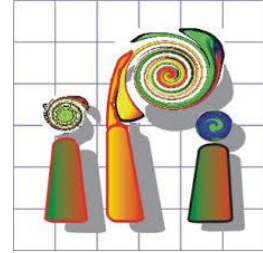


Leibniz  
Universität  
Hannover



**Leibniz University Hanover**

**Institute of Photogrammetry and Geoinformation**

**Helmholtz Centre Potsdam, German Centre for Geoscience**

**Master Thesis**

# **Mitigation of Ionospheric Errors in L-band InSAR Observations**

Zhiyuan Wang

Matri.-Nr.:10006721

Supervisor: Prof. Dr. Mahdi Motagh

Co-supervisor: Dr.-Ing. Sanaz Vajedian

Potsdam, April 2019

# Declaration of Authorship

I, Zhiyuan Wang, declare that this master thesis and works presented herein have been composed by myself. All the consulted published or unpublished works have been cited clearly. No sources or works other than those listed in the bibliography have been used. All works here have not been submitted to other institution to obtain a degree.

Signed:

---

Date:

---

# Acknowledgement

I wouldn't finish this thesis without supports from my family, friends and colleagues from both German Centre for Geosciences (GFZ) and Leibniz University Hanover. By writing it, I learned a lot about how to implement scientific research, how to face challenges and how to solve problems individually or by group working. I hereby want to thank people who helped during the thesis.

First I would like to thank Mahdi Motagh from GFZ, my supervisor, who gave me such an interesting topic for the thesis. During this study he gave me a lot of helps and brilliant ideas to lead me to achieve my goal. His advice has always been patient and helpful. I am really grateful for having such a responsible supervisor.

Then I would like to thank my co-supervisor Sanaz Vajedian from Leibniz University Hanover. I thank her for giving me many useful advice and ideas of improving my methods and results. These ideas really helped me to polish my results that are presented in this thesis.

I am also grateful to Lucas Schreiter and Chao Xiong, from GFZ, section 2.3. Lacking of knowledge from ionosphere and global space weather, I was facing a huge challenge. They taught me useful knowledge about ionosphere and offered me help when I was implementing CODE based method. I am really grateful for their help.

Many thanks to Wei Tang from China University of Mining & technology (Beijing) and Mahmud Haghshenas Haghighi from GFZ, section 1.4, who provided me a lot of helps on implementing my methods, polishing results and especially on dealing with troposphere error in InSAR observations.

My special thanks to Sylvia Magnussen from GFZ who helped me on installing and maintaining software and system so that I could focus on my thesis without worrying about them.

Last but not least, I want to thank my parents and my girlfriend for supporting me

spiritually to finish this thesis and my master degree. It was their love that encourages me to go further of my study.

# 1 Abstract

Space-borne Synthetic Aperture Radar (SAR) is one of the most often used technology to measure surface displacement of large areas. With development of satellite and sensor technology, more SAR data are available. According to the wavelength of the signal, SAR data can be categorized into different bands, each of them has its own advantages and can be used for different applications. Of all the bands, L-band SAR data (~24cm wavelength) has an outstanding ability of penetrating vegetation due to its long wavelength. However, this attribute also becomes a reason that it is sensitive to Ionosphere when the signal is transferred between satellites and target.

The sensitivity of L-band SAR data to Ionosphere leads to a phase shift in the generated SAR Interferometry (InSAR) and becomes a major error in L-band InSAR observations. In the recent years, several methods have been developed in order to mitigate this error. In this master thesis, 4 different methods have been applied to try to mitigate ionospheric phase from InSAR observations. Large scaled Ionospheric effect can create a slope along the direction of the ionosphere fluctuation. This results in residual phase in InSAR observations. To remove this effect, a residual phase removal based on a polynomial fit of a lower degree can be applied. Ionosphere product from Center for Orbit Determination in Europe (CODE) was also used for ionospheric phase correction. This product provides global covered total electron content (TEC) map based on global positioning system (GPS)'s observations. For smaller scaled ionospheric phase correction, two methods were applied based on a linear relationship between the azimuth shift from InSAR observations. They are:(1) Multiple Aperture Interferometry (MAI) based method and (2) Amplitude Tracking (AT) based method.

To test and evaluate these methods, L-band SAR data from Advanced Land Observing Satellites (ALOS)-1 Phased Array type L-band Synthetic Aperture Radar (PALSAR) data and ALOS-2 ScanSAR data were used. These two satellites were launched by Japan Aerospace Exploration Agency (JAXA). ALOS-1 data set belongs to

Alaska in arctic, where the ionosphere is affected by the sun activities and creates aurora that can have a strong effect on signal transportation. ALOS-2 data set belongs to Ecuador, where the ionospheric activities are strong because its location in equatorial regions. In 2016, a  $M_w$  7.8 earthquake happened in this area, this event also helped us to estimate whether our methods are suitable for different geological hazard applications.

Results of experiments demonstrated that residual phase removal can remove large scale ionospheric phase effectively, but depends on specific parameter setting on different regions. This method is suitable for regions where there is strong surface displacement e.g. earthquake. Method based on CODE model is proved to be not sufficient for correcting all ionospheric error. Both MAI based method and AT method had good performance on ALOS-1 PALSAR data. These two methods are suitable if there is no appreciable surface displacement in the study region.

# Content

|   |   |    |
|---|---|----|
| 1 | Abstract.....   | I  |
| 2 | Introduction.....   | 1  |
|   | 2.1 Motivation.....                                       | 1  |
|   | 2.2 Task Description.....                                 | 4  |
| 3 | Related Works.....  | 6  |
|   | 3.1 Ionospheric Errors.....                               | 6  |
|   | 3.1 GPS Based Methods.....                                | 6  |
|   | 3.2 Azimuth Shift Based Methods.....                      | 7  |
|   | 3.4 Related Work Discussion.....                          | 9  |
| 4 | Theoretical Background.....                               | 10 |
|   | 4.1 SAR Interferometry.....                               | 10 |
|   | 4.1.1 Concept of SAR.....                                 | 10 |
|   | 4.1.2 SAR Data.....                                       | 11 |
|   | 4.1.3 Interferogram Generation.....                       | 13 |
|   | 4.2 Ionospheric Error in InSAR.....                       | 14 |
|   | 4.2.1 Ionospheric Phase Delay.....                        | 14 |
|   | 4.2.2 Faraday Rotation Effect.....                        | 15 |
|   | 4.2.3 Ionospheric Phase Shift in InSAR.....               | 16 |
|   | 4.3 Residual Phase Removal.....                           | 19 |
|   | 4.4 GPS based Ionospheric Phase Estimation.....           | 20 |
|   | 4.4.1 GPS Signal.....                                     | 20 |
|   | 4.4.2 GPS based TEC Measurement.....                      | 21 |
|   | 4.3.1 CODE Product.....                                   | 22 |
|   | 4.5 Azimuth Shift Based Ionospheric Phase Estimation..... | 24 |
|   | 4.5.1 Amplitude Tracking based Method.....                | 26 |
|   | 4.5.1.1 Cross-correlation and Coherence.....              | 26 |
|   | 4.5.1.2 Ionospheric Phase Estimation based on AT.....     | 27 |
|   | 4.5.2 Multiple Aperture Interferogram based Method.....   | 28 |
|   | 4.5.2.1 Multiple Aperture Interferogram.....              | 28 |
|   | 4.5.2.2 Ionospheric Phase Estimation based on MAI.....    | 30 |
| 5 | Methodologies.....  | 32 |
|   | 5.1 Residual Phase Removal.....                           | 32 |
|   | 5.2 CODE based Ionospheric Phase Correction.....          | 33 |
|   | 5.3 Azimuth Shift based Ionospheric Phase Correction..... | 34 |
| 6 | Data Overview.....  | 36 |
|   | 6.1 Satellite Data Introduction.....                      | 36 |
|   | 6.1.1 ALOS-1 PALSAR Data.....                             | 36 |
|   | 6.1.2 ALOS-2 ScanSAR data.....                            | 37 |
|   | 6.2 Study Area.....                                       | 39 |
|   | 6.2.1 ALOS-1 Data.....                                    | 39 |

|       |   |    |
|-------|---|----|
| 6.2.2 | ALOS-2 Data.....                                      | 40 |
| 7     | Experiments and Results.....                          | 42 |
| 7.1   | Interferogram Generation.....                         | 42 |
| 7.2   | Residual Phase Removal Correction.....                | 44 |
| 7.2.1 | Pre-seismic Interferogram.....                        | 45 |
| 7.2.2 | Co-seismic Interferogram.....                         | 51 |
| 7.3   | CODE based Ionospheric Phase Correction.....          | 55 |
| 7.4   | Azimuth based Ionospheric Phase Removal.....          | 60 |
| 7.4.1 | MAI based Method.....                                 | 60 |
| 7.4.2 | AT based Method.....                                  | 68 |
| 7.5   | Discussion.....                                       | 76 |
| 7.5.1 | Residual Phase Removal Correction.....                | 76 |
| 7.5.2 | CODE based Ionospheric Phase Correction.....          | 77 |
| 7.5.3 | Azimuth shift based Ionospheric Phase Correction..... | 77 |
| 8     | Conclusion and Outlook.....                           | 79 |
| 8.1   | Conclusion.....                                       | 79 |
| 8.2   | Outlook.....  | 80 |
|       | Bibliography.....                                     | 81 |



# List of Figures

|   |   |    |
|---|---|----|
| 1 | Abstract.....   | I  |
| 2 | Introduction.....   | 1  |
|   | Figure 2.1: Ionospheric phase deformation with respect to TEC variance.....   | 2  |
|   | Figure 2.2: Deformation caused by ionospheric phase in ALOS-2 data.....   | 3  |
|   | Figure 2.3: Deformation caused by ionospheric phase in ALOS PALSAR data.....  | 4  |
| 3 | Related Works.....  | 6  |
| 4 | Theoretical Background.....   | 10 |
|   | Figure 4.1: Imaging geometry of radar system.....   | 11 |
|   | Figure 4.2: SAR observations from ALOS-2 data, Ecuador.....   | 12 |
|   | Figure 4.3: Example of azimuth streaks caused by ionospheric error on ALOS PALSAR data.....   | 17 |
|   | Figure 4.4: Example of azimuth streaks caused by ionospheric phase shift on ALOS-2 data .....                                       | 18 |
|   | Figure 4.5: Quadratic ionospheric error.....  | 19 |
|   | Figure 4.6: Structure of GPS signal.....  | 20 |
|   | Figure 4.7: Global covered TEC map , daily based product.....   | 23 |
|   | Figure 4.9: Global covered TEC map, hourly based product.....   | 24 |
|   | Figure 4.10: MAI geometry of forward- and backward-looking interferograms.....  | 28 |
|   | Figure 4.11: Working flow of generating MAI interferogram.....  | 30 |
| 5 | Methodologies.....  | 32 |
|   | Figure 5.1: Working flow of residual phase removal strategy.....  | 33 |
|   | Figure 5.2: Working flow of CODE based ionospheric phase correction.....  | 34 |
|   | Figure 5.3: Working flow of azimuth shift based ionospheric phase correction.....   | 35 |
| 6 | Data Overview.....  | 36 |
|   | Figure 6.1: Imaging geometry of ALOS-1 PALSAR data acquisition.....   | 37 |
|   | Figure 6.2: ALOS-2 Observation Mode.....  | 39 |
|   | Figure 6.3: Study area in Alaska.....   | 40 |
|   | Figure 6.4: Study area in Ecuador.....  | 41 |
| 7 | Experiments and Results.....  | 42 |
|   | Figure 7.1: Interferogram from ALOS-1 data pair in Alaska.....  | 43 |
|   | Figure 7.2: Interferogram from ALOS-2 data pair in Ecuador.....   | 43 |
|   | Figure 7.3: Interferogram from ALOS-2 data pair in Ecuador.....   | 44 |
|   | Figure 7.4: Ground Control Points distribution.....   | 45 |
|   | Figure 7.5: Wrapped interferogram of pre-seismic pair corrected by removing residual phase with different polynomial degrees.....   | 46 |
|   | Figure 7.6: Unwrapped interferogram of pre-seismic pair corrected by removing residual phase with different polynomial degrees..... | 47 |
|   | Figure 7.7: Mean value of unwrapped phase of corrected interferograms.....  | 48 |
|   | Figure 7.8: STD of unwrapped phase of corrected interferograms.....   | 48 |
|   | Figure 7.9: Residual phase removal results from testing pair. (a): Master: .....  | 49 |
|   | Figure 7.10: DEM of study area.....   | 50 |

|  |    |
|--|----|
| Figure 7.11: Phase with respect to elevation.....  | 50 |
| Figure 7.12: GCPs distribution, points were selected all over the area.....  | 51 |
| Figure 7.13: Wrapped interferogram of co-seismic pair corrected by removing residual phase.....                              | 52 |
| Figure 7.14: Unwrapped interferogram of co-seismic pair corrected by removing residual phase.....                            | 53 |
| Figure 7.15: Area selected for statistical analysis.....   | 54 |
| Figure 7.16: Mean value of unwrapped phase of selected area from corrected interferograms.....                               | 54 |
| Figure 7.17: STD of unwrapped phase of corrected interferograms.....   | 55 |
| Figure 7.18: Global covered VTEC map (in TECU) generated by SH expansion.....  | 56 |
| Figure 7.19: Global covered VTEC variance map of pre-seismic pair.....   | 57 |
| Figure 7.20: Wrapped generated ionospheric phase on different epochs.....  | 58 |
| Figure 7.21: Ionospheric phase generated from CODE hourly product at 17:00.....  | 58 |
| Figure 7.22: Unwrapped ionospheric phase .....   | 59 |
| Figure 7.23: Corrected interferogram .....   | 59 |
| Figure 7.24: Intermediate results of MAI based method on ALOS-1 PALSAR data....  | 61 |
| Figure 7.25: The first derivative of InSAR phase with respect to azimuth direction....                                       | 61 |
| Figure 7.26: Linear relationship of scaled MAI phase with respect to the derivative of InSAR phase in azimuth direction..... | 62 |
| Figure 7.27: Calculated Ionospheric phase in radiant.....  | 63 |
| Figure 7.28: Unwrapped ionospheric phase by MAI method.....  | 63 |
| Figure 7.29: Wrapped ionospheric phase by MAI method.....  | 63 |
| Figure 7.30: Unwrapped corrected interferogram .....   | 64 |
| Figure 7.31: DEM and selected area for troposphere estimation.....   | 65 |
| Figure 7.32: Results of linear regression.....   | 66 |
| Figure 7.33: MAI results from ALOS-2 ScanSAR data from pre-seismic pair.....   | 67 |
| Figure 7.34: Intermediate results of AT based method on ALOS-1 PALSAR data .....   | 69 |
| Figure 7.35: Linear relationship between scaled AT azimuth phase and the derivative of InSAR phase in azimuth direction..... | 69 |
| Figure 7.36: Calculated unwrapped ionospheric phase based on AT based method..   | 70 |
| Figure 7.37: Calculated ionospheric phase using AT based method ALOS-1 data.....   | 70 |
| Figure 7.38: Ionospheric phase correction results based on AT based method.....  | 71 |
| Figure 7.39: Results of linear regression.....   | 72 |
| Figure 7.40: Selected area for AT based Ionospheric phase correction from ALOS-2 ScanSAR pre-seismic pair.....               | 73 |
| Figure 7.41: Intermediate results of AT based method on ALOS-2 data.....   | 74 |
| Figure 7.42: Comparison of calculated ionospheric phase and original InSAR phase   | 75 |
| Figure 7.43: Corrected InSAR phase of ALOS-2 data.....   | 75 |
| 8 Conclusion and Outlook.....  | 79 |
| Bibliography.....  | 81 |

# List of Tables

|   |   |    |
|---|---|----|
| 1 | Abstract.....   | I  |
| 2 | Introduction.....   | 1  |
| 3 | Related Works.....  | 6  |
| 4 | Theoretical Background.....   | 10 |
|   | Table 4.1 Wavelength and frequency of SAR data.....   | 11 |
| 5 | Methodologies.....  | 32 |
| 6 | Data Overview.....  | 36 |
|   | Table 6.1 PALSAR characteristic.....  | 36 |
|   | Table 6.2 ALOS-2/PALSAR-2 characteristic.....   | 38 |
|   | Table 6.3 ALOS PALSAR data information.....   | 40 |
|   | Table 6.4 ALOS-2/PALSAR -2 data information.....  | 41 |
| 7 | Experiments and Results.....  | 42 |
|   | Table 7.1: Multi-look parameters for ALOS-1 PALSAR data.....  | 42 |
|   | Table 7.2: Multi-look parameters for ALOS-2 ScanSAR data.....   | 42 |
|   | Table 7.3: Principle parameters setting for residual phase removal.....   | 44 |
|   | Table 7.4: Mean values and STD values of original InSAR result and corrected InSAR results of pre-seismic image pair..... | 47 |
|   | Table 7.5: Mean values and STD values of original InSAR result and corrected InSAR results of co-seismic image pair.....  | 54 |
|   | Table 7.6: Estimated linear parameters (MAI based method).....  | 62 |
|   | Table 7.7:STD and mean value before and after ionospheric correction (MAI based method).....                              | 65 |
|   | Table 7.8:STD and mean value before and after subtracting tropospheric trend (MAI based method).....                      | 67 |
|   | Table 7.9: Estimated linear parameters (AT based method).....   | 69 |
|   | Table 7.10:STD and mean value before and after ionospheric correction (AT based method).....                              | 71 |
|   | Table 7.11:STD and mean value before and after subtracting tropospheric trend (AT based method).....                      | 73 |
|   | Table 7.12: Statistical result of two methods of azimuth based ionospheric phase correction.....                          | 77 |
| 8 | Conclusion and Outlook.....   | 79 |
|   | Bibliography.....   | 81 |

## 2 Introduction

### 2.1 Motivation

Synthetic Aperture Radar Interferometry (InSAR) technology is a powerful tool for earth surface deformation analysis. Compared to Global Positioning System (GPS) technology, it has a continuous observation of the whole study area without setting any receivers. This technology is especially suitable to analyse deformation with seismic deformation e.g. deformation of earthquake event. In the past, both co-seismic deformation (Simons, Fialko, & Rivera, 2002) and post-seismic motion (Ryder, Parsons, Wright, & Funning, 2007) have been analyzed by using InSAR observations.

With a high revisit time period e.g. Sentinel-1 TOPS for 12 days for Advanced and Land Observing Satellites (ALOS)-2 ScanSAR for 14 days, strategies like Persistent Scatter Interferometry (PSI) approach (Ferretti, Prati, & Rocca, 2001) and Small Baseline Subset (SBAS) approach (Lanari, Mora, Manunta, Berardino, & Sansosti, 2004) can be applied to support a time series analysis for estimating slow surface movements like land slide (Haghshenas Haghighi & Motagh, 2016) and land subsidence (Motagh et al., 2017).

For all applications mentioned above, generating an interferogram is the most important process. In order to get better quality of Interferogram, it is important to get rid of ionospheric errors in it.

Ionosphere exists from about 60 km until more than 2,000 km. When the radiation from the sun reaches the ionosphere, it creates more free electrons by a process of ionization. This increases the electron density of atmosphere. Electron density can be described using the concept of total electron content (TEC), which is considered to be the total number of electrons between satellites and target along a tube of 1 m<sup>2</sup>. The variance of TEC from different epochs of the same area causes ionospheric fringes in interferograms. One fringe in the interferogram represents the deformation corresponding to half of the wavelength, this error can lead to a large bias in our estimated deformation.

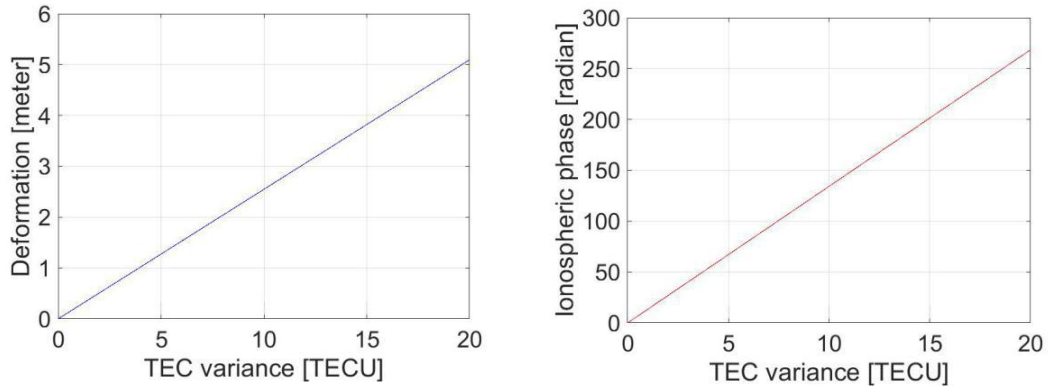


Figure 2.1: Ionospheric phase deformation with respect to TEC variance.

Fig. 2.1 demonstrates the relationship between Ionospheric phase, deformation and corresponding TEC variance. The resulted error increases with the TEC variance between the master and slave images. If we have a TEC variance of 20 TECU, we would obtain 6 meter of deformation in our final result. This can be a large error of the further deformation analysis.

We always have a higher electron concentration at the local time of around 12:00 and less at night because of the exposure from the sun. SAR satellites that offers L-band data like ALOS-2, for descending data, always captures data at local time around 12:00 and if the sun activities from one acquisition day were intense, it could lead to a relative big TEC variance between two acquisitions. The ionospheric error is especially obvious in equatorial regions due to the big incident angle of the sun radiation. Fig. 2.2 shows the interferograms generated in the study area that locates in Ecuador, in the equatorial regions. This example shows the earthquake deformation. We can see that except from the earthquake deformation, there are residual fringes caused by ionosphere. The deformation error in this example reaches 1 meter.

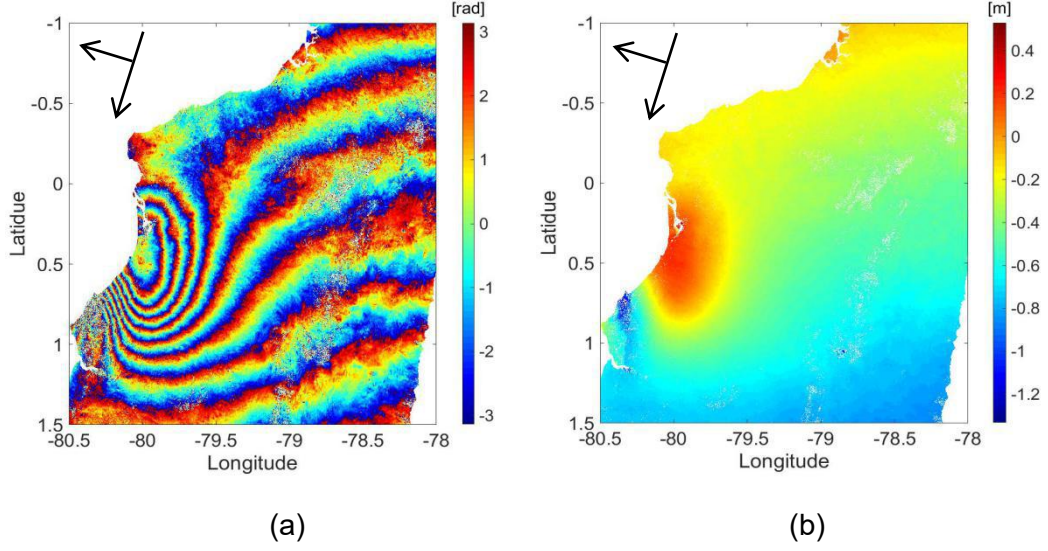
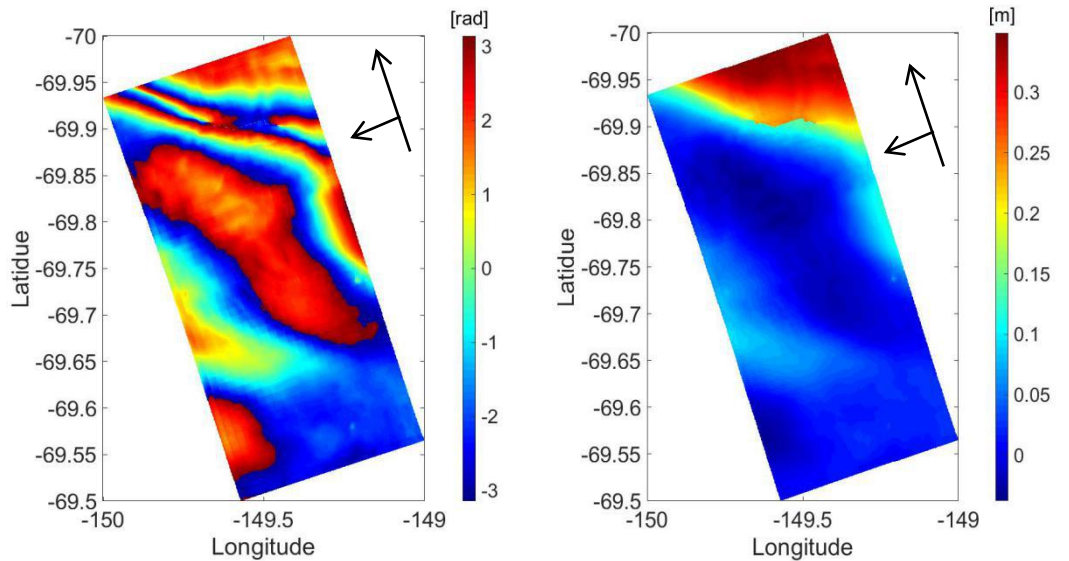


Figure 2.2: Deformation caused by ionospheric phase in ALOS-2 data (a) Wrapped interferogram and (b) relative deformation along line of sight (LOS) of test site in Ecuador, where there was a Mw 7.8 earthquake happened on 16,04,2016. The master data was acquired on 01,04,2016 and the slave data was acquired on 29,04,2016.

Another important application of SAR is to study polar region. In this kind of application, ionospheric phase becomes again a big challenge. Due to the magnetic field from the earth, polar region will suffer more from the sun activities than other regions and can have so called “Aurora” when there is solar wind. This phenomenon is caused by strong ionization of ionosphere. Thus, the corresponding variation of TEC can also lead to large ionospheric error in the interferograms that generated from this regions.



(a)

(b)

Figure 2.3: Deformation caused by ionospheric phase in ALOS PALSAR data (a) Wrapped interferogram and (b) relative deformation along line of sight (LOS) of test site in northern Alaska, this region locates in polar area and can be easily affected by solar activities. The master data was acquired on 01,04,2007 and the slave data was acquired on 17,05,2007.

Fig. 2.3 demonstrates interferograms generated in northern Alaska of USA, where the aurora activities occurred frequently. In this example we can see fringes caused in a smaller scale, comparing to the large scaled ionospheric phase that created a slop in the image, this kind of error is more irregular.

From examples shown above, we can see the affect brought by ionospheric error are strong, especially when we have study area that locate in equatorial region and polar region. It is therefore really necessary to eliminate ionospheric errors in InSAR observations. Fig. 2.2 and Fig. 2.3 are our study cases in this thesis, the detailed data description the corresponding corrections, results and discussions will be present in following chapter.

## 2.2 Task Description

Ionospheric effects in InSAR observation is a complicated topic, because without any sensor to give direct observations from it as a benchmark, it is hard to get rid of it totally. This master thesis focuses on the goal of evaluating different methods for mitigating ionospheric errors. In this thesis 4 different methods were implemented to try to mitigate ionospheric errors from both ALOS-1 (Phased Array type L-band Synthetic Aperture Radar) PALSAR data and ALOS-2 ScanSAR data (~L-band) according to different types of effect that can be brought by ionosphere. These 4 methods are: (1) residual phase removal based method, (2) Center for Orbit Determination in Europe (CODE) ([http://www.aiub.unibe.ch/research/code\\_\\_\\_analysis\\_center/index\\_eng.html](http://www.aiub.unibe.ch/research/code___analysis_center/index_eng.html)) model based method, (3) Multiple-Aperture Interferometry (MAI) based method and (4) Amplitude tracking (AT) based method.

Residual phase removal based method and CODE model based method were applied and test on the data for Ecuador due to its large coverage of the area that lead to a large scale ionospheric error in generated interferogram. In this study, in order to get a better result from TEC map that fit the acquisition time, we used CODE hourly based products. In order to boost the resolution of it, a spherical harmonics expansion was applied and the hourly global covered ionospheric map was generated. TEC variance value were then calculated and corresponding ionospheric phase maps were generated and removed from original interferogram.

Both MAI based method and AT based methods have been implemented and tested on ALOS PALSAR data that locates in Alaska for testing and removing small scaled ionospheric errors. An evaluation of the results has been done by estimating the tropospheric effect using a linear regression. After evaluation and comparison, we additionally applied Amplitude based methods on ALOS-2 data from Ecuador to test its ability.

Comparison of different methods and discussion of the advantages and disadvantages has been done in the end of our experiments and corresponding detailed implementation and results will be present in following chapters.



## **3 Related Works**

### **3.1 Ionospheric Errors**

Ionospheric effect on microwave signal has first been discussed in GPS technology (Wilson, Mannucci, & Edwards, 1995), and was discussed in SAR community later. At first, people discovered some kind of shift along azimuth direction which appears like a doppler effect. This kind of shift were regarded as “Azimuth Streak” and was first discussed as an effect caused by ionospheric electron density fluctuations by Gray, Mattar and Sofko (2000). Azimuth streak can be described in two forms, they are (1) linear streak and (2) curved streak in range. It was first addressed from their study that ionospheric effect can be easily observed in arctic and antarctic area due to the ionozation of atmosphere. Matter and Gray (2002) discussed ionospheric error on SAR data as the first order error of ionosphere and can be corrected if we can assume the linear relationship between doppler frequency and azimuth shift. Later ionospheric effects on SAR interferogam has been studied in detailed and described as 3 types according to (Meyer, Bamler, & Jakowski, 2006). According to their paper, two major errors can be caused by ionosphere in SAR system, they are: (1) Faraday Rotation in Polarimetric SAR (Pol-SAR) applications and (2) Phase shift caused by azimuth streak in InSAR applications. The detection and correction of faraday rotation was developed for Pol-SAR L-band data (Meyer, & Nicoll, 2008), and for InSAR application, a correction working frame work was set up later in 2011 for the first time (Meyer, 2011). In their paper, the author specified ionospheric error in different scale level and set a mathematical framework for correcting ionospheric error, which is the main framework of all azimuth shift based methods.

### **3.1 GPS Based Methods**

For GPS technology, ionospheric effect is always an issue because it also has L-band signal as carrier frequencies. Thanks to its two carrier frequencies, GPS has also the ability to extract TEC from the satellites and targets by combining GPS pseudo range and phase

measurements (Lanyi & Roth, 1988). This approach laid the foundation of implementing a global TEC measurement. Based on this approach, a global mapping technique for GPS-derived TEC was developed by Mannucci, Wilson, Yuan, Ho, and Lindqwister (1998). In this study, global covered TEC measurement was established based on the global GPS network (GGN). The author also introduced a Kalman filter to smooth the map in time. For a better global modeling, surface harmonic fitting technique has also been introduced in generating global TEC product (Wilson, Mannucci, & Edwards, 1995). Further, Dyrud, Jovancevic, Brown, Wilson and Ganguly (2008) improved the TEC measurement with GPS by eliminate 3 biases while combining phase measurement and code measurement.

Global covered TEC product from CODE provides a high quality TEC product, and this product has been used to establish global TEC model for further use (Jakowski, Hoque, & Mayer, 2011).

Studies for mitigating ionospheric phase by using CODE product are really rare. Mateus, Catalão, and Nico (2017) used CODE daily based product to generate ionospheric phase and remove it from Sentinel-1 data, but our study showed that a daily based product is not sufficient for ionospheric error correction.

## **3.2 Azimuth Shift Based Methods**

Methods for ionospheric correction can be grouped into two types according to (Meyer, 2010): (1) range spectrum based method and (2) azimuth spectrum based method. The second type has been investigated a lot in recent years and is also the major method that we implemented in this thesis.

According to (Matter & Gray, 2002), there is a linear relationship between azimuth streak and doppler frequency. The main idea of azimuth shift based method is to generate the azimuth shift, and parameters of the linear relationship so that we can estimate the corresponding ionospheric phase streak (IPS) from them.

To generate azimuth shift, AT-based method and MAI-based method were implemented in this thesis. Chen and Zebker (2006) implemented azimuth shift estimation

based on AT and combined it with GPS observations to confirm that the azimuth shift is caused by kilometer-scaled spatial variation of ionosphere (large scale effect). Wegmüller, Werner, Strozzi and Wiesmann (2006) generated ionospheric phase delay by using cross-correlation and then manually set a filter to remove non-dispersive phase. Both studies were worked on L-band ALOS PALSAR data. For AT based method, coregistration is important. Therefore Chen and Zebker (2014) improved coregistration strategy by combining complex and amplitude cross-correlation on ALOS PALSAR observation in Greenland. As an improvement, Gomba, Gonzalez and Zan (2017) shows the potential of combining AT based method and enhanced spectral diversity (ESD) to process Sentinel-1 TOP data and ALOS-2 ScanSAR data.

MAI were first designed to measure and extract azimuth displacement from InSAR data (Bechor, & Zebker, 2006). It generates deformation from azimuth and range direction by separating full aperture into forward and backward apertures. An improvement of this method by removing flat-earth and topographic phase from MAI has been applied in (Jung, Won, & Kim, 2009). Hu et al. (2012) generated 2D displacement of 2012 Yushu earthquake and then they generated 3D coseismic displacement of 2010 New Zealand earthquake used MAI method (Hu et al. 2012). In both studies, they applied a ionospheric correction on ALOS PALSAR data based on MAI result, which demonstrate the potential of using MAI to mitigate ionospheric error in SAR data. A standard working flow of using MAI to do ionospheric correction were discussed then by Jung, Lee, Lu, and Won (2013). In their study, linear relationship between MAI phase and azimuth derivative were discussed deeply and an ionospheric correction on ALOS-PALSAR data was applied. After that, Liu, Jung, and Lu (2014) further improved the MAI based method combining orbit error removal with considering earth flat residual phase. This working flow were then applied in measuring glacier velocity variations (Chae, Lee, Jung, & Zhang, 2017). Results from their paper proved that this method has a good performance on ALOS PALSAR data. MAI based method were then applied on ALOS-2 ScanSAR data to analyse water level change, this approach estimated the ionospheric effect in large scale by processing sub-swaths of data separately (Cao, Lee, Jung, & Yu, 2017). In their paper, authors first applied a low

degree of polynomial fit on the data to get rid of orbit error, the MAI based method were applied just for small scale ionospheric error.

### **3.4 Related Work Discussion**

In this thesis we first implemented residual phase removal method on ALOS-2 ScanSAR data. This strategy is based on the assumption that the ionospheric phases are forming a slop along one direction and causing a ramp in our InSAR observation. The underlying theory is the same as removing orbit and flat earth phase from InSAR observation (Liu et al., 2014).

The second method we implemented in this thesis is CODE model based method. We utilized hourly based CODE product and generated vertical TEC (VTEC), slant TEC (STEC) hourly from 00:00 to 13:00 (UTC) and try to generate ionospheric map for ALOS-2 ScanSAR data, and remove it from the InSAR observation. Before there was only studies that used daily based product (Mateus et al., 2017). Therefore this is the first time to test and apply such a approach in this field.

For azimuth based method, we implemented AT based and MAI based method separately. AT based method were based on a cross-correlation strategy for co-registration. For the test on ALOS-2 ScanSAR data, we used only amplitude co-registration (Chen & Zebker, 2014). MAI method were implemented according to the frame work generated by Jung et al. (2013).

## 4 Theoretical Background

### 4.1 SAR Interferometry

#### 4.1.1 Concept of SAR

Synthetic Aperture Radar (SAR) is an image system using microwave signal. It provides the reflection information of the signal from target objects and measure the length of travel path between the satellite and objects. Thanks to microwave signal, SAR can penetrate cloud easily and works both in day- and night time. This attribute brings a big advantage comparing to optical remote sensing image system.

A SAR image system usually carries a radar sensor that points to the surface of the earth and is perpendicular to the orbit of the platforms (e.g. satellites and aircraft). The flight direction of the platform is called azimuth direction and the direction along the look angle is called range direction. As shown in the following sketch, arrow “E” corresponds to azimuth direction, and arrow “D” corresponds to range direction.

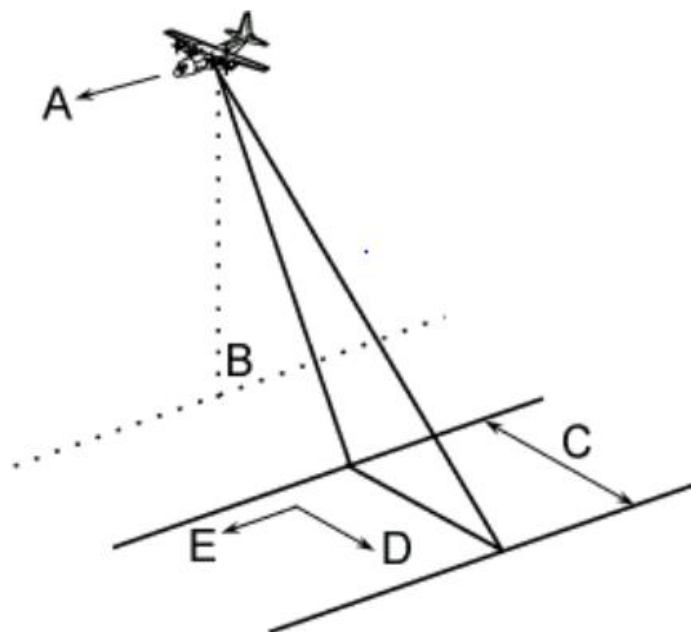


Figure 4.1: Imaging geometry of radar system. Reprinted from 'Geometry Glossary', by European Space Agency (ESA), 2014, Retrieved from <https://earth.esa.int/handbooks/asar/CNTR5-5.html#eph.asar.gloss.geo:GEOMETRY>.

For a radar remote sensing system, the resolution of an image is defined in two directions: (1) Range resolution and (2) Azimuth resolution. Range resolution is also called cross-track resolution. It represents the minimum distance along range direction that two objects can be separated. Azimuth resolution is also called along-track resolution. It represents also the ability of distinguishing two objects along azimuth direction. In a radar system, azimuth resolution is decided by antenna length and distance from sensor to the ground:

$$R_a = \frac{R\lambda}{l} \quad (4.1)$$

where  $R$  represents ground to sensor distance.  $\lambda$  represents the wavelength and  $l$  represents the effective antenna length. When the signal's wavelength is fixed and the platform is on the right position of the orbit (distance from ground to sensor is also fixed), the only parameter that can be modified is the antenna length, and if an antenna length is fixed by the design of the satellite and limited from the the sensor, the azimuth resolution shall be low. SAR technology solves this problem by receiving back scattered echos of signal from the same object along flying. This strategy simulates a larger antenna and thus increases the azimuth resolution. The simulated large antenna is so-called synthetic aperture. The length of aperture is the key element to the resolution.

### 4.1.2 SAR Data

Common operational space-borne SAR system works in the following bands:

Table 4.1 Wavelength and frequency of SAR data

| Frequency Band | Frequency (GHz) | Wavelength (cm) |
|----------------|-----------------|-----------------|
| X band         | 12.5-8          | 2.4-3.8         |
| C band         | 8-4             | 3.8-7.5         |
| L band         | 2-1             | 15-30           |

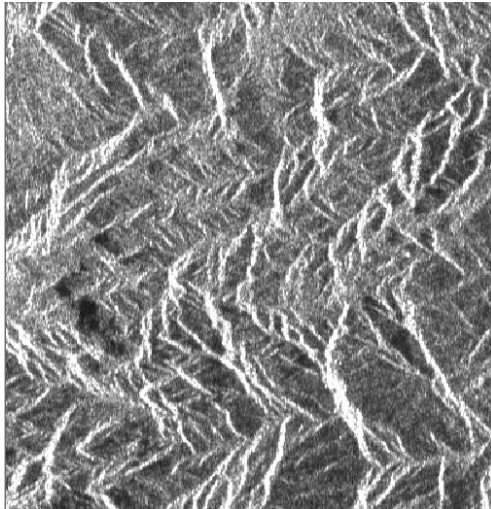
Different band has different ability of penetrating object e.g. cloud, vegetation, snow and soil, and can be used for different applications accordingly. The longer the wavelength is, the better penetrating ability it has. However, when the wavelength is increasing, the sensitivity of the signal to the ionosphere is also increasing.

SAR systems provide two observations, they are: (1) Amplitude observation and (2) phase observation. Amplitude observation is a measurement of amplitude of radiation back scatter attributes of the target object. This observation contains information of the materials, chemical component, or surface structure of the target object. The observation itself is always shown in brightness in a gray-scaled image, and similar to optical data, this data illustrates the real sight of the target area and can be used as an input of optical remote sensing analysis.

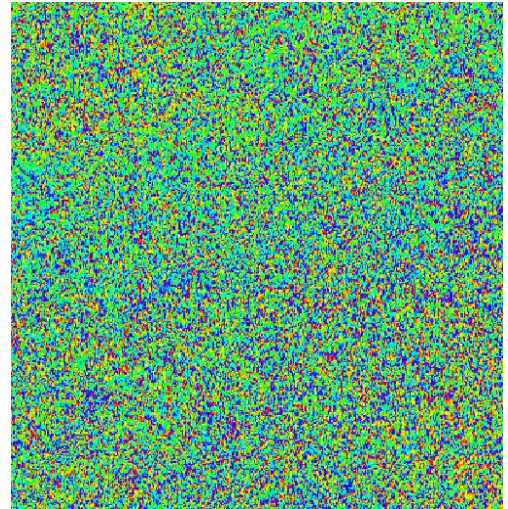
Phase observation is a function of the distance from the satellite to the target object:

$$\phi = \frac{4\pi}{\lambda} R \quad (4.2)$$

Phase observation is usually used to calculate the differential phase, and based on this, the relative deformation of the ground surface can be calculated. This theory of this will be discussed in the next session.



(a)



(b)

Figure 4.2: SAR observations from ALOS-2 data, Ecuador, acquired on 08, 01, 2016. (a)

Amplitude observation and (b) Phase observation.

### 4.1.3 Interferogram Generation

To measure the deformation or surface movement of target area, the differential phase observations from two images can be calculated. These two images are called “Master” image and “Slave” image (usually the image that taken earlier is regarded as “Master”). An interferogram is to generated in order to measure the relative change of the distance from the satellite position to the target sites. For a SAR data, the amplitude part and the phase part are stored in the form of complex number. Generating interferogram is a process of complex conjugate multiplication of the signal from two images, where we multiple the amplitude observation from one image with the other and the result of the phase is a phase difference between two images.

$$\Delta\phi = \phi_{slave} - \phi_{master} \quad (4.3)$$

When considering the phase for one single pixel, assuming there is no disturbances, according to the eq. (4.2), the differential phase between two epochs will be:

$$\Delta\phi = \frac{4\pi}{\lambda} \Delta R_{def} \quad (4.4)$$

where  $\Delta R_{def}$  is the relative deformation we want to measure. But in reality, there are several error sources that can affect our final result, in that case, the modification of the phase will be:

$$\Delta\phi = \frac{4\pi}{\lambda} (\Delta r_{topo} + \Delta r_{tropo} + \Delta r_{iono} + \Delta r_{def}) \quad (4.5)$$

In eq.(4.5),  $\Delta r_{topo}$  is the topographic path delay that brought by the change of the topography. This part contains flat-earth delay and topography-related phase.  $\Delta r_{tropo}$  is the differential tropospheric path delay and  $\Delta r_{iono}$  is the differential ionospheric delay. When processing the signal, we should also pay attention to the doppler phase that caused by doppler effect along the orbit, which is called orbit error.

In order to generate the right phase related to deformation, we need to correct all the



errors mentioned above. Different methods and models were developed to mitigate these errors and in this thesis, we focus on how to mitigate ionospheric error.

## 4.2 Ionospheric Error in InSAR

### 4.2.1 Ionospheric Phase Delay

Microwave signal travels in speed of light in vacuum which is approximately  $3 \times 10^8$  m/s. This speed changes, when the electron density of the medium varies. While the ionosphere is exposed by the sun, it is ionized by solar radiation. This leads to a variance of electron density. The electron density can be expressed using  $N_e$  in  $e^-/m^3$ . The magnitude of electron density variance can be of  $N_e$  from  $10^{11}$  to  $10^{12}$   $e^-/m^3$  at altitude of 300 to 500 km (Sanz , Juan Zornoza & Hernández-Pajares, 2011).

The refraction of the signal caused by ionosphere can be described in GPS signal (L-band) where it has both phase and pseudo range measurement (Sanz et al., 2011):

$$\Delta_{ph,f}^{iono} = -\frac{K}{f^2} \int N_e dl \quad \Delta_{gr,f}^{iono} = +\frac{K}{f^2} \int N_e dl \quad (4.6)$$

In eq.(4.6),  $\Delta_{ph,f}^{iono}$  is the phase refraction, where the minus sign shows the phase advance i.e. negative delay brought by ionosphere.  $\Delta_{gr,f}^{iono}$  on the contrast shows the positive delay from code measurement (also regarded as “Group delay”).  $K$  is a constant with  $K = 40.28$   $m^3/s^2$ . In this equation, the integral part is defined as a total electron content along the slant direction (STEC):

$$STEC = \int N_e dl \quad (4.7)$$

The concept of total electron content (TEC) is used to describe the electron density along the propagation from the satellite to the ground by imaging a tube with  $1$   $m^2$  cross section along the path, and the total number of electron within this tube is the TEC value. The unit of TEC is TECU, and 1 TECU is defined as  $10^{16}$   $e^-/m^2$ .

The ionospheric delay  $\phi_{iono}$  can be express as:

$$\phi_{iono} \equiv \alpha_f STEC \quad (4.8)$$

where  $\alpha_f$  is a scaling factor. Eq.(4.8) is also referred as the First Order Ionospheric Effect and can be denoted as  $I1_f \equiv I_f$ . Eq. (4.8) can be further written in eq. (4.9) when we specific the scaling factor:

$$\phi_{iono} \approx 2\pi \frac{K}{cf} STEC \quad (4.9)$$

In this case, the dependence of refraction index with magnetic field  $B$  has been neglected (Sanz et al., 2011). By considering this term, we can obtain a higher order ionospheric effect.

Second Order Ionosphereic Effect was mentioned and described in (Hernández-Pajares, Juan, Sanz & Orús, 2007). By considering the magenetic field  $B$ , phase and code measurements will be like:

$$I2_{ph,f} = -\frac{7527}{2f^3} \int_{gr}^{sat} N_e B \cos \theta dl \quad I2_{gr,f} = -2I2_{ph,f} \quad (4.10)$$

where  $B$  is the magnetic field model of the earth and  $\theta$  is the angle between  $B$  and the propagation direction. According to Sanz et al. (2011), the second order ionospheric term has less then 0.1% of the total effect in GPS application, and by satellite clock estimation and orbit estimation in GPS related applications, this effect shall be taken into consideration.

#### 4.2.2 Faraday Rotation Effect

Polarization of the SAR signal defines the vibration direction of the signal. When signal travels through ionosphere, the different propagation velocities of left- and right- handed signals causes the phase differences between polarization (Meyer et al., 2008). This effect is called faraday rotation (FR) effect. The magnitude of FR with respect to carrier frequency

$f$  for one way travel can be given by:

$$\Omega = -2\pi f \frac{1}{10^6} \int \frac{N_{iono}(f, h)}{c} \frac{f_h}{f} \cos(\theta) dh = \frac{K}{f^2} B \cos(\theta) STEC \quad (4.11)$$

where  $f_h$  represents electron gyrofrequency with  $f_h = B \cdot e / 2\pi \cdot m$ ,  $B$  is the local geomagnetic field. FR effect mainly affects polarimetric SAR (POL-SAR) data applications. A method of FR estimation has been developed by Meyer et al. (2008). Since this thesis focus on InSAR applications, we don't go into detail with FR effect correction.

### 4.2.3 Ionospheric Phase Shift in InSAR

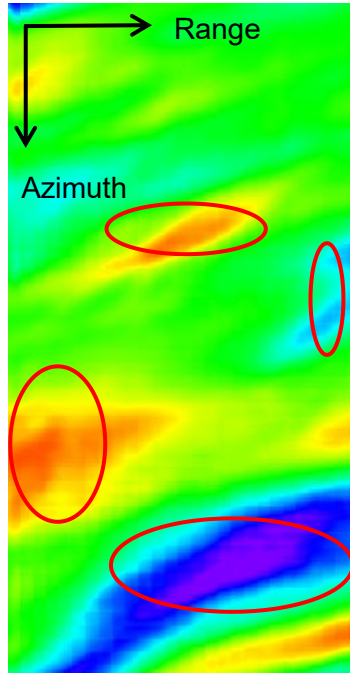
In L-band data based InSAR applications, the major error that brought by ionosphere is the phase shift i.e. first order ionospheric effect. Here we use  $\phi_{iono}$  to denote the phase. The phase shift in two way along the propagation is then given according to eq. (4.9):

$$\phi_{iono} = -\frac{4\pi K}{cf_0} STEC \quad (4.12)$$

The minus sign again represents the phase advance i.e. negative delay brought by ionosphere. The  $f_0$  is the center frequency of carrier phase.

According to Meyer et al. (2006), ionospheric effects in a SAR image can be separated according to their causes:

(1) Phase advance: This group of error is caused by the phase advance; it contains 1) a slope in range direction caused by a range depended signal-path length in ionosphere; 2) blurring effect caused by small-scaled electron density inhomogeneties; and 3) phase gradient cross azimuth chirp caused by azimuth shift. Fig. 4.3 and fig. 4.4 demonstrates azimuth shift caused ionospheric errors in our test observation. In these pairs we can clearly see the de-correlation caused by ionospheric variation in coherence map. The phase gradient error is the most obvious type that we obtained in our example.

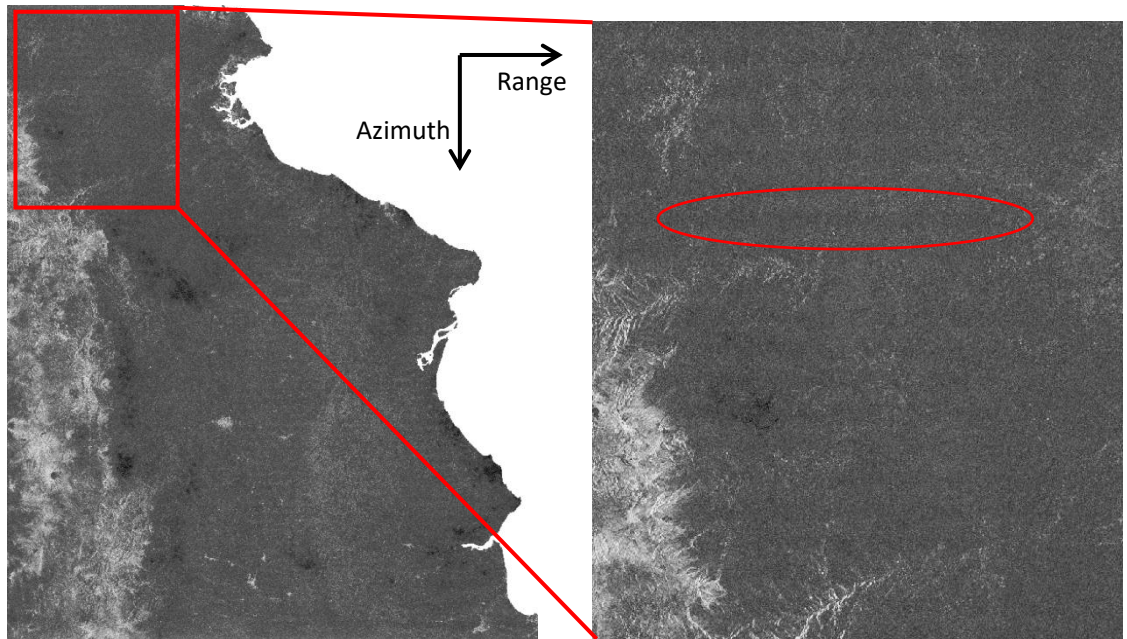


(a)



(b)

Figure 4.3: Example of azimuth streaks caused by ionospheric error on ALOS PALSAR data (a) Azimuth shift phase generated by using MAI based method and (b) Coherence map of our test area located in Alaska. Red circles marked out in (a) the azimuth shift phase gradient and in (b) “Azimuth streak” (Matter & Gray, 2002) i.e. the de-correlated stripes caused by ionosphere pattern. A linear relationship between them can be seen from this example.



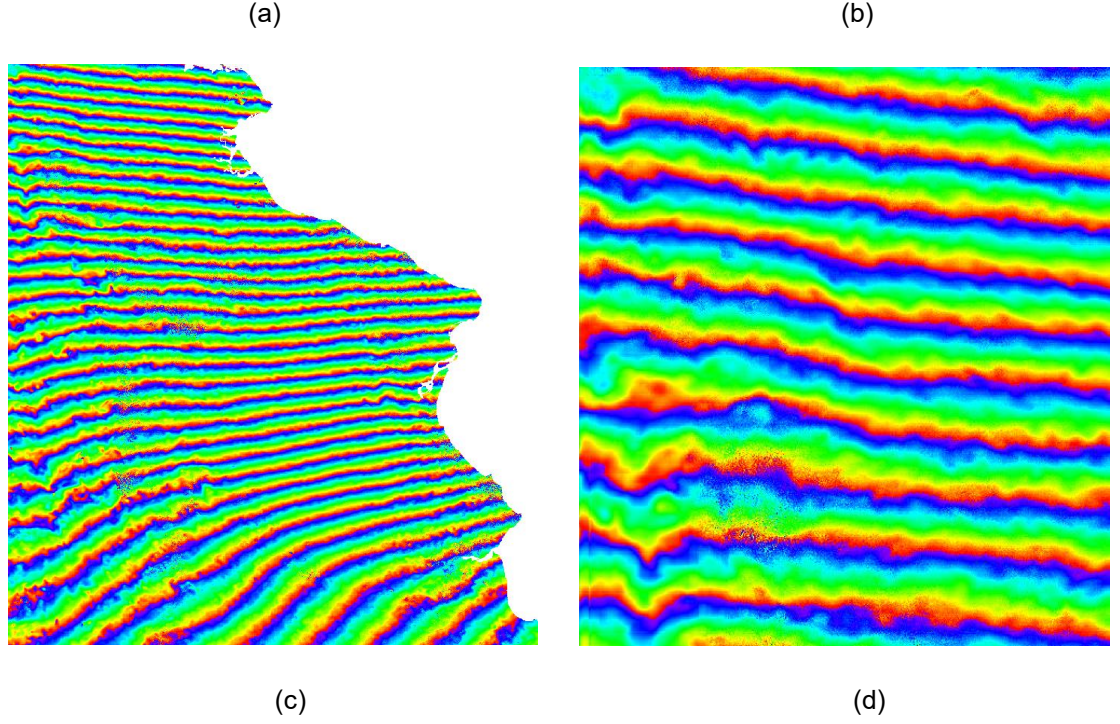


Figure 4.4: Example of azimuth streaks caused by ionospheric phase shift on ALOS-2 data (a) Coherence map of test site Ecuador (b) Zoomed coherence map of this area where we can see the low coherence azimuth streak along range direction and (c) wrapped interferogram and (d) zoomed interferogram of this area, we can see residual phases along the same direction as those azimuth streak in (b).

(2) Group delay: Local geometric distortions of SAR images that are caused by spatial TEC variance. This is usually along range direction.

(3) Nonlinear phase term: Residual phase ramp in interferogram. This term is not modeled by linearization via phase and code refraction. This is because of the carrier frequency bias from center carrier phase frequency. According to Meyer et al. (2006), this can be described as an approximately quadratic form as:

$$\delta\phi_r(f) \approx \frac{4\pi}{c_0} \frac{K}{f_0^3} TEC (f - f_0)^2 \quad (4.13)$$

This residual phase ramp has a trend which is usually in range direction (Meyer et al., 2006). Meyer et al. (2006) described this phase as “quadratic phase error”, and according to their description, the maximal quadratic phase error happens usually at the margins of



the azimuth chirp.

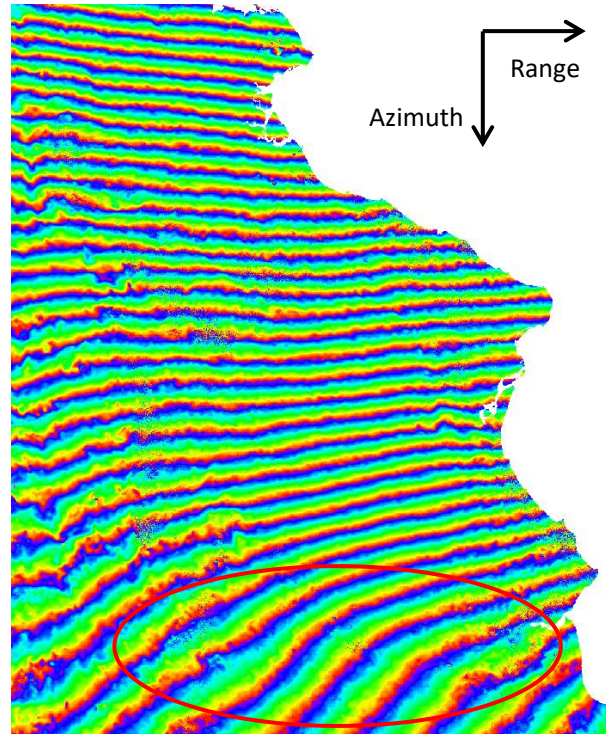


Figure 4.5: Quadratic ionospheric error. Wrapped interferogram of Ecuador, in the red circle we see a residual phase ramp that no longer along azimuth direction appears to be along the range trend.

In this thesis, according to test SAR data, I focused on dealing with the azimuth shift phase caused by phase advance and the residual phase ramp in generated interferogram.

### 4.3 Residual Phase Removal

Residual phase is a kind of synthetic phase that can be seen as a ramp in generated unwrapped interferogram. This phase is not related to real deformation of the ground but can be created by many reasons e.g. topography, orbit error, or ionosphere.

A residual phase can be modeled by using a polynomial of a low degree e.g. degree of 2 to remove orbit error (Liu et al., 2014). Similarly, a polynomial of low degree can also be used to remove ionospheric residual phase. The modeled residual phase is defined by the polynomial degree from 1 to 10 by :

$$\phi_R = K_1 + K_2X + K_3Y + K_4X^2 + K_5XY + K_6Y^2 + K_7X^3 + K_8X^2Y + K_9XY^2 + K_{10}Y^3 \quad (4.14)$$

Parameters from  $K_1$  to  $K_{10}$  are estimated by a polynomial fit process from input data. The interferometric phase can be estimated by using original interferogram to subtract the modeled residual phase. For this method, it is important to select the ground control points (GCPs) as input and to set the right degree for the process.

## 4.4 GPS based Ionospheric Phase Estimation

### 4.4.1 GPS Signal

GPS's carrier phase is also in L-band, Therefore it's signal is also sensitive to ionosphere. There 3 carrier frequencies in GPS's system, they are  $L_1$ ,  $L_2$  and  $L_5$ . It has 2 ranging codes: (1) civilian clear/acquisition (C/A code) or L2C code, and (2) restricted precise/protected (P) code. Fig. (4.6) shows the structure of GPS's signal:

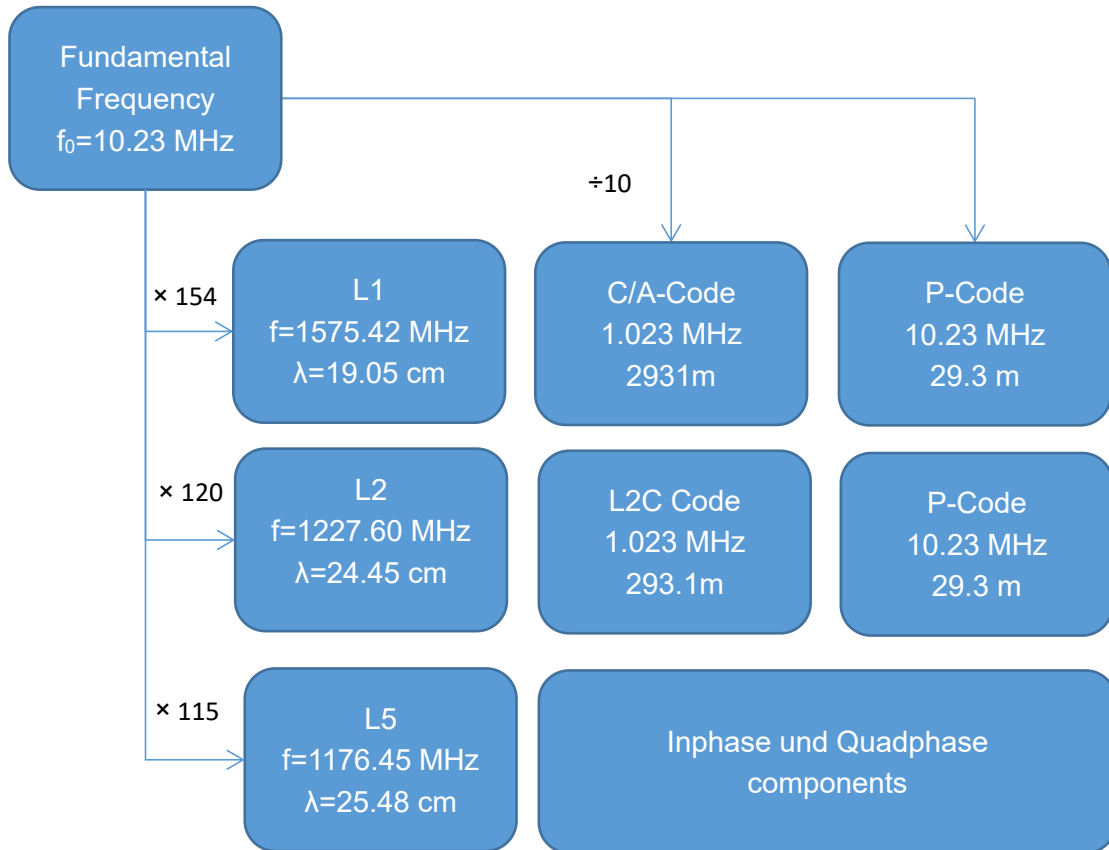


Figure 4.6: Structure of GPS signal.

From eq. (4.6) we can see that the phase advance and group delay effect are equivalent in distance. The first order ionospheric effect on code and carrier phase depend on  $f^2$ . Combining  $L_1$  and  $L_2$  bands, a ionosphere free linear combination can be applied ((Sanz , Juan Zornoza & Hernández-Pajares, 2011):

$$\Phi_{iono-free} = \frac{f_1^2 \Phi_{L1} - f_2^2 \Phi_{L2}}{f_1^2 - f_2^2} \quad R_{iono-free} = \frac{f_1^2 R_{P1} - f_2^2 R_{P2}}{f_1^2 - f_2^2} \quad (4.15)$$

#### 4.4.2 GPS based TEC Measurement

The first order ionospheric effect fractions of code and carrier phase are shown as eq. (4.6) can also be written as:

$$\Delta_{ph,f}^{iono} = -\frac{K}{f^2} \cdot TEC \quad \Delta_{gr,f}^{iono} = +\frac{K}{f^2} TEC \quad (4.16)$$

For a better notation, we use further  $TEC$  to represent  $STEC$  along the slant range of propagation from the receiver to the satellite. If we convert phase shift into meter, we can combine these two measurements once we have the position of ground stations, and with these measurements we can estimate  $TEC$  values.

Let's take code measurements as examples. For one ground station, we have two pseudorange measurements  $\rho_{L1}$  and  $\rho_{L2}$ ; two carrier phases  $L_1$  and  $L_2$ . According to eq.(4.16), for 1 TECU, there is 0.163 m on  $L_1$  and 0.267 m on  $L_2$ . The TEC value then can be calculated by (Dyrud et al., 2008) :

$$TEC_{\rho} = \frac{\rho_{L2} - \rho_{L1}}{0.104mTECU^{-1}} \quad (4.17)$$

In eq. (4.17),  $TEC_{\rho}$  is regarded as the absolute TEC measurement, but the result is noisy due to the pseudorange measurement by code is not precise (in meter level).

For carrier phase measurement we can estimate the TEC similarly:

$$TEC_{\phi} = \frac{-\phi_{L2} + \phi_{L1}}{0.104mTECU^{-1}} \quad (4.18)$$



Carrier phase measurement is more precise than code measurement, it's TEC result is therefore much smoother than code generated results. However, due to the ambiguities from phase measurement, this TEC result is not absolute, but relative. In order to get a smoother and absolute TEC measurement, we have to combine code and phase together. A typical way to do this is to use least square fitting on phase-derived TEC and code-derived TEC. The parameter that has to be estimated is the so-called TEC offset, which is the DC offset (mean amplitude displacement from zero) between phase derived TEC and code derived TEC. The final TEC value can then be calculated by:

$$TEC_{final} = TEC_{\phi} - TEC_{offset} \quad (4.19)$$

To improve the TEC result, Dyrud et al. (2008) proposed improvement of eliminating 3 biases during estimating process. Here we don't go into detail of this study. For our experiments, we used TEC product generated from CODE.

### 4.3.1 CODE Product

Center for Orbit Determination in Europe (CODE) is operated by the American International University-Bangladesh (AIUB) since 1992 and more information about CODE institute can be read from website :(  
[http://www.aiub.unibe.ch/research/code\\_\\_\\_analysis\\_center/index\\_eng.html](http://www.aiub.unibe.ch/research/code___analysis_center/index_eng.html) ).

CODE provides global covered ionospheric map daily in grid :

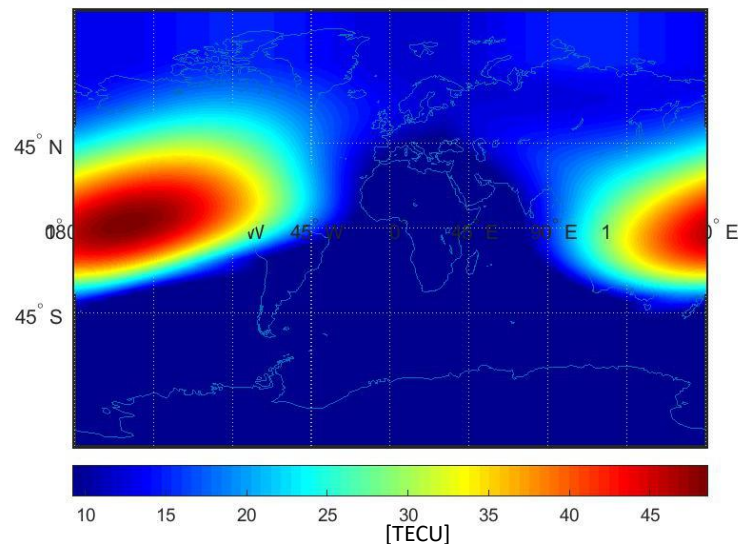


Figure 4.7: Global covered TEC map , daily based product. On date 01,04,2016.

The daily product is smoothed and set the UTC time at 0:00 of everyday, so that the TEC concentration is on pacific ocean. To get ride of the ionospheric effect in SAR applications, this product is not sufficient because TEC values are changing from hour to hour, therefore we must use TEC map on the same time that the data was acquired.

CODE also provides hourly based global covered TEC map. To reduce the data volume they were stored in spherical harmonics coefficients (SHC) from degree and order of 0 to degree and order of 15, an example shown below present how CODE product looks:

```

CODE'S GLOBAL IONOSPHERE MAPS FOR DAY 092, 2016                                05-APR-16 20:06
-----
MODEL NUMBER / STATION NAME : 0920-01
MODEL TYPE (1=LOCAL,2=GLOBAL,3=STATION) : 2
MAXIMUM DEGREE OF SPHERICAL HARMONICS : 15
MAXIMUM ORDER : 15
DEVELOPMENT WITH RESPECT TO
  GEOGRAPHICAL (=1) OR GEOMAGNETIC (=2) FRAME : 2
  MEAN (=1) OR TRUE (=2) POSITION OF THE SUN : 1
MAPPING FUNCTION (0=NONE,1=COSZ,2=MSLM,3=ESM) : 2
HEIGHT OF SINGLE LAYER AND ITS RMS ERROR (KM) : 450.00      0.00
COORDINATES OF EARTH-CENTERED DIPOLE AXIS
  LATITUDE OF NORTH GEOMAGNETIC POLE (DEGREES) : 80.33
  EAST LONGITUDE (DEGREES) : -72.67
PERIOD OF VALIDITY
  FROM EPOCH / REFERENCE EPOCH (Y,M,D,H,M,S) : 2016 04 01 00 00 00
  TO EPOCH :
LATITUDE BAND COVERED
  MINIMUM LATITUDE (DEGREES) : -87.88
  MAXIMUM LATITUDE (DEGREES) : 89.84
ADDITIONAL INFORMATION
  NUMBER OF CONTRIBUTING STATIONS : 256
  NUMBER OF CONTRIBUTING SATELLITES : 55
  ELEVATION CUT-OFF ANGLE (DEGREES) : 10
  MAXIMUM TEC AND ITS RMS ERROR (TECU) : 66.03      0.64
COMMENT / WARNING :
COEFFICIENTS
DEGREE  ORDER  VALUE (TECU)  RMS (TECU)
0       0       16.46085074  0.0309
1       0       1.63564342  0.0293
1       1       8.36758337  0.0318
1      -1       5.17497454  0.0295
2       0      -7.07921600  0.0290
2       1       0.18630247  0.0303
2      -1       0.63733346  0.0285
2       2       1.34636070  0.0296
2      -2       1.76797830  0.0298
3       0      -1.53098644  0.0265
3       1      -2.43417589  0.0309
3      -1      -1.83360367  0.0288
3       2       0.06743218  0.0286
3      -2       0.69187080  0.0285
3       3      -0.90255206  0.0295
3      -3      -0.54543129  0.0291
4       0       2.99144902  0.0281
4       1      -0.35943413  0.0276
4      -1      -0.42995623  0.0265
4       2      -0.76034250  0.0302

```

Figure 4.8: CODE hourly based product.

This file contains products from epoch 0:00 to 23:00 UTC of the data. In order to extract the global covered TEC map and increase the resolution, a spherical harmonics expansion shall be applied (Müller, 2016, slide 5):

$$V = \sum_{l=0}^{l_{\max}} \left( \frac{a}{r} \right)^l \sum_{m=0}^l \left( \bar{C}_{l,m} \cdot \cos m\lambda + \bar{S}_{l,m} \cdot \sin m\lambda \right) \bar{P}_{l,m}(\cos \theta) \quad (4.20)$$

where  $V$  is the field we want to express,  $l, m$  degree and order.  $r, \lambda, \theta$  are spherical coordinate of point P,  $\bar{C}_{l,m}$  and  $\bar{S}_{l,m}$  are spherical harmonics expansion coefficients,  $\bar{P}_{l,m}$  is the fully normalized legendre functions.

After spherical expansion and a proper interpolation, the global covered TEC map can be recovered:

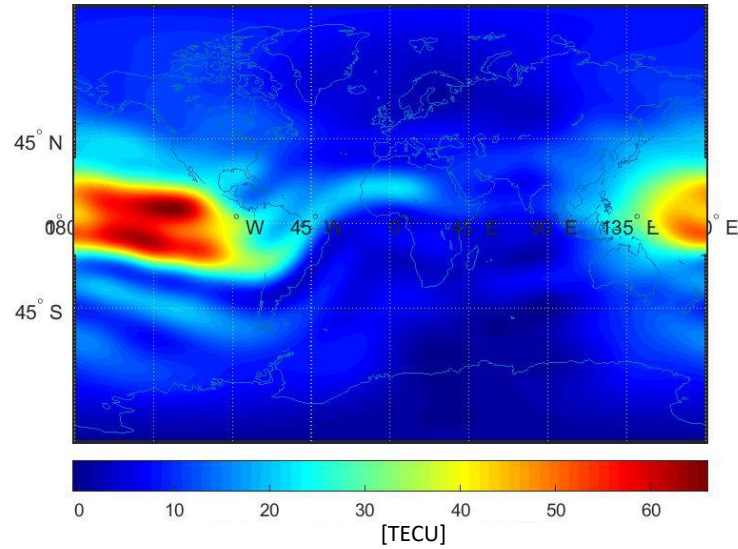


Figure 4.9: Global covered TEC map, hourly based product, at 0:00 UTC. On date 01,04,2016.

Hourly based products provide us a map that close to the acquisition time. When TEC value is retrieved from the global TEC map, we can calculate the ionospheric shift phase according to eq. (4.12).

## 4.5 Azimuth Shift Based Ionospheric Phase Estimation

As discussed in section 4.2.3, the first order ionospheric effect is the major error in

InSAR application. In generated SAR interferogram, one of the most common ionospheric effect is the azimuth shift caused by ionosphere. This phenomenon is the first reported ionospheric error type in InSAR application by Grey et al. (2000).

Considering the signal is propagating along a straight line, we used a simple projection function to project TEC value from vertical TEC to slant TEC, eq. (4.12) then became:

$$\phi_{iono} = -\frac{4\pi K}{cf_0} \frac{1}{\cos \theta} VTEC \quad (4.21)$$

In interferogram generation process, we generated the differential phase from master and slave images. In order to get rid of ionospheric phase in interferogram, the differential ionospheric phase should also be generated, then eq. (4.21) can also be written as:

$$\Delta\phi_{iono} = -\frac{4\pi K}{cf_0} \frac{1}{\cos \theta} \Delta VTEC \quad (4.22)$$

where  $\Delta VTEC$  is the TEC variance.

For correcting this first order ionosphere effect, a linear relationship between azimuth shift and ionospheric phase is introduced (Matter & Gray, 2002):

$$\phi_{iono} = \alpha \int \Delta x_{shift} dx + c \quad (4.23)$$

where  $\alpha$  is a scaling factor,  $\Delta x_{shift}$  is the azimuth shift, and  $c$  is the constant term of this integration. To determine the ionospheric phase,  $\alpha$  need to be estimated.

From eq. (4.22) and eq. (4.23), we can generate the first derivative of ionospheric phase with respect of azimuth direction  $x$  as:

$$\frac{d\phi_{iono}}{dx} = \alpha \frac{4\pi}{\lambda} \Delta x_{shift} \quad (4.24)$$

We assume that there is no obvious deformation and fringes that obtained in our area are all caused by ionosphere, We can transfer eq. (4.24) into eq. (4.25). When we have the azimuth shift and the azimuth derivative from InSAR phase with respect to azimuth direction, we can estimate  $\alpha$  and  $\beta$  (i.e linear parameters) by applying a polynomial fit on

them:

$$\frac{\Delta\phi_{InSAR}(x,r)}{\Delta_{az}} = \alpha\Delta x_{shift} + \beta \quad (4.25)$$

and once we estimate this linear relationship, the ionospheric phase can be calculated by integrating scaled azimuth shift along azimuth direction using eq. (4.23) and the generated ionospheric phase can be subtracted from SAR interferogram to get rid of ionospheric error from SAR interferogram. To achieve this, the most important step is to generate azimuth shift. In this thesis, two ways to generate azimuth shift are introduced, they are (1) AT based method and (2) MAI based method.

### 4.5.1 Amplitude Tracking based Method

Azimuth tracking based method is based on amplitude cross correlation. It is a technique to find conjugate points from two images with an overlap area. It is applied a lot in photogrammetry and optical remote sensing applications. This method is implemented on amplitude measurements because it also contains local texture (i.e. scattered information) of objects on testing site.

After finding a pair of conjugate points in an image pair i.e. amplitude images from master and slave, a shift between them can be measured in pixel's aspect and can be translated into real size scale and decomposed into range direction and azimuth direction. In doing this, we can generate azimuth shift from every pixel that are good correlated.

#### 4.5.1.1 Cross-correlation and Coherence

Cross correlation set two windows, which are matrix around target point. The size of the matrix is called window's size. One window defines the point and its neighbors, the other window moves all over the other image to find the point that has the highest similarity with respect to the first window. A normalized cross correlation (NCC) coefficient is defined to represent the similarity of two points (Heipke, 2016) :

$$NCC = \frac{\sum_{r=1}^R \sum_{c=1}^C (g(r,c)' - \bar{g}') (g(r,c)'' - \bar{g}'')}{\sqrt{\left( \sum_{r=1}^R \sum_{c=1}^C (g(r,c)' - \bar{g}')^2 \right) \left( \sum_{r=1}^R \sum_{c=1}^C (g(r,c)'' - \bar{g}'')^2 \right)}} \quad (4.26)$$

where  $r$  and  $c$  indicates the row and column index of the pixel in the image system, the  $g$  mean the corresponding gray value of the pixel.

Amplitude cross correlation process is purely based on amplitude measurement form SAR. In order to increase the accuracy of points tracking, two steps shall be applied separately, first a coarse process with a relative large window, and then apply a smaller window for a finer process. This method can also help to restore the corresponding pixels into the right position, it is also called coregistration process.

After coregistration, the correlation between two pixels at the same position is measured, the value of it is between 0 and 1, this is called coherence (Motagh, 2017):

$$\gamma = \frac{E[ms^*]}{\sqrt{E[mm^*]E[ss^*]}} \quad \gamma = |\gamma| e^{-i\phi} \quad (4.27)$$

where  $\gamma$  is the calculated coherence,  $E$  is the expectation calculator,  $\phi$  is the interferometry phase,  $m$  and  $s$  represents co-registrated complex image values from SAR data.

The higher the coherence, the higher the similarity of pixels are. Low value of coherence demonstrate a decorrelation of the pixel pair. Low coherence can be caused by e.g. vegetation growing and in this thesis, mostly by ionospheric error.

#### 4.5.1.2 Ionospheric Phase Estimation based on AT

Azimuth shift  $\Delta x_{shift}$  can be generated by amplitude cross correlation in meter. When azimuth derivative from InSAR phase is calculated from the generated interferogram,  $\alpha$  and  $\beta$  in eq.(4.25) can be estimated by applying a polynomial fit and the corresponding ionospheric phase can then be estimated.

This method can only be applied when there is no obvious deformation happened in study area, because the dispersive and non-dispersive phases are hard to be separated. The detailed processing flow and implementation of this method shall be discussed in following chapters.

## 4.5.2 Multiple Aperture Interferogram based Method

### 4.5.2.1 Multiple Aperture Interferogram

The main principle of MAI technique is separating full aperture of single look complex (SLC) image into two apertures: (1) forward-looking aperture and (2) backward-looking aperture. This process modified the doppler centroid and reduced doppler bandwidth into half of the full one (Jung et al, 2009):

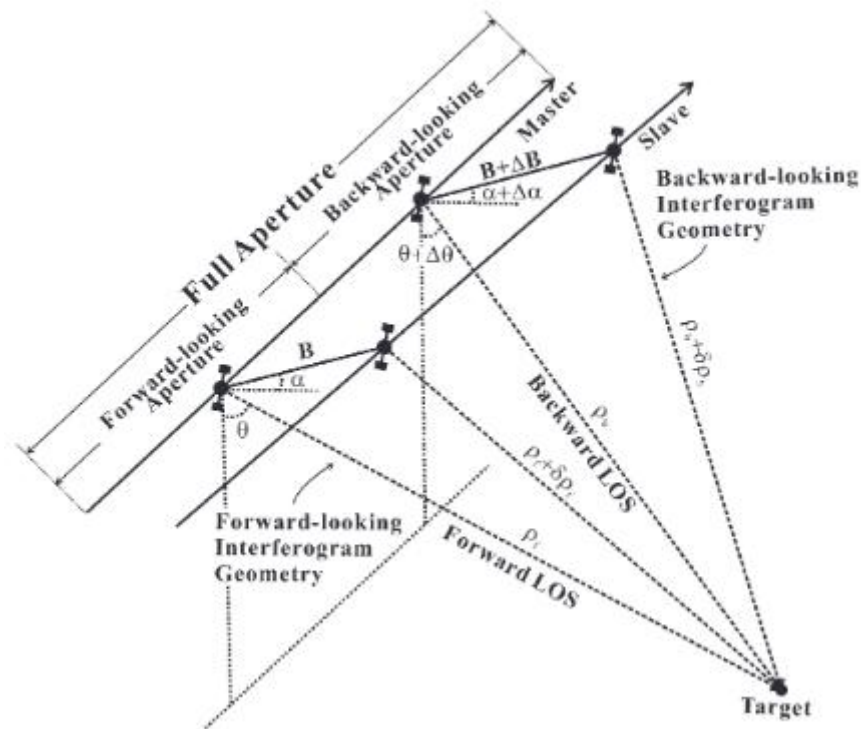


Figure 4.10: MAI geometry of forward- and backward-looking interferograms. Reprinted from “An Improvement of Performance of Multiple-Aperture SAR Interferometry (MAI),” by H. S. Jung, J. S. Won, and S. W. Kim, 2009, *IEEE Transactions on Geoscience and Remote Sensing*, 47(8), 2859-2869.

This figure shows the geometry of forward and backward looking interferogram, where  $B$  is the baseline length,  $\rho$  represents the slant range distance. The author demonstrated this figure in (Jung et al, 2009) to discuss the flat-earth and topography effect caused by the change of the baseline. Here we don't go into deep of this part, but only introduce the main principle of MAI.

In order to generate forward- and backward- looking SLC image, four images are formed: forward-looking and backward-looking SLCs for each master and slave image. Interferograms are generated from both forward-looking image pair and back-looking image pair from both side (master and slave). Afterward, like interferogram generation, a complex conjugate multiplication are applied on these two generated forward- and backward-looking interferograms to produce the final MAI interferogram:

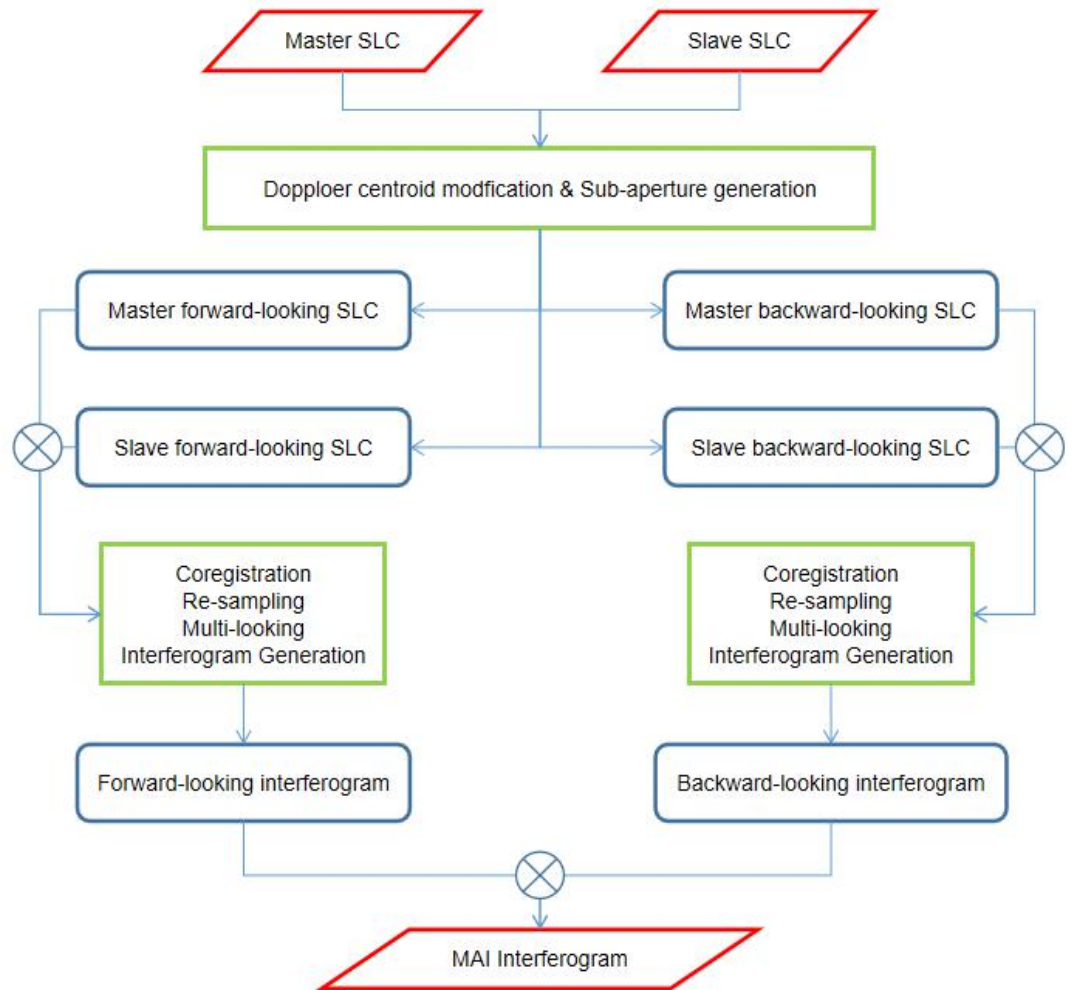




Figure 4.11: Working flow of MAI generation.

Fig. 4.11 demonstrates the MAI generating process. The phase image of MAI interferogram is the differential phase between forward-( $\phi_f$ ) and backward looking ( $\phi_b$ ) interferograms:

$$\phi_{MAI} = \phi_f - \phi_b = -\frac{4\pi}{l} n \Delta x_{shift} \quad (4.28)$$

$\Delta x_{shift}$  is the azimuth displacement of the surface,  $n$  is the normalized squint to present the fraction of full aperture width with  $n = 0.5$  (after aperture separation we have half of the aperture).  $l$  is the effective antenna length.

Eq. (4.28) shows the relationship between MAI phase and azimuth shift. However, there is a disadvantage of this method, that is, when we reduce the length of aperture, according to eq. (4.1), we lose azimuth resolution of our image. The signal to noise ratio (SNR) is also reduced similarly. Therefore, to generate MAI interferogram, we need image pair with higher coherence comparing to generating full aperture interferogram.

#### 4.5.2.2 Ionospheric Phase Estimation based on MAI

According to eq. (4.25), the azimuth shift can be generated by MAI phase by:

$$\Delta x_{shift} = -\frac{l}{4\pi n} \phi_{MAI} \quad (4.29)$$

We substitute  $\Delta x_{shift}$  in eq. (4.24), we can obtain:

$$\frac{d\phi_{iono}}{dx} = -\alpha \frac{l}{n\lambda} \phi_{MAI} \quad (4.30)$$

Eq. (4.30) denotes the linear relationship between MAI phase and the first derivative of ionospheric phase with respect to ionospheric phase. Similar like AT based method, after we estimated the scaled parameter  $\alpha$  and  $\beta$  by using eq. (4.25), the ionospheric phase can be calculated by integrating scaled MAI phase along azimuth direction accordingly:

$$\phi_{iono} = -\alpha \cdot \frac{l}{n\lambda} \cdot \int \phi_{MAI} dx \quad (4.31)$$

Like AT based method, this method is also restrict to the applications where there was no large surface deformation, other wise pixels with large deformation shall be excluded e.g. by applying threshold on generated SAR interferogram.

## 5 Methodologies

In this chapter methods; the processing working flows; and tools for implementations were introduced. In section 5.1 residual phase removal method is first introduced, and then in section 5.2 the process of generating CODE products and how to implement ionospheric correction based on CODE products is shown. Because the process of AT based method and MAI based method are similar, they are combined and are discussed in section 5.3.

### 5.1 Residual Phase Removal

Residual phase removal was applied on ALOS-2 data set that locates in Ecuador. Three pairs of SAR image were processed and 3 interferograms were generated correspondingly.

During interferogram generation, the coherence maps from it was also generated. After that, a ground control points (GCPs) sets were generated from phase image. 3 criteria should be considered by selecting GCPs:

- GCPs should locate in area where there is no large deformation.
- GCPs should have high coherence according to coherence map.
- GCPs should not be only concentrated in one area, it is better to set them all over the map with a certain density.

GCPs shall served as input of estimating polynomial. In order to estimate the specific amount of parameters, the number of them should be more than the number of estimated parameters. The more input points we have, the better the estimated result is.

In this thesis, degree of 3, 5, 7 and 9 were tested for each pair of image. The generated residual phase were then removed from the InSAR phase.

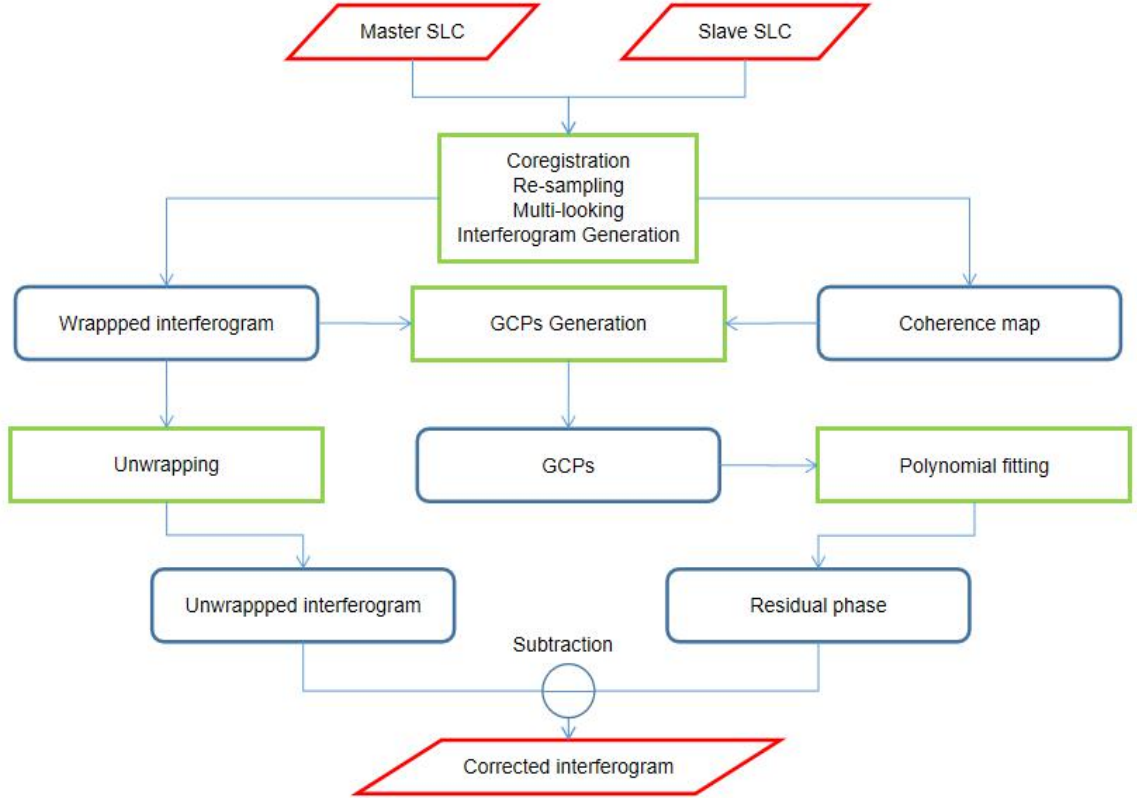


Figure 5.1: Working flow of residual phase removal strategy.

The implementation was done by ENVI version 5.4.1, SARscape software (Exelis Visual Information Solutions, Boulder, Colorado) and details will be discussed in the following chapter.

## 5.2 CODE based Ionospheric Phase Correction

CODE product can be downloaded from : “<ftp.auib.unibe.ch/CODE/IONO>.” One CODE daily product file contains TEC measurements from GPS from 0:00 to 23:00 UTC. They are stored as SHCs with degree and order from 0 to 15. To restore the TEC global covered map, a SH expansion was applied. Afterward, TEC map of master acquisition shall be subtracted from TEC map of slave in order to generate the TEC variance map. The TEC variance is actually a VTEC variance, it need to be re-projected into slant range direction by including the incident angle of ALOS-2.

Slant TEC variance can be used to calculate ionospheric phase according to eq. (4.12). A corrected SAR interferogram can be generated by subtracting ionospheric phase

form original unwrapped interferogram.

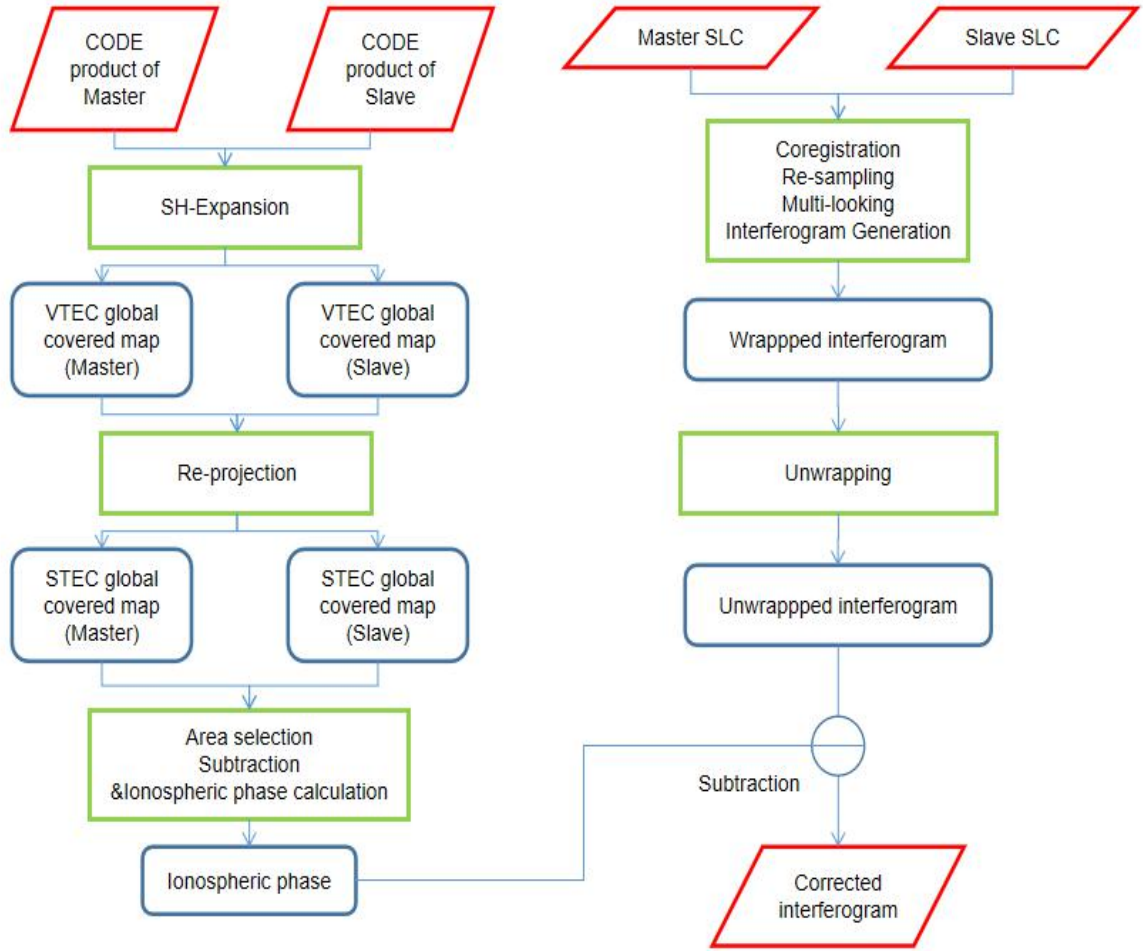


Figure 5.2: Working flow of CODE based ionospheric phase correction.

While CODE based ionospheric phase correction on ALOS-2 data was applied, it can not be applied on ALOS-1 PALSAR data because considering the preserved TEC map was only up to 5 degree in longitude and latitude, this resolution is not sufficient for small scaled image. The detailed information of data will be discussed in chapter 6.

The SH expansion was applied using Python programming language version 3(Python Software Foundation, <https://www.python.org/>) and further calculation was implemented by MATLAB (The MathWorks, Inc., Natick, Massachusetts, United States).

### 5.3 Azimuth Shift based Ionospheric Phase Correction

As discussed in section 4.5, there are two important step for azimuth shift based

ionospheric phase correction: (1) Azimuth shift generation and (2) linear relationship estimation. AT and MAI are two ways to generate azimuth shift.

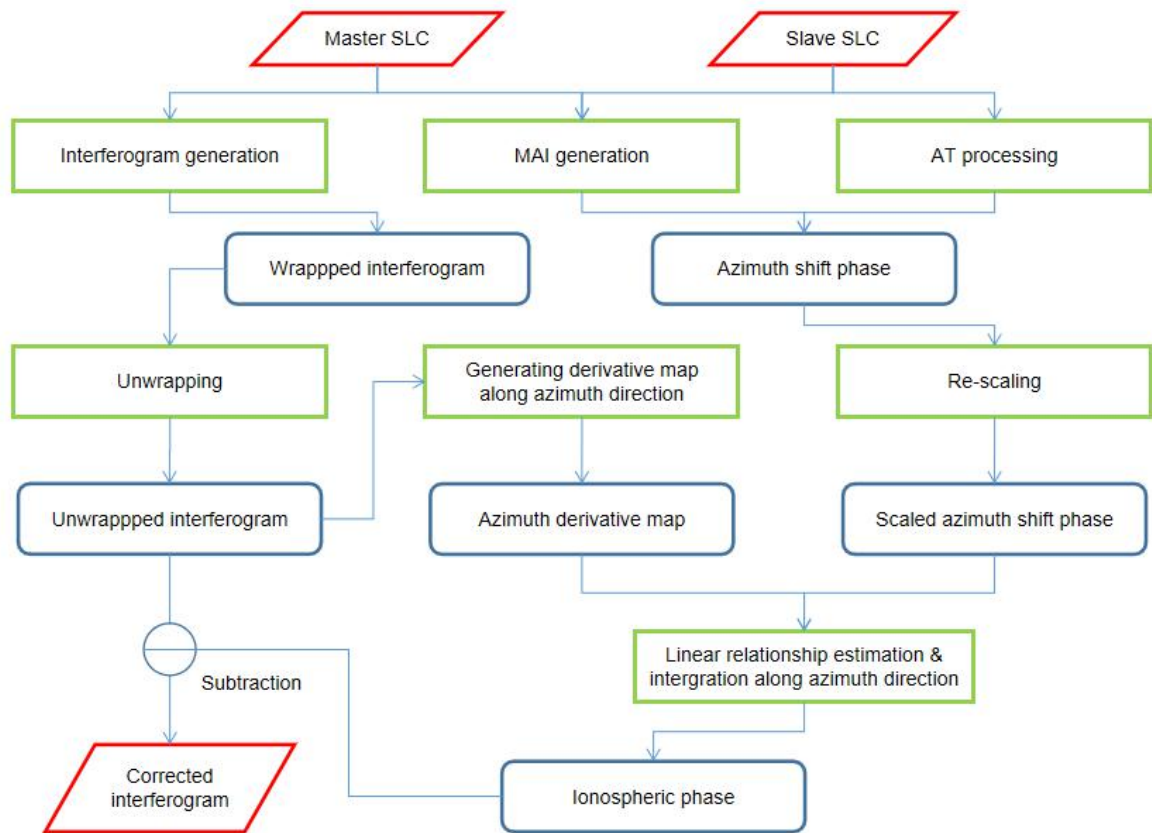


Figure 5.3: Working flow of azimuth shift based ionospheric phase correction.

AT process and MAI process implementation can be seen in section 4.5.1 and section 4.5.2. AT was applied by SARscape using “Amplitude tracking” tool box, it generates shift along both range and azimuth pixel wised. MAI interferograms were also generated by using SARscape. And further ionospheric phase calculations were implemented in MATLAB.

## 6 Data Overview

In this thesis, L-band SAR data provided by Japan Aerospace Exploration Agency (JAXA) were utilized, they are: (1) ALOS-1 PALSAR (Advanced Land Observing Satellites -1 Phase Array type L-band Synthetic Aperture Radar) and (2) ALOS-2/PALSAR-2 ScanSAR data.

### 6.1 Satellite Data Introduction

#### 6.1.1 ALOS-1 PALSAR Data

ALOS-1 satellite was launched on 24,01,2006 and was shut down on 12,05,2011. The altitude is approximately 692km above the equator, the orbit inclination is approximately  $98.2^{\circ}$ , its revisit time is 46 days. The size of the space craft is  $8.9\text{ m} \times 27.4\text{ m} \times 6.2\text{ m}$  ( $x \times y \times z$ , where  $x$  is azimuth i.e. fly direction and  $z$  is nadir direction.) and the weight is about 4000 kg.

It has three data acquisition modes: (1) fine resolution mode; (2) ScanSAR mode; and (3) Polarimetric mode. In this thesis we used polarimetric mode, all parameters regarding to it are shown in the following table ( <https://www.eorc.jaxa.jp/ALOS/en/about/palsar.htm> ):

Table 6.1 PALSAR characteristic

| Mode             | Fine              |                   | ScanSAR            | Polarimetric      |
|------------------|-------------------|-------------------|--------------------|-------------------|
| Center Frequency | 1270 MHz (L-band) |                   |                    |                   |
| Chirp Bandwidth  | 28 MHz            | 14 MHz            | 14 MHz, 28 MHz     | 14 MHz            |
| Polarization     | HH or VV          | HH+HV or VV+VH    | HH or VV           | HH+HV+VH+VV       |
| Incident angle   | 8 to $60^{\circ}$ | 8 to $60^{\circ}$ | 18 to $43^{\circ}$ | 8 to $30^{\circ}$ |

| Mode              | Fine        |             | ScanSAR              | Polarimetric |
|-------------------|-------------|-------------|----------------------|--------------|
| Range Resolution  | 7 to 44 m   | 14 to 88m   | 100m<br>(multi look) | 24 to 89 m   |
| Observation Swath | 40 to 70 km | 40 to 70 km | 250 to 350 km        | 20 to 65 km  |

*Note.* From "About ALOS PALSAR", by JAXA, retrieved from <https://www.eorc.jaxa.jp/ALOS/en/about/palsar.htm> Copyright 1997 by Japan Aerospace Exploration Agency & Earth Observation Research Center.

The geometry of ALOS-1 POLSAR is shown as:

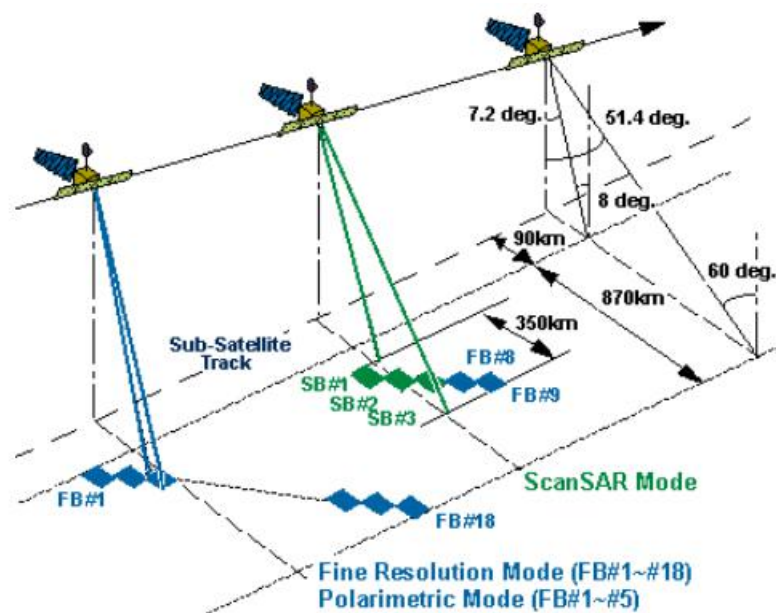


Figure 6.1: Imaging geometry of ALOS-1 PALSAR data acquisition. Reprinted from 'About ALOS-PALSAR', by Japan Aerospace Exploration Agency (JAXA) , Retrieved from <https://www.eorc.jaxa.jp/ALOS/en/about/palsar.htm>. Copyright 1997 by Japan Aerospace Exploration Agency & Earth Observation Research Center.

## 6.1.2 ALOS-2 ScanSAR data

After ALOS-1 was shut down, the second generation of ALOS satellite was launched in the same year, that was the ALOS-2, also called PALSAR-2 project. It was launched on



24, 05, 2014. The altitude of it is 628 km, the orbit inclination is 97.9° and the revisit time is 14 days. The spacecraft weights 2120 kg and has a size of 9.9 m × 16.5 m × 3.7 m (x × y × z, where x is azimuth i.e. fly direction and z is nadir direction.)

ALOS-2 has three acquisition modes, they are: (1) Spotlight mode; (2) Strip map mode; and (3) ScanSAR mode. Corresponding parameters of these three modes are shown in table (6.2) ( <https://www.eorc.jaxa.jp/ALOS-2/en/about/palsar2.htm> ):

Table 6.2 ALOS-2/PALSAR-2 characteristic

| Mode                           | Spotlight | Stripmap           |                         |                |                |       | ScanSAR             |                    |
|--------------------------------|-----------|--------------------|-------------------------|----------------|----------------|-------|---------------------|--------------------|
|                                |           | Ultrafine<br>[3 m] | High sensitive<br>[6 m] |                | Fine<br>[10 m] |       | Normal              | Wide               |
| Bandwidth<br>(MHz)             | 84 MHz    | 84 MHz             | 42 MHz                  |                | 28 MHz         |       | 14<br>MHz           | 28<br>MHz<br>z     |
| Resolution<br>(m)              | 3 m       | 3 m                | 6 m                     |                | 10 m           |       | 100 m               | 60 m               |
| Incidence<br>angle<br>(degree) | 8- 70 °   | 8- 70 °            | 8-<br>70 °              | 20-<br>40<br>° | 8-<br>70°      | 23.7° | 8- 70 °             | 8- 70 °            |
| Swath                          | 25 km     | 50 km              | 50 km                   | 40<br>km       | 70 km          | 30 km | 350 km<br>(5 scans) | 490 km<br>(7scans) |
| Polarization                   | SP        | SP/DP              | SP/DP/<br>CP            | FP             | SP/DP/<br>CP   | FP    | SP/DP               | SP/<br>DP          |

\* SP: HH or HV or VV, DP: HH+HV or VV+VH, FP: HH+HV+VH+VV, CP: compact pol.

*Note.* From "ALOS-2 Project/ PALSAR-2", by JAXA, retrieved from <https://www.eorc.jaxa.jp/ALOS-2/en/about/palsar2.htm>. Copyright 1997 by Japan Aerospace Exploration Agency & Earth Observation Research Center.

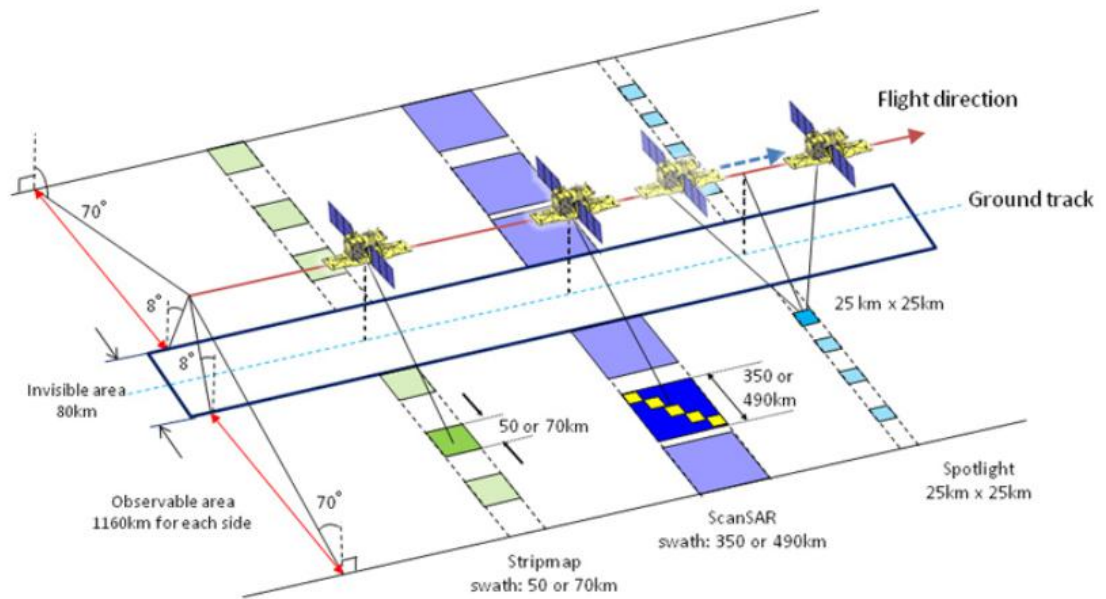


Figure 6.2: ALOS-2 Observation Mode. Reprinted from 'ALOS-2 Project/ PALSAR-2, by Japan Aerospace Exploration Agency (JAXA) , Retrieved from <https://www.eorc.jaxa.jp/ALOS-2/en/about/palsar2.htm>. Copyright 1997 by Japan Aerospace Exploration Agency & Earth Observation Research Center.

In this thesis, I used ALOS-2 ScanSAR mode data, with normal format, for each image there are 5 sub-swaths.

## 6.2 Study Area

### 6.2.1 ALOS-1 Data

According to chapter 4, ionospheric effect is easy to be seen in both equatorial area and polar area due to the sun radiation and earth magnetic field. The ALOS-1 pair that are used covers a region in northern Alaska, where magnetic field attracts the solar radiation and causes strong atmosphere ionization. There were no strong deformation during that time, therefore we can assume fringes are caused mostly by ionosphere.

This pair was reported in (Gomba, Parizzi, De Zan, Eineder, & Bamler, 2016), where they applied "split spectrum method" to identify and remove ionosphere. Here I used this pair to test our azimuth shift based method i.e. MAI based method and AT based method.

The acquisition time information for master and slave are:

Table 6.3 ALOS PALSAR data information

| Image  | Acquisition Date | Acquisition Time(UTC) | Heading   |
|--------|------------------|-----------------------|-----------|
| Master | 01 April 2007    | 07:27:36.54           | Ascending |
| Slave  | 17 May 2007      | 07:29:36.53           | Ascending |

The study area is shown in the following figure:

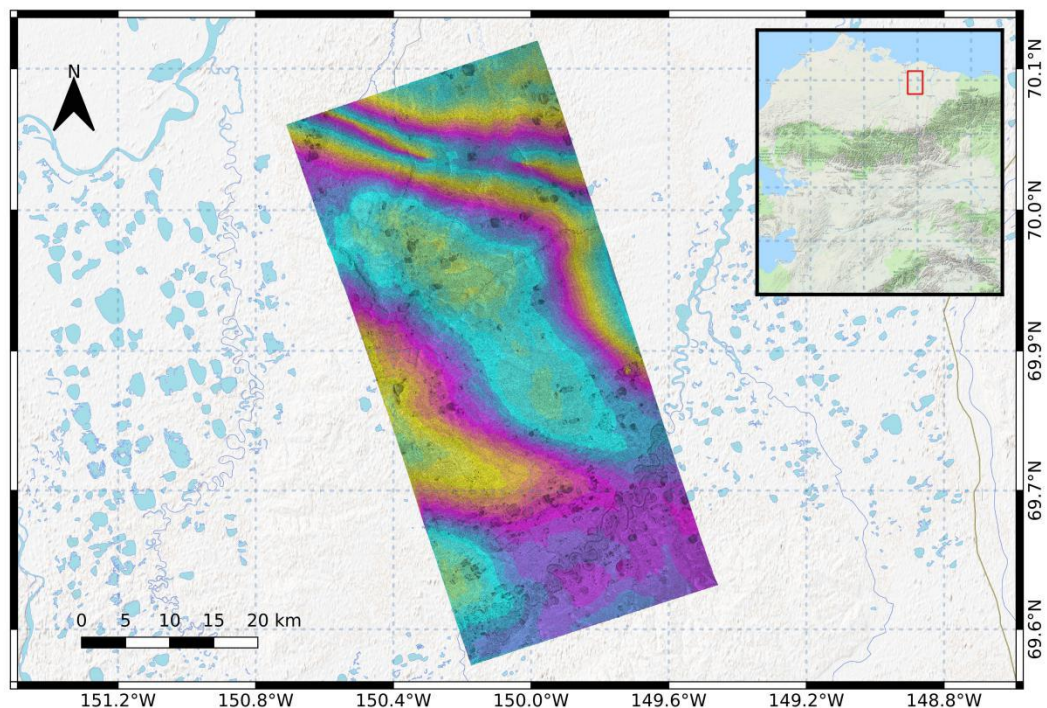


Figure 6.3: Study area in Alaska. Here we used the wrapped interferogram show our area.

## 6.2.2 ALOS-2 Data

As mentioned in chapter 2, there was a Mw 7.8 earthquake happened in 2016 in Ecuador. To analyse the pre-seismic and post-seismic deformation, a time series analysis should be applied. But in the interferograms I obtained, strong ionospheric error in most of pairs can be seen.

The sun radiation is the major reason for ionization of atmosphere. Locating in equatorial area, this study area has a lot of sun radiation. And for ALOS-2, the acquisition

time is always at around 12:00 (Local time, in our study area the UTC time is around 17:00:00) when the sun radiation is always the strongest. In this case, we should always obtain strong ionospheric error in this study area.

In this thesis, 2 pairs were selected for estimating ionospheric error, one pair is before earthquake, where there were no strong deformations, and there an assumption that most fringes were caused by ionosphere can be made. The other pair was during the earthquake where we can clearly see the co-seismic deformation from the earthquake.

Data information were shown below:

Table 6.4 ALOS-2/PALSAR -2 data information

| No.                       | Image  | Acquisition Date | Acquisition Time(UTC) | Heading    |
|---------------------------|--------|------------------|-----------------------|------------|
| 1. Co-seismic Image Pair  | Master | 01 April 2016    | 17:00:54.17           | Descending |
|                           | Slave  | 29 April 2016    | 17:00:53.47           | Descending |
| 2. Pre-seismic Image Pair | Master | 08 January 2016  | 17:00:56.24           | Descending |
|                           | Slave  | 01 April 2016    | 17:00:54.17           | Descending |

The location of study area is presented in the following figure:

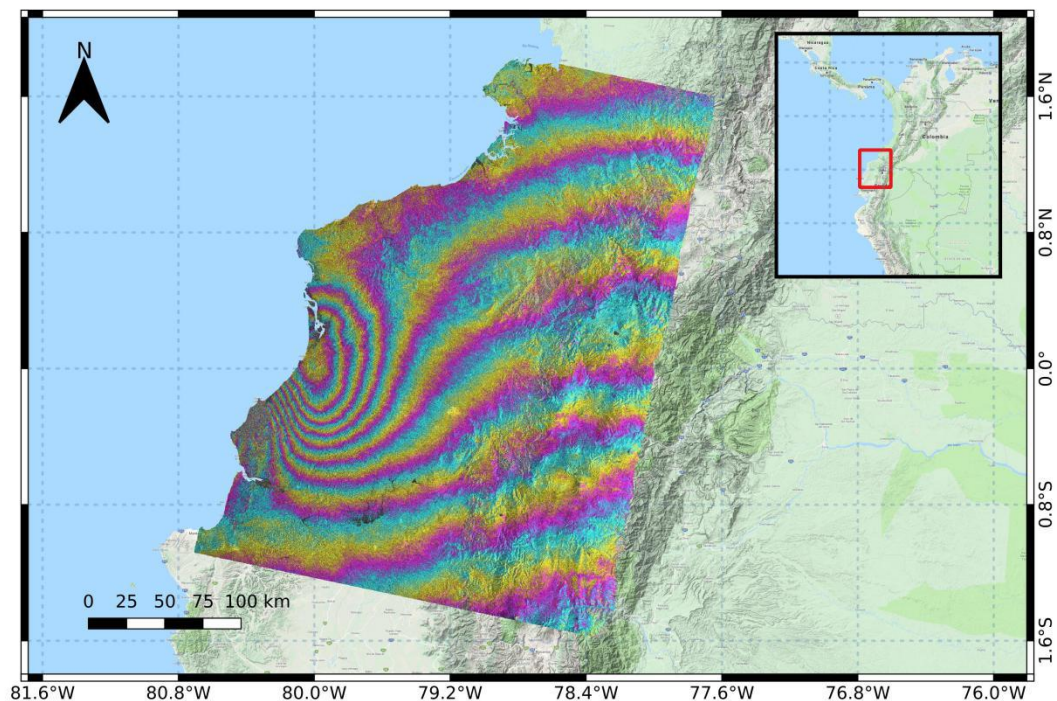


Figure 6.4: Study area in Ecuador shown in wrapped interferogram from co-seismic pair.

## 7 Experiments and Results

### 7.1 Interferogram Generation

During the implementation, topographic phase removal was done by using a digital elevation model (DEM) provided by Shuttle Radar Topography Mission (SRTM)-3 version 4 i.e. with 90 m resolution ( <http://srtm.csi.cgiar.org/> ).

For ALOS-1 data, we set the multi-look parameter as:

Table 7.1: Multi-look parameters for ALOS-1 PALSAR data

| ALOS-1 PALSAR Data     |         |
|------------------------|---------|
| Range Looks            | 1       |
| Azimuth Looks          | 7       |
| Range Resolution [m]   | 23.0334 |
| Azimuth Resolution [m] | 24.9218 |

And for ALOS-2, the setting is the same:

Table 7.2: Multi-look parameters for ALOS-2 ScanSAR data

| ALOS-2 ScanSAR Data    |         |
|------------------------|---------|
| Range Looks            | 1       |
| Azimuth Looks          | 7       |
| Range Resolution [m]   | 23.0334 |
| Azimuth Resolution [m] | 24.9218 |

All generated interferograms were filtered using a “Goldstein filter” (Goldstein, & Werner, 1998) with a filtering window in size of 256. The unwrapping process was done by applying “Minimum Cost Flow” (Costantini, 1998) with unwrapping coherence threshold of 0.2. The generated wrapped and unwrapped inteferogram is shown in Fig. 7.1; fig. 7.2 and fig. 7.3.



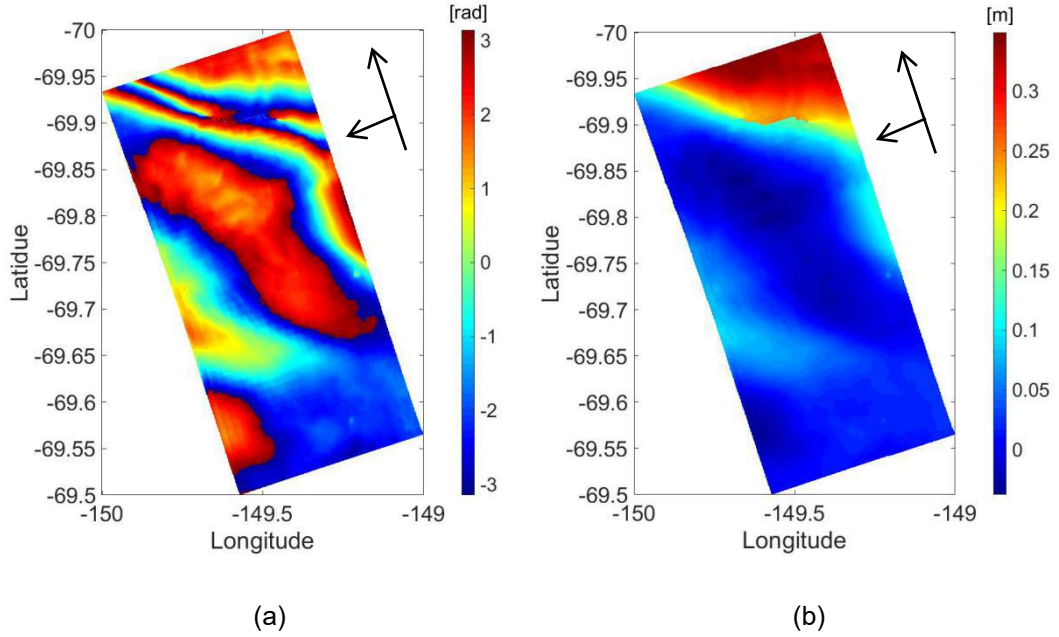


Figure 7.1: Interferogram from ALOS-1 data pair in Alaska, Master: 01, April, 2007. Slave: 17, May, 2007. (a) Wrapped interferogram in radiant and (b) unwrapped interferogram in meter.

Between these two acquisitions there was no strong crustal deformation reported in this area. However we still see fringes caused by ionosphere in wrapped interferogram and by unwrapping it we got a deformation information around 0.35 meter.

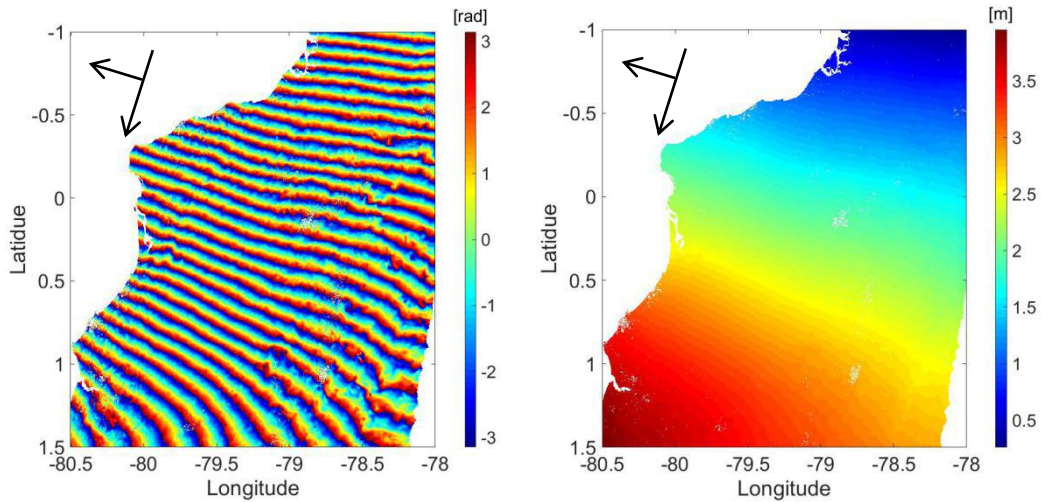


Figure 7.2: Interferogram from ALOS-2 data pair in Ecuador, Master: 08, January, 2016. Slave: 01, April, 2016. (a) Wrapped interferogram in radiant and (b) unwrapped interferogram in meter.

This pair is the pre-seismic pair before the earthquake, when there was no report or no sign of obvious surface deformation. However, lots of fringes caused by ionosphere were

seen in this interferogram and lead to a slope along the azimuth direction in unwrapped interferogram.

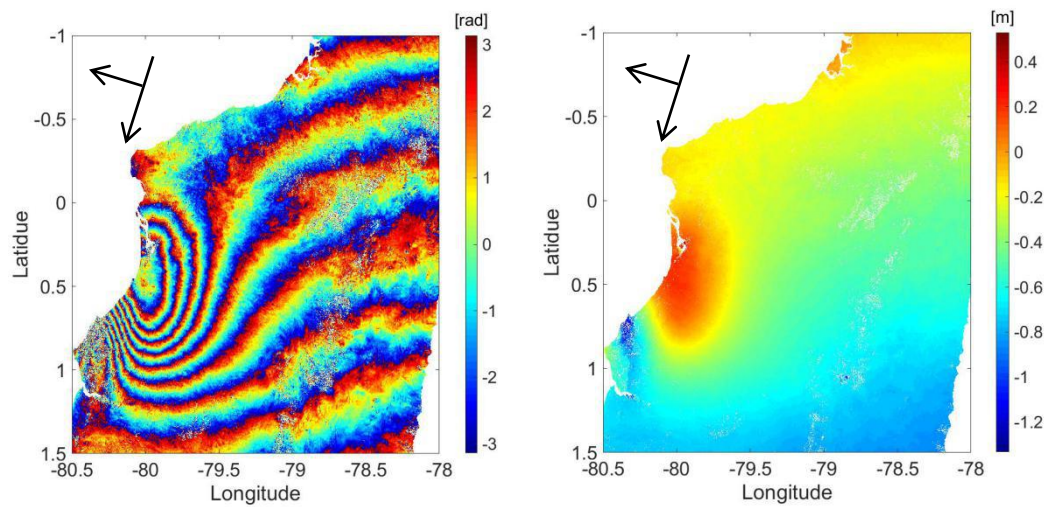


Figure 7.3: Interferogram from ALOS-2 data pair in Ecuador, Master: 01, April, 2016. Slave: 26, April, 2016. (a) Wrapped interferogram in radiant and (b) unwrapped interferogram in meter.

Fig. 7.3 shows the co-seismic pair interferogram, where we can see a strong deformation at western sea shore, which was the epicenter of the earthquake. Aside from this area, we can see a slope along azimuth direction from the north to the south that leads to a deformation with magnitude of around 1 meter. By removing it, we can highlight the earthquake deformation with a less disturbed result.

## 7.2 Residual Phase Removal Correction

Residual phase removal correction was applied on ALOS-2 pairs (seeing table 6.4) to remove the slope shaped residual phases that can be seen in the interferograms (see fig. 7.2 & fig. 7.3). Principle parameters setting of this process is shown in the following table:

Table 7.3: Principle parameters setting for residual phase removal

|                       |      |
|-----------------------|------|
| Azimuth window size   | 2048 |
| Range window size     | 2048 |
| Azimuth window number | 10   |
| Range window number   | 10   |

For each imterferogram, the poly degree were set to be 3, 5, 7, and 9.

### 7.2.1 Pre-seismic Interferogram

For pre-seismic pair, 23 points were selected as ground control points according to the rules discussed in section 5.1. Fig. 7.4 shows the distribution of ground control points:

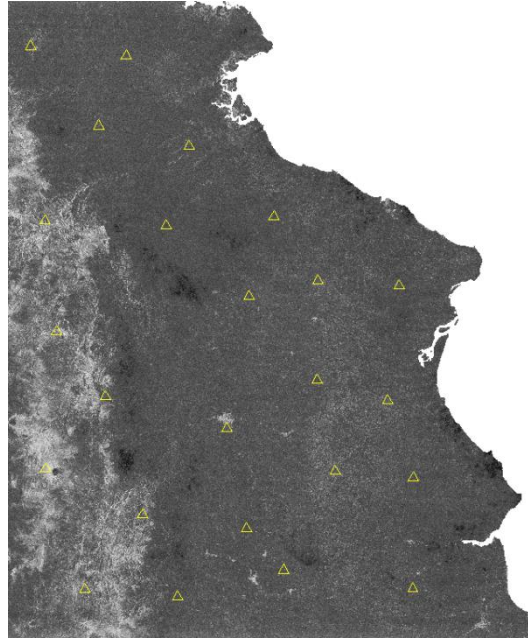
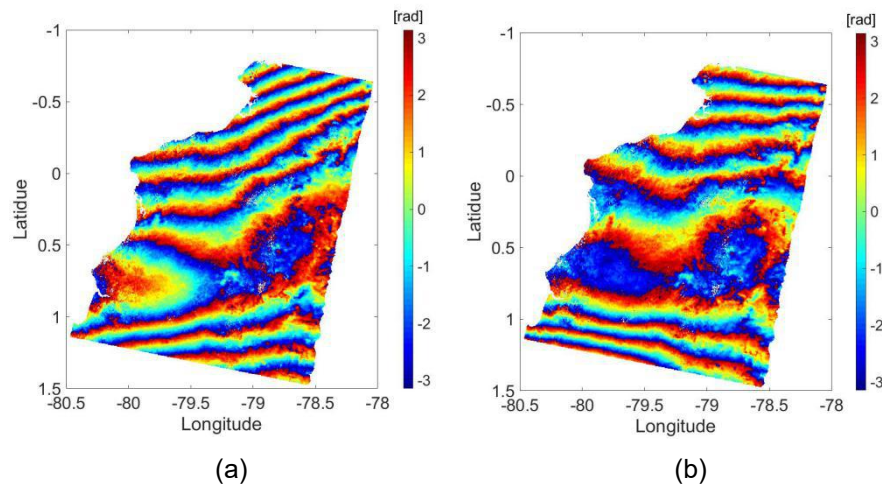


Figure 7.4: Ground Control Points distribution. The base map was the coherence map. All points are separated all over the map.

Residual phases were then removed from interferogram using different polynomial degrees (3, 5, 7, & 9), and corrected interferograms were shown in the fig. 7.5 and fig. 7.6:





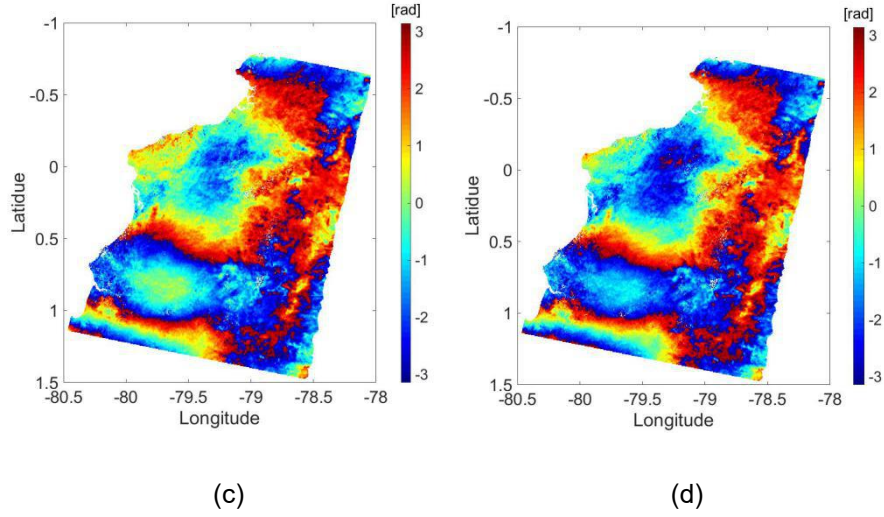


Figure 7.5: Wrapped interferogram of pre-seismic pair corrected by removing residual phase with different polynomial degrees:(a) correction with degree of 3; (b) correction with degree of 5; (c) correction with degree of 7; and (d) correction with degree of 9.

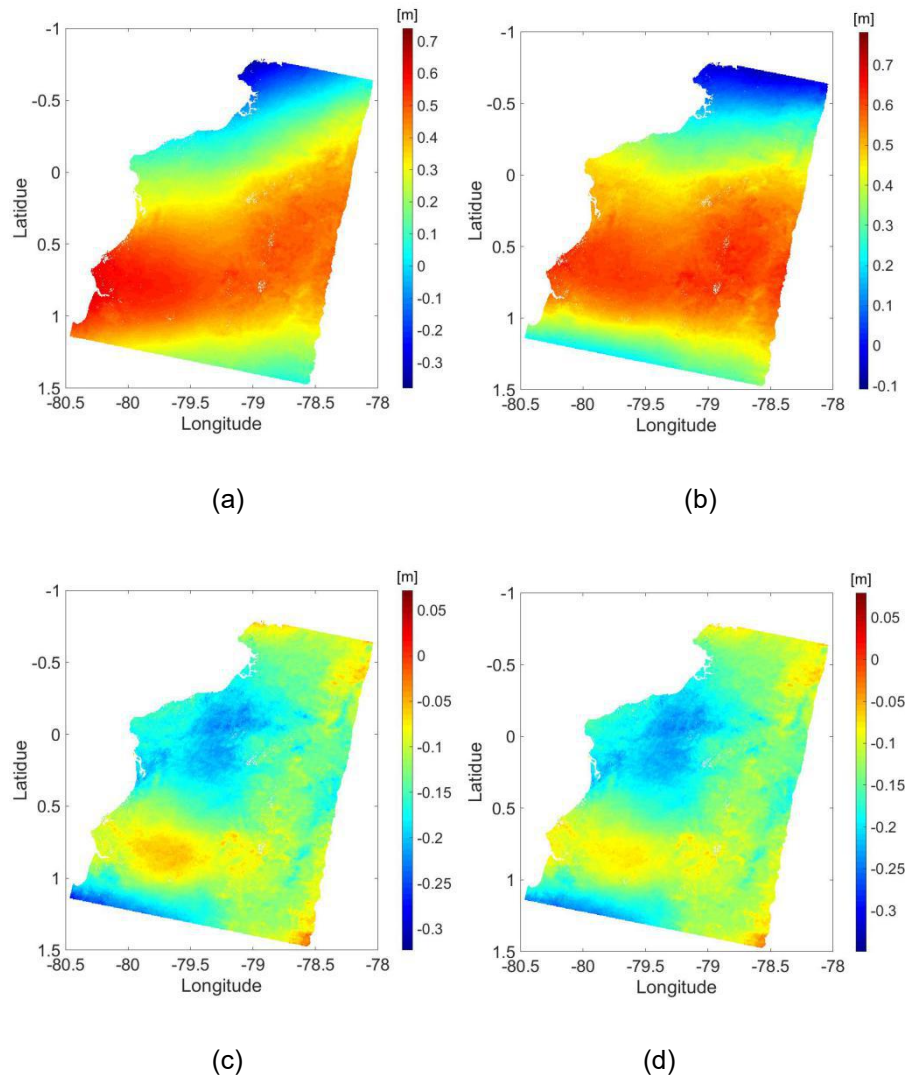


Figure 7.6: Unwrapped interferogram of pre-seismic pair corrected by removing residual phase with different polynomial degrees. The deformation information is shown in meter along the direction along line of sight: (a) correction with degree of 3; (b) correction with degree of 5; (c) correction with degree of 7; and (d) correction with degree of 9.

In this case, most of the residual fringes were deleted with polynomial degree of 7, when we increased the degree from 7 to 9, we can not see big changes of fringes from the wrapped interferogram. But if we see the comparison of unwrapped interferograms we can obtain a slightly larger “deformation” moving away from the satellite when the degree increased to 9 (shown in blue color) that might be caused by over fitting.

The mean value and the standard deviation (STD) of corrected interferogram with respect to different polynomial degree were then analyzed. Without obvious ground deformation in this pair, and if there was no other error sources, a mean value of “0” after applying the correction shall be obtained. And after the correction, the phase shall be flattened, hence the ideal STD shall also approach to “0”. As shown in fig. (7.7), the mean value decreases to “0” when the polynomial degree is increasing and stop changing after the degree reaches 7. In the fig. (7.8), we can see the same trend happened to STD. This shows that our method did removed most of the residual phases. We can see the STD value increases a little bit when the poly degree changes to 9, this can be the result caused by over fitting.

Table 7.4: Mean values and STD values of original InSAR result and corrected InSAR results of pre-seismic image pair

| Polynomial Degree | Without correction (0) | 3       | 5       | 7       | 9       |
|-------------------|------------------------|---------|---------|---------|---------|
| Mean [rad]        | 121.5620               | 17.4152 | 23.4484 | -7.1639 | -7.6973 |
| STD [rad]         | 53.3093                | 9.6834  | 8.4083  | 2.1446  | 2.2490  |

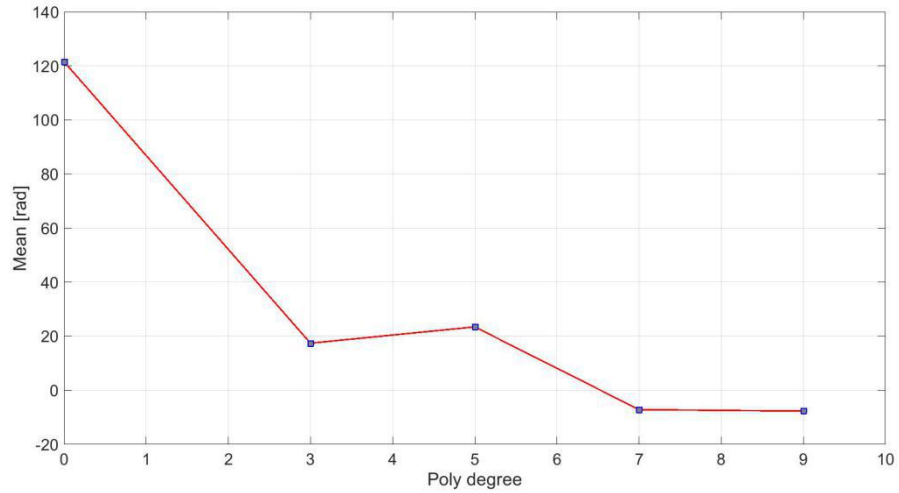


Figure 7.7: Mean value of unwrapped phase of corrected interfaograms (in radiant) with respect to different polynomial degree. Here we use degree of “0” to represent the original interferogram to demonstrate the change after applying residual phase removal correction.

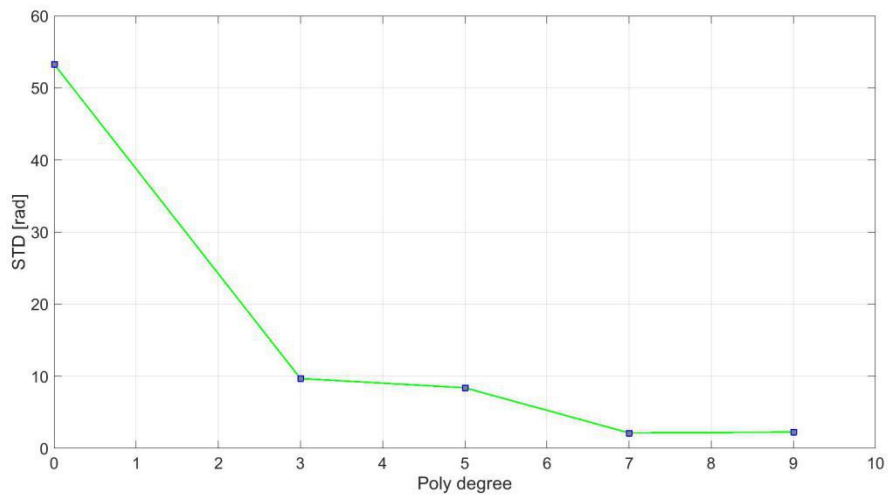


Figure 7.8: STD of unwrapped phase of corrected interferograms (in radiant) with respect to different polynomial degree. Here we again use degree of “0” to represent the original interferogram.

Although most of error phases were removed from the interferogram by this strategy, the mean value is not completely became “0” (-7.16 rad) with polynomial degree of 7. In fig.7.6 a descending area at northern part of the seashore can be seen, where it was the epicenter of the earthquake that happened later, and correspondingly, an uplift area at the southern sea shore. This “deformation” looks like tropospheric effect caused by turbulence. To confirm this assumption, another ScanSAR image from ALOS-2 of this area was

introduced. This image was acquired on 16, October, 2015. Two interferograms were generated from this image with respect to image acquired on 08, January, 2016 and image acquired on 01, April, 2016. Residual phase removal process were applied on two generated interferogram:

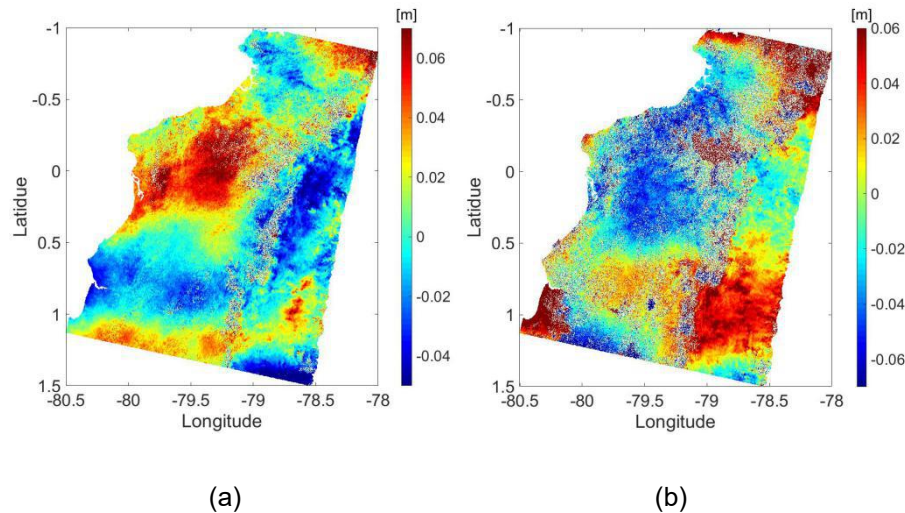


Figure 7.9: Residual phase removal results from testing pair. (a): Master: 16, October, 2015, slave: 08, January, 2016.,corrected with residual phase removal with degree of 7 (b) Master: 16, October, 2015 and slave: 01, April, 2016 with degree of 9.

In fig. (7.9) (a) the same pattern was obtained as it was in fig. (7.5) (c). Therefore it can be concluded that there was a turbulence on the date of 08, January, 2016, which caused the phase anomalies that can be seen after ionospheric phase correction.

In the eastern side of the corrected interferogram with polynomial degree of 7(shown in fig. 7.5), we also obtained uplift. By looking at the DEM, it can be known that belonging to a part of Andes mountain, this area has complicated topography and the average elevation is approximately 3000 meter. According to (Zebker, Rosen, & Hensley, 1997), Elevation will affect the troposphere, and creates tropospheric phase error in InSAR observation. According to this study, there is a approximate linear relationship between the tropospheric phase and elevation. Hence I assumed that the phase appeared in this area were caused by troposphere.

A rectangular area has been selected (shown in fig. 7.10) to verify the assumption, a

linear regression between the DEM and the corrected unwrapped interferogram with a polynomial degree of 7 was applied in this area.

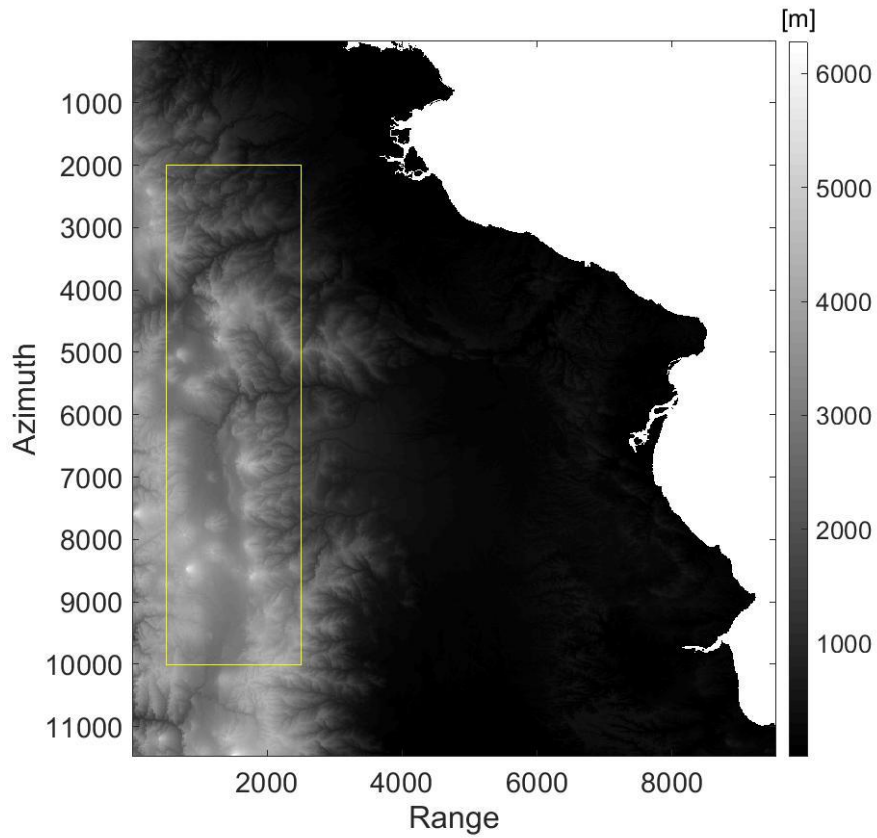


Figure 7.10: DEM of our study area, where yellow rectangle indicates the area we selected for linear regression.

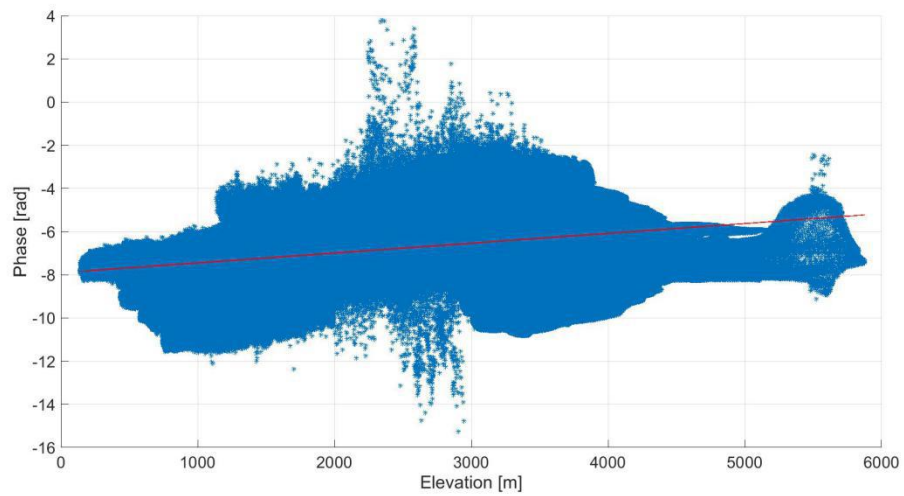


Figure 7.11: Phase with respect to elevation in the selected area.

With more than 15,000,000 sample pixels for linear regression, the linear relationship between the phase left in this area and the elevation can be roughly seen in the selected area. Hence it can be concluded that the phase left in this area is caused by troposphere.

Troposphere model can be introduced to correct this error, but since this thesis focus on ionospheric phase error correction, we didn't implement the tropospheric error correction.

### 7.2.2 Co-seismic Interferogram

In the co-seismic pair, 26 GCPs were generated. According to section 5.1, we didn't select points from the earthquake region.

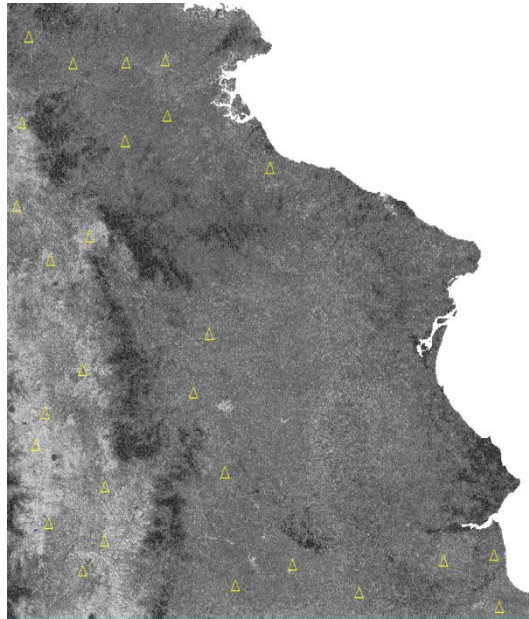


Figure 7.12: GCPs distribution, points were selected all over the area but not within earthquake area. The background map is the coherence map.

Similar to pre-seismic pair, residual phase removal with respect to polynomial degree of 3, 5, 7, and 9 were applied to this pair.



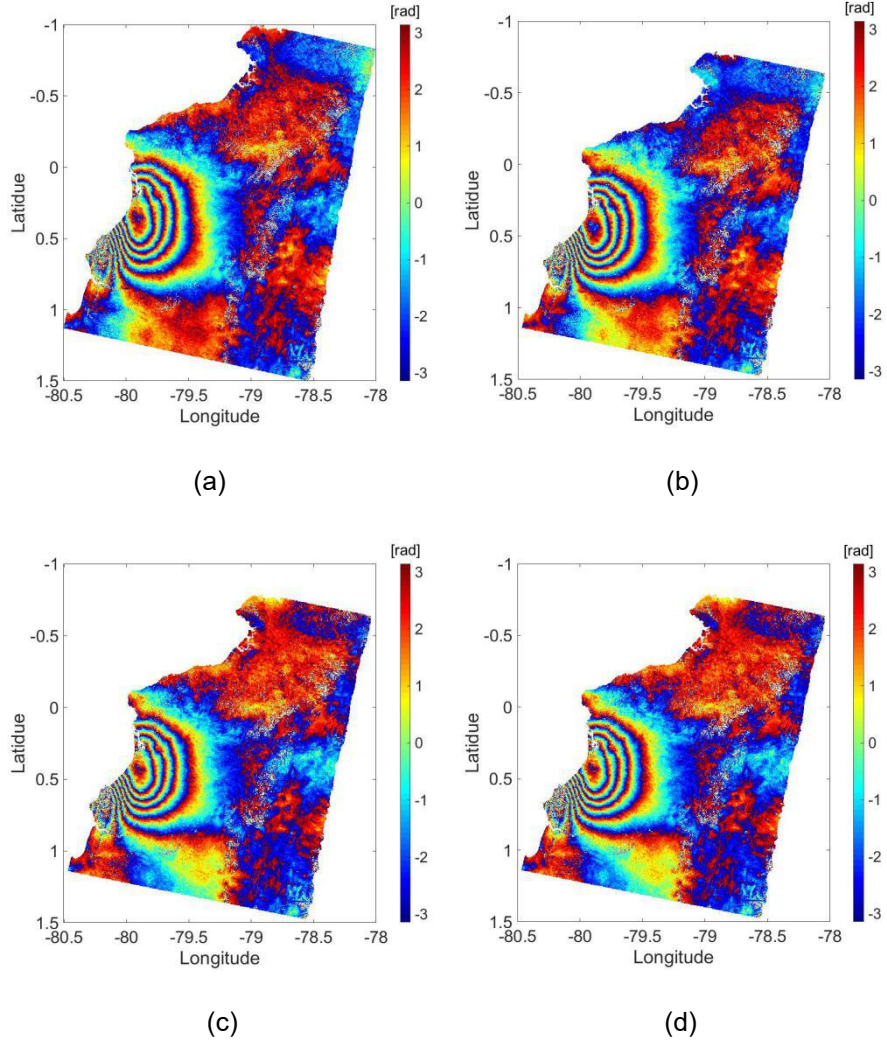
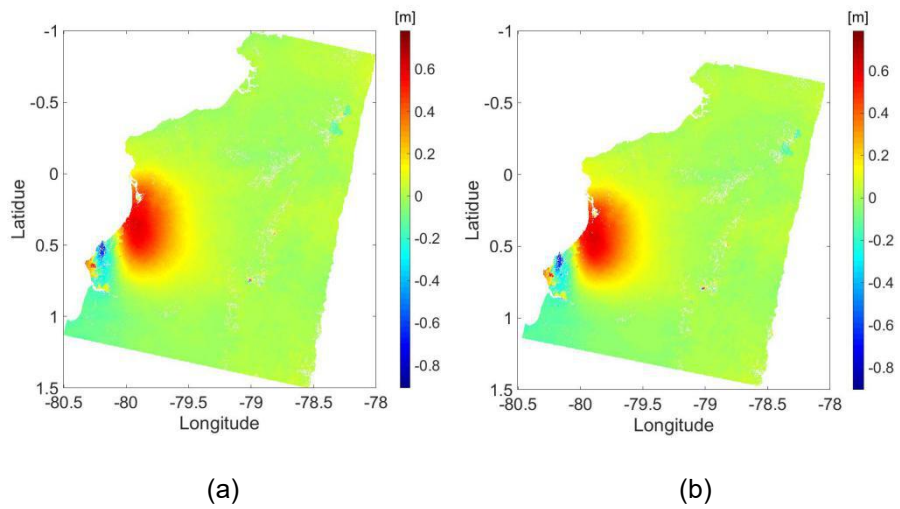


Figure 7.13: Wrapped interferogram of co-seismic pair corrected by removing residual phase with different polynomial degree:(a) correction with degree of 3; (b) correction with degree of 5; (c) correction with degree of 7; and (d) correction with degree of 9.



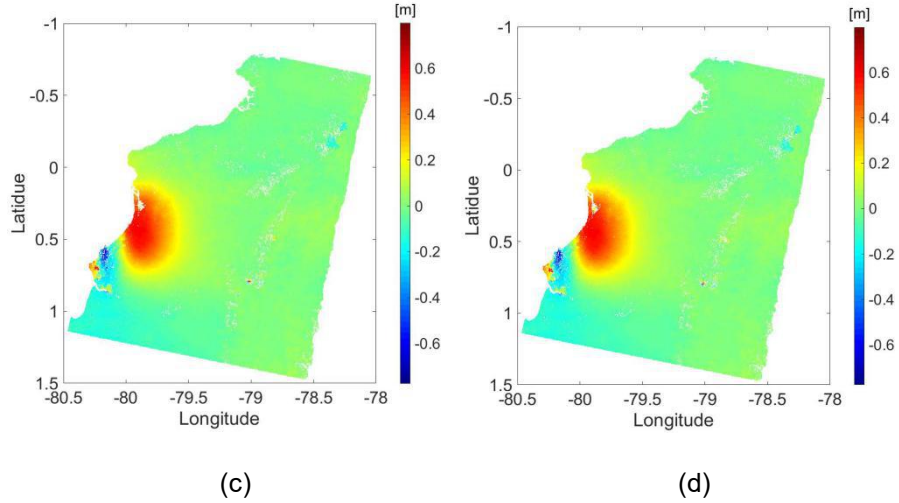


Figure 7.14: Unwrapped interferogram of co-seismic pair corrected by removing residual phase with different polynomial degree: (a) correction with degree of 3; (b) correction with degree of 5; (c) correction with degree of 7; and (d) correction with degree of 9.

Unlike the pre-seismic pair, most of the residual fringes can already been removed with using degree of 3. In the corrected unwrapped inferferogram, the slop trend caused by ionosphere is gone by polynomial degree of 3, and when the degree increases, the magnitude of deformation doesn't change a lot. After correction, the deformation of earthquake becomes more visible.

In order to implement statistic analysis, one area that doesn't cover the earthquake was selected in order to avoid analyzing crustal deformation phase. This selected area is shown in fig. 7.15.

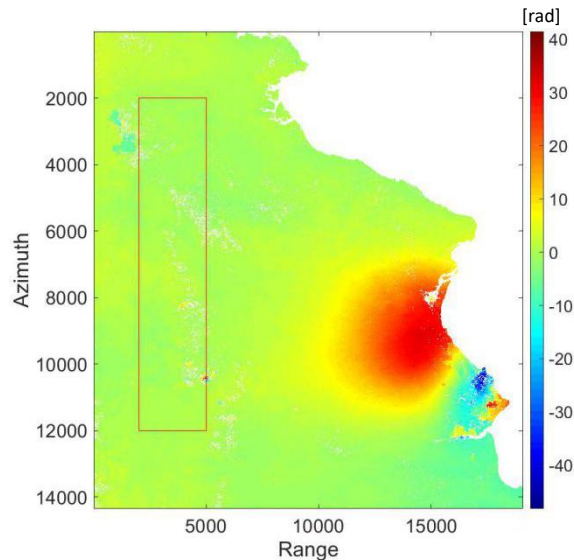




Figure 7.15: Area selected for statistical analysis (in red rectangle).

After selecting this area, mean and STD value with respect to different polynomial degree were again calculated.

Table 7.5: Mean values and STD values of original InSAR result and corrected InSAR results of co-seismic image pair

| Polynomial Degree | Without correction (0) | 3       | 5       | 7       | 9       |
|-------------------|------------------------|---------|---------|---------|---------|
| Mean [rad]        | -27.2519               | -0.2003 | -0.2908 | -0.0028 | -0.0021 |
| STD [rad]         | 9.1493                 | 1.1777  | 1.1728  | 1.3098  | 1.3088  |

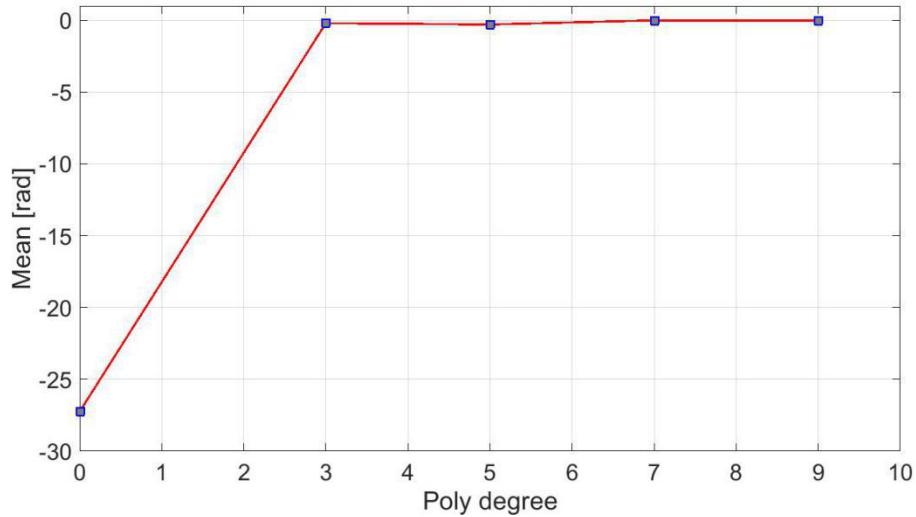


Figure 7.16: Mean value of unwrapped phase of selected area from corrected interferograms (in radiant) with respect to different polynomial degree. Here we use again degree of “0” to represent the original interferogram to demonstrate the change after applying residual phase removal correction.

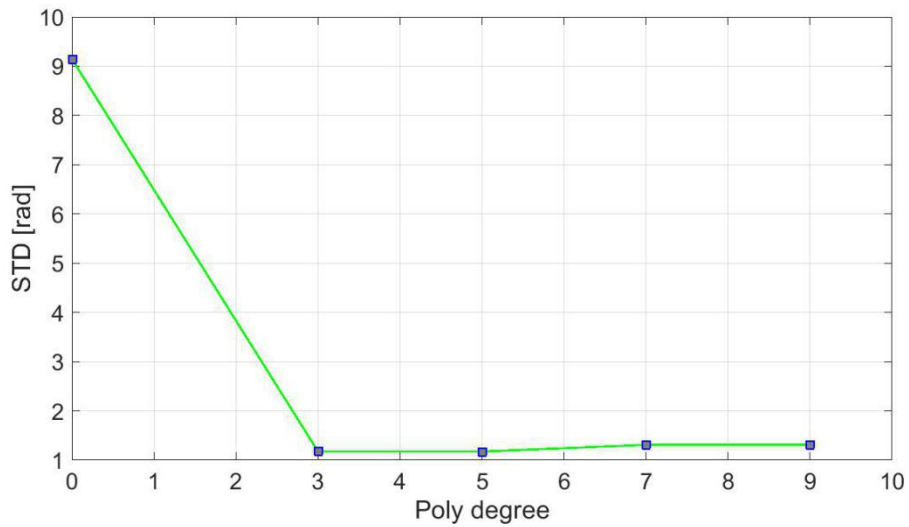


Figure 7.17: STD of unwrapped phase of corrected interferograms (in radiant) with respect to different polynomial degree. “0” is used to represent the original interferogram.

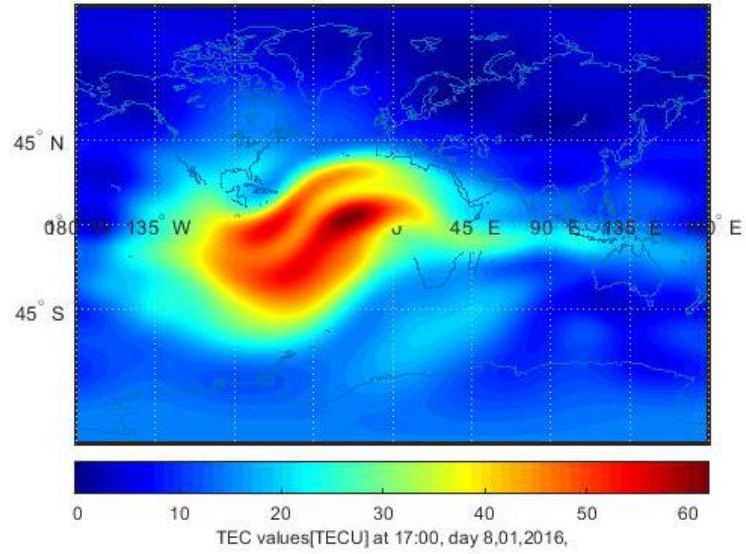
Unlike pre-seismic pair, the mean value approached to 0 when the polynomial degree is 3 and became stable afterwards. A slight increases was be obtained when polynomial degree increases after 3. This can again be the over-fitting effect brought by this method.

With mean value almost at 0 and no left tropospheric phase happened in the eastern part of the mountain, it can be concluded that this strategy worked well in this pair, ionospheric phase which appears as slope shaped residual phases were removed successfully.

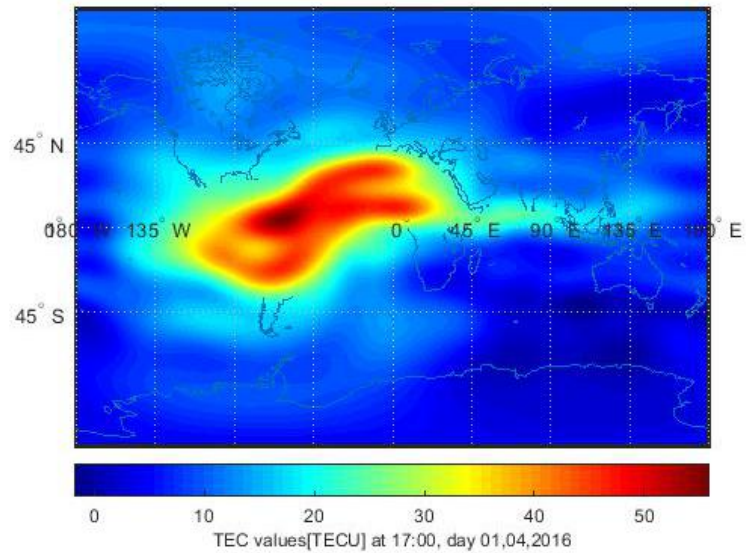
### 7.3 CODE based Ionospheric Phase Correction

A SH expansion were applied on hourly based CODE products to generate global covered vertical TEC map. This process was implemented using python version 3. The SH expansion was implemented using “pyshtools” (Wieczorek, & Meschede, 2018). After expansion, a further bilinear interpolation was applied for the VTEC map to re-sample it to the same size of the generated interferogram.

In this section, we implemented CODE based ionospheric phase correction on the pre-seismic pair in Ecuador (seeing table 6.4). CODE products at 17:00 UTC were used as a demonstration:



(a)



(b)

Figure 7.18: Global covered VTEC map (in TECU) generated by SH expansion, (a) VTEC map corresponds to the time 17:00 UTC, on 08, January, 2016 and (b) VTEC map corresponds to time 17:00 UTC, 01, April, 2016.

Fig. 7.18 shows a pair of result from SH expansion, where a clear concentration of free electron floating on South America can be seen at acquisition time because in that area, the local time is around 12:00 (in Ecuador with GMT-5). For this reason, such a huge ionospheric effect can be expected.

A VTEC variance map were generated after SH expansion by using the slave VTEC

map minus master VTEC map. From this map, we can see a huge TEC variance along equatorial area:

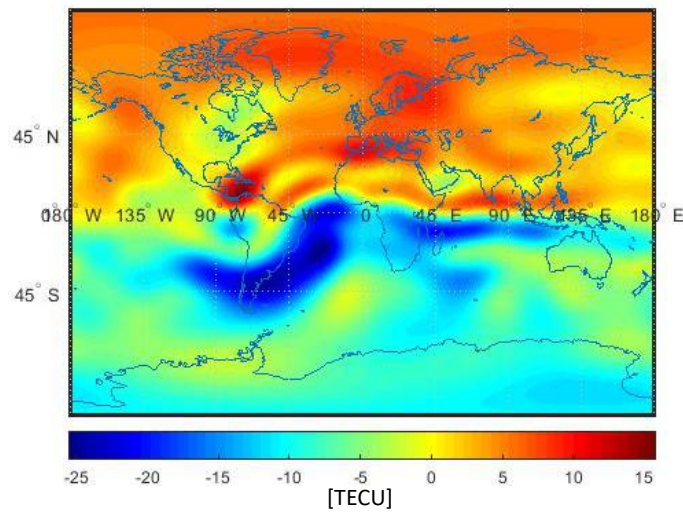
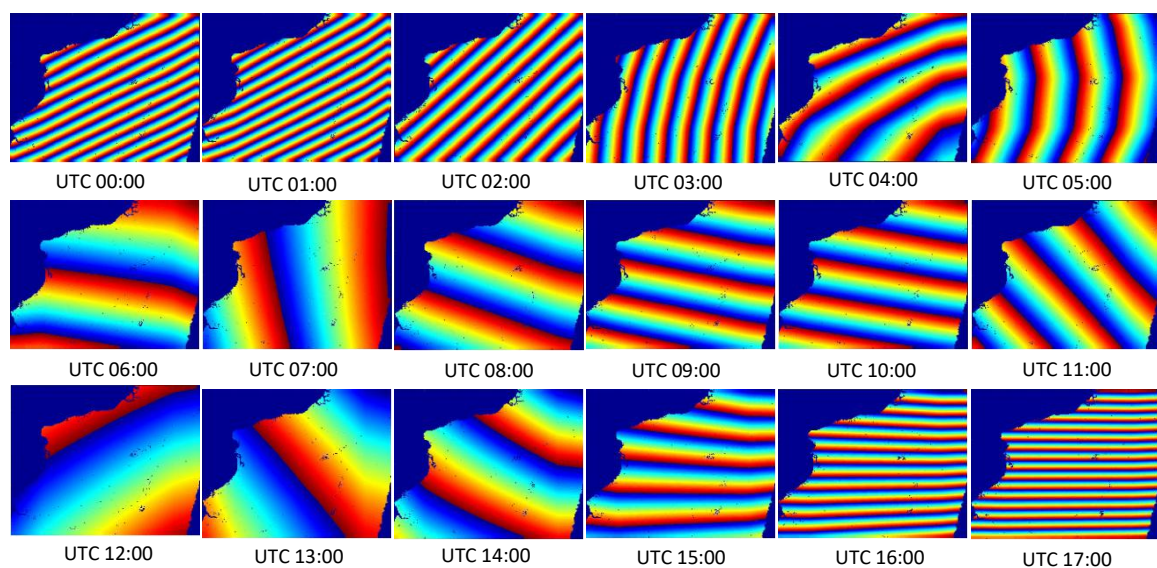


Figure 7.19: Global covered VTEC variance map of pre-seismic pair (in TECU) between 08, January, 2016 and 01, April, 2016.

After VTEC variance map is generated, study area is selected from it, it is then re-sampled, geo-coded and masked out with the interferogram. The slant TEC(STEC) value can be generated by re-projected VTEC map into slant of range direction using projection function which is a reciprocal of cosine function of the incident angle. In this thesis, the average of incident angle ( $39^\circ$ ) was use.

After STEC map was generated, the ionospheric phase in SAR observation can be calculated according to eq. 4.12.



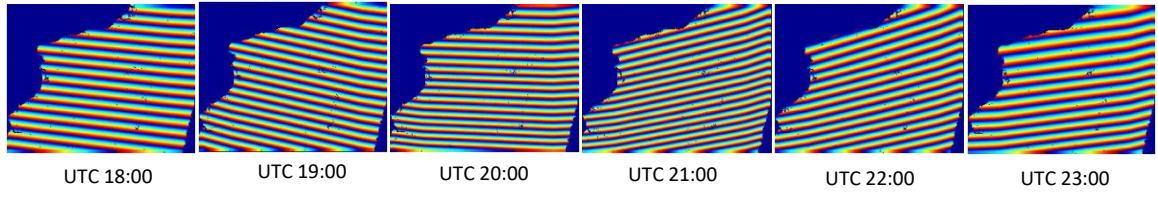


Figure 7.20: Wrapped generated ionospheric phase on different epochs.

Fig. 7.20 demonstrates the wrapped generated ionospheric phase at different time between 08, January, 2016 and 01, April, 2016. In generated ionospheric phase results, a slope shaped phases can be clearly seen. Note that this is an area of around  $350 \times 350$  km, where only this kind of large scaled trend shaped ionospheric error can be modeled by this approach.

Because the tested data were acquired at 17:00, the ionospheric phase that generated from this epoch were used for the following ionospheric correction.

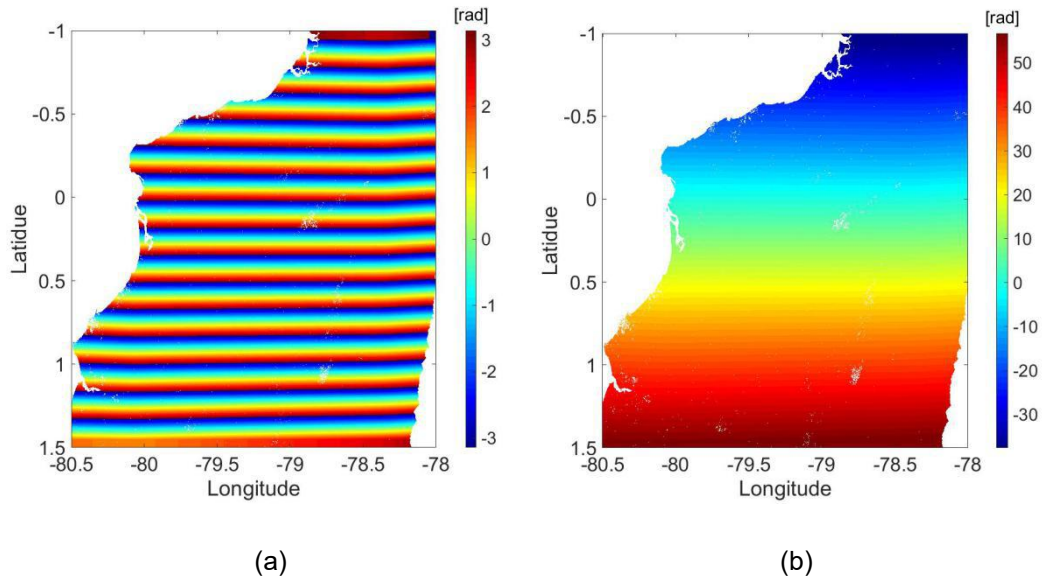


Figure 7.21: Ionospheric phase generated from CODE hourly product at 17:00 UTC with master date: 08, January, 2016 and slave date: 01, April, 2016. (a) Wrapped generated ionospheric phase, and (b) unwrapped ionospheric phase (in radian).

Both original unwrapped interferogram and the ionospheric phase were then re-referenced and the ionospheric phase were subtracted from the interferogram.



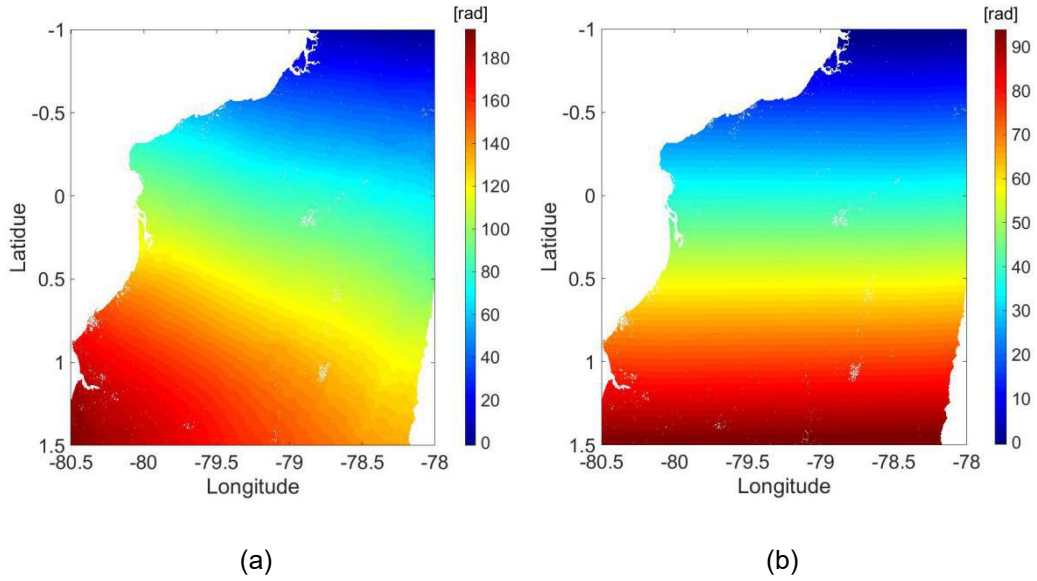


Figure 7.22: Unwrapped ionospheric phase (a) Re-referenced original unwrapped interferogram and (b) re-referenced unwrapped ionospheric phase.

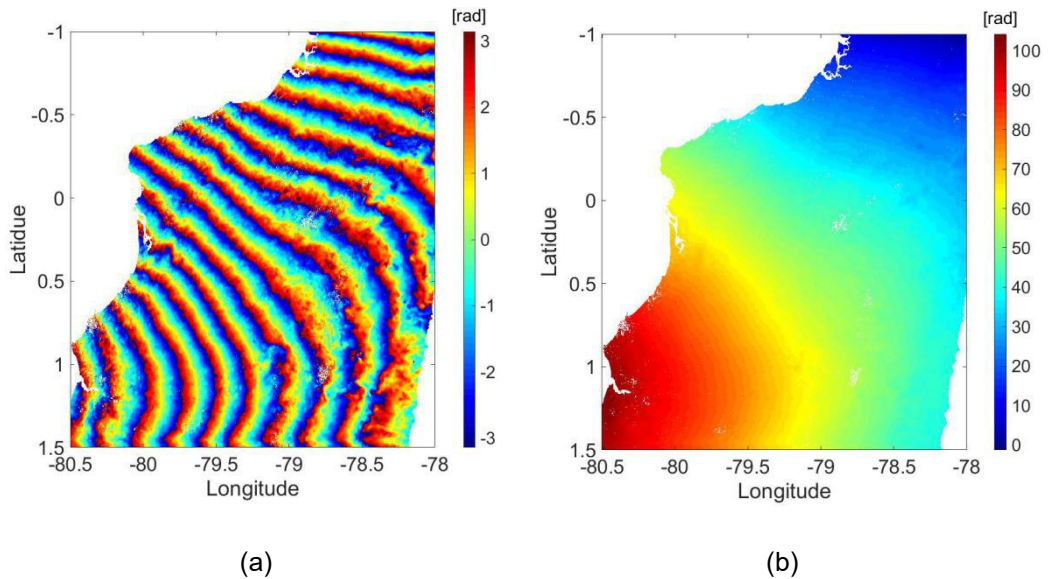


Figure 7.23: Corrected interferogram (a) Wrapped interferogram after ionospheric correction and (b) unwrapped interferogram after ionospheric correction (in radian).

Fig. 7.23 shows the result of the correction. Using CODE based ionospheric phase correction method, not all of the fringes from the interferogram can be removed, although by this method the slope shaped ionospheric phase stripe along the image was generated, and a phase group with magnitude of around 90 radian has been removed from the image, there are still around 100 radian phase left.

I therefore conclude that this method is not sufficient for ionospheric phase correction on our L-band InSAR observations. Further discussion will be presented in the following section.

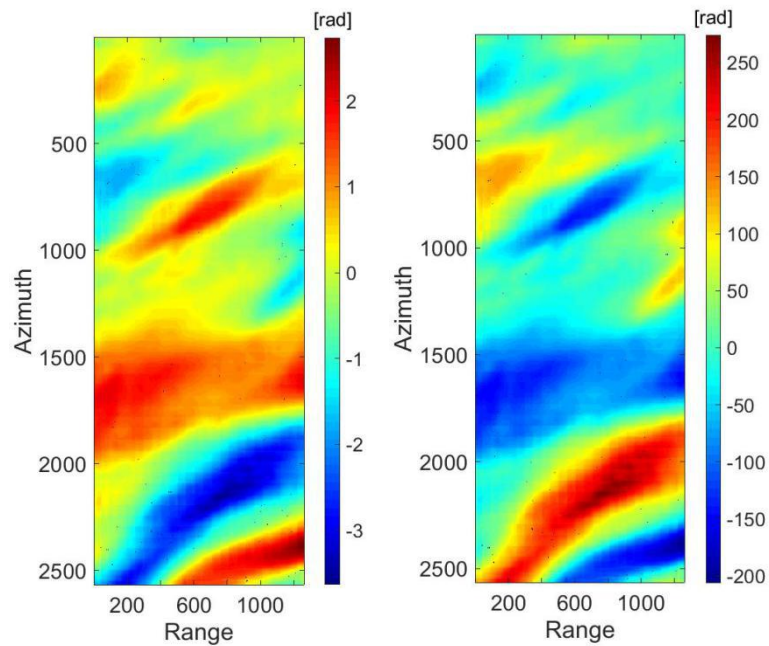
## 7.4 Azimuth based Ionospheric Phase Removal

Azimuth based method were implemented on ALOS-1 pair, and were tested on ALOS-2 pre-seismic pair (see table 6.1 and table 6.2).

### 7.4.1 MAI based Method

MAI interferogram generation was implemented by SARscape software(Exelis Visual Information Solutions, Boulder, Colorado). The MAI factor was set as “2” so that the full aperture will be split into 2 pieces: namely forward-looking and backward-looking aperture. Principle parameters of interferogram generation, filtering and unwrapping process were set the same as normal interferogram generation process (see Section 7.1).

For ALOS-1 image pair that locates in Alaska, the MAI phase were generated and re-scaled according to eq. (4.30). Results are shown in fig. 7.24:



(a)

(b)

Figure 7.24: Intermediate results of MAI based method on ALOS-1 PALSAR data (a) Generated MAI phase from ALOS-1 pair (in radian). This phase indicates the azimuth phase shift information per pixel; and (b) MAI phase scaled by aperture length, normal squint and wavelength according to eq. (4.30).

At the same time, the first derivative of InSAR phase with respect to azimuth direction were calculated from original InSAR phase:

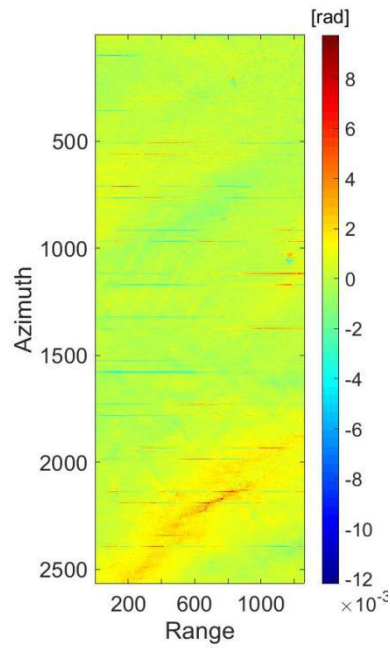


Figure 7.25: The first derivative of InSAR phase with respect to azimuth direction.

Fig. 7.25 shows the result, where the azimuth variance with irregular shaped patterns can be seen. After this is generated, a linear relationship between it and scaled MAI phase were estimated using polynomial fit. The estimated linear relationship is shown in fig. 7.26:



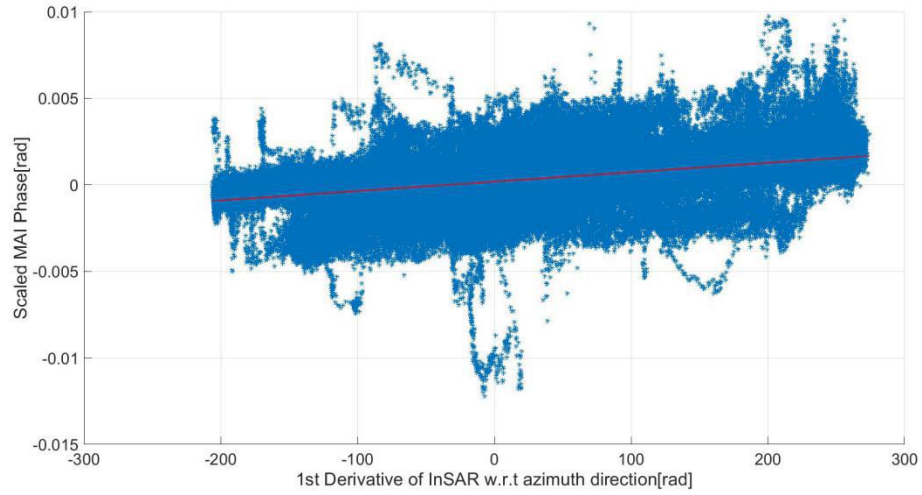


Figure 7.26: Linear relationship of scaled MAI phase with respect to the derivative of InSAR phase in azimuth direction.

In fig. 7.26, a clear linear relationship can be seen. The parameters of this linear function are:

Table 7.6: Estimated linear parameters (MAI based method)

|          |                         |
|----------|-------------------------|
| $\alpha$ | $5.4272 \times 10^{-6}$ |
| $\beta$  | $1.8551 \times 10^{-4}$ |

Ionospheric phase can then be calculated by integrating scaled MAI phase along azimuth direction according to eq. 4.31.

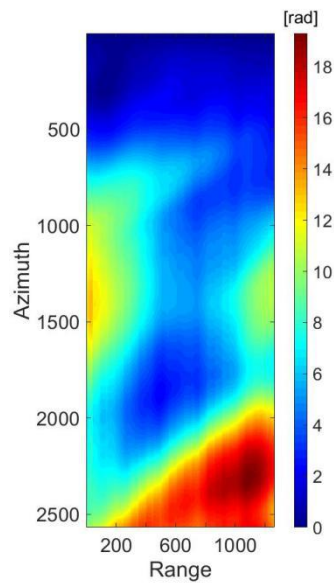


Figure 7.27: Calculated Ionospheric phase in radiant.

After the ionospheric phase was generated, it is re-referenced with the original unwrapped interferogram.

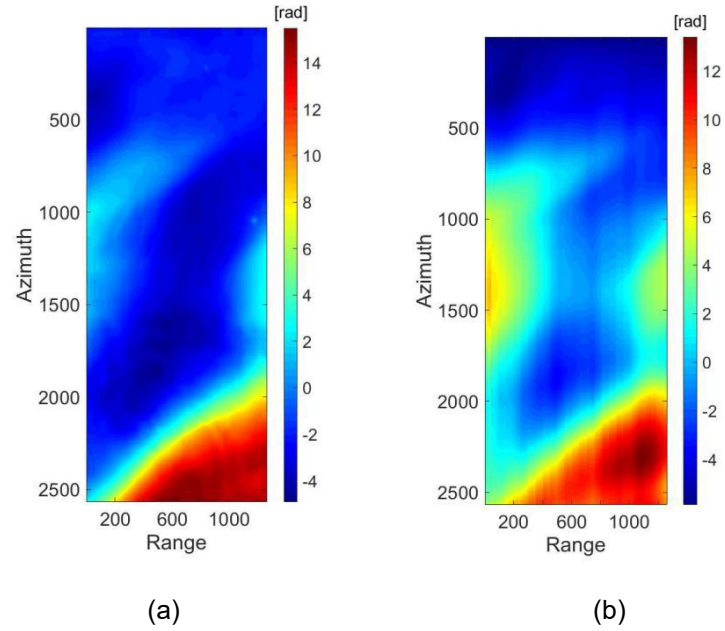


Figure 7.28:(a) Re-referenced unwrapped InSAR phase and (b) calculated ionospheric phase.

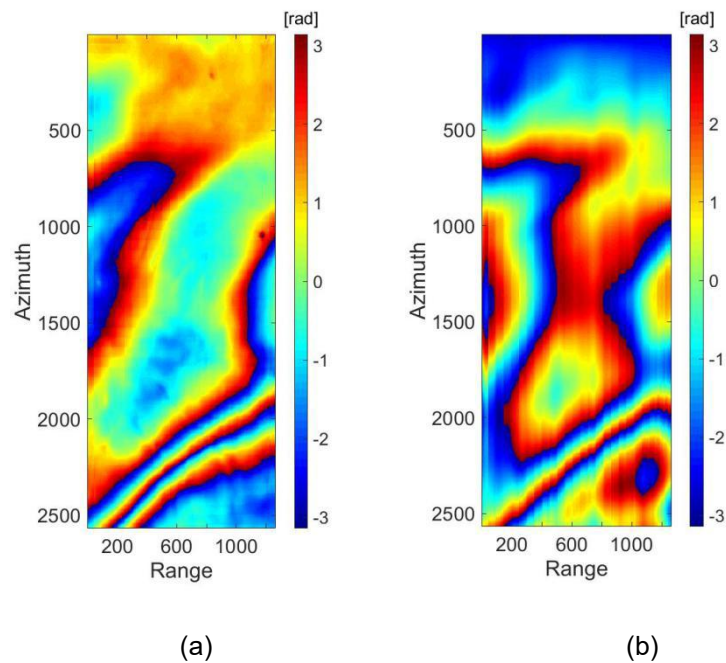


Figure 7.29:Wrapped ionospheric phase (a) Re-referenced wrapped InSAR phase and (b)wrapped calculated ionospheric phase.

It can be seen from fig. 7.29 that the calculated ionospheric phase has similar phase pattern as the re-sampled InSAR phase. By visualized analysis from the wrapped interferogram and wrapped ionospheric phase, a similar fringe structure between them can be obtained .

Ionospheric phase was then subtracted from the InSAR phase, the corrected InSAR phases are shown in fig. 7.30:

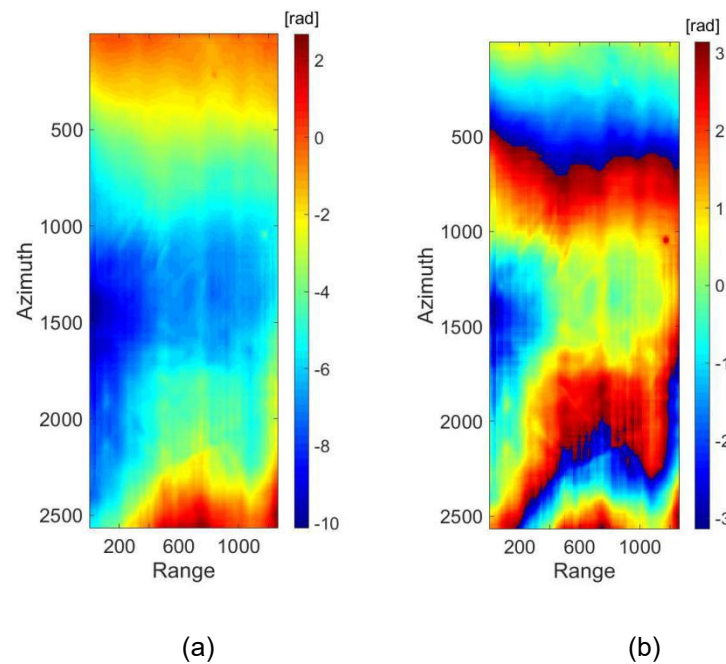


Figure 7.30: Unwrapped corrected interferogram (a) Unwrapped corrected InSAR phase based on MAI based ionospheric phase correction method, and (b) wrapped corrected InSAR phase.

This result shows two uplifts in the upper and lower part of the image, and a “deformation” moving away from the satellite with respect to the line of sight direction. These “deformations” are not expected after correction. They are assumed to be troposphere error. In order verify this assumption and to apply a statistic analysis, we selected one region out of this area for this area contains topography changes and also phase anomalies.

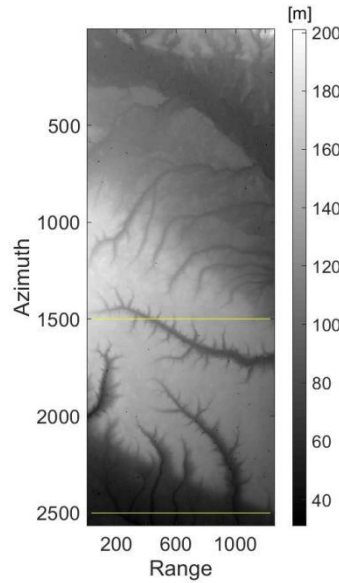


Figure 7.31: DEM and selected area for troposphere estimation (yellow rectangle).

The STD value and mean value were calculated:

Table 7.7:STD and mean value before and after ionospheric correction (MAI based method)

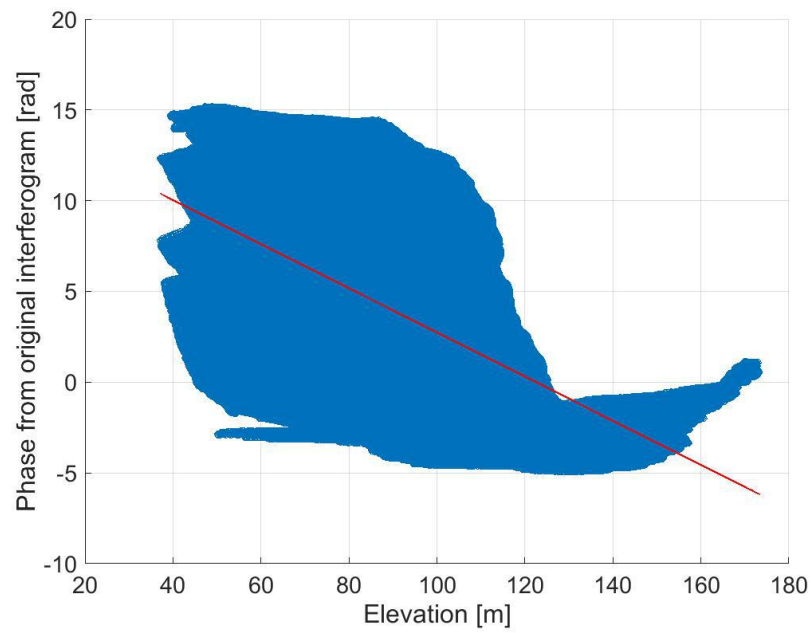
| Statistical value | Before correction | After correction |
|-------------------|-------------------|------------------|
| Mean [rad]        | 2.0534            | -0.9941          |
| STD [rad]         | 6.2860            | 2.1951           |

Because there was no reported strong surface deformation happened in that area, and no disturbances from other error source, assuming all fringes were caused by ionospheric error, a result which is smooth and without any deformation shall be expected and the calculated mean value and STD after correction should be “0”. However, from table 7.7, although the STD value and the mean value are reduced as expected, they are still not close to “0”. This means ether our ionospheric correction strategy is not sufficient, or we have some other error sources in our image.

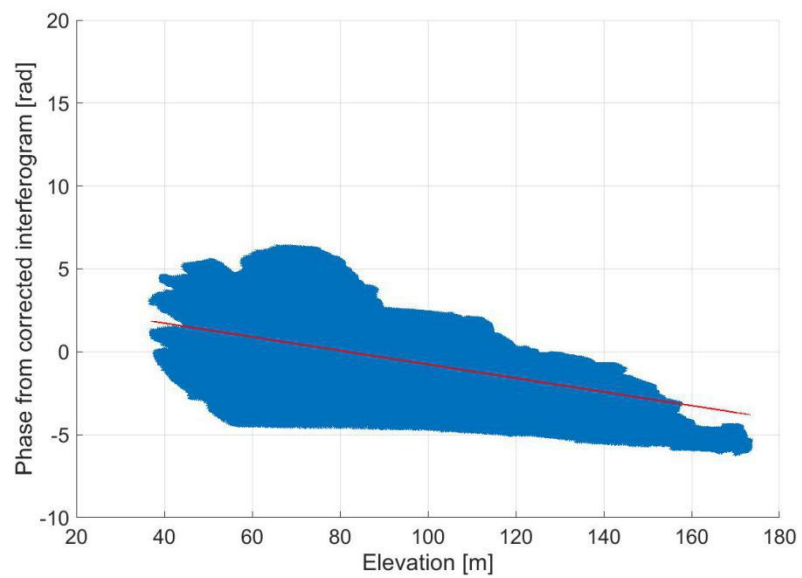
The relationship between the corrected InSAR phase and and DEM was estimated, by assuming the phase anomalies were caused by tropospheric error.

A linear regression was applied between the unwrapped corrected InSAR phase and DEM. The same approach has also been done between the uncorrected InSAR phase and and DEM to see the difference before and after ionospheric phase correction based on

MAI method:



(a)



(b)

Figure 7.32: Results of linear regression (a) Original InSAR phase with respect to elevation, and (b) InSAR phase after ionospheric phase correction, with respect to elevation.

Fig. 7.32 demonstrates phase change with respect to elevation due to the ionospheric phase correction. Before correction, no regular relationship can be seen between the

phase and elevation. After correction, a linear trend between phase and elevation was obtained. This result further proved that the phase anomalies after the ionospheric phase correction were caused by troposphere.

This trend was then subtracted from the selected area of the corrected InSAR. It is shown from the results that both STD and mean value were reduced after detrending:

Table 7.8:STD and mean value before and after subtracting tropospheric trend (MAI based method).

| Statistical value | Before subtracting the trend | After subtracting the trend |
|-------------------|------------------------------|-----------------------------|
| Mean [rad]        | -0.9941                      | $3.9182 \times 10^{-14}$    |
| STD [rad]         | 2.1951                       | 1.7395                      |

After subtracting the tropospheric trend, STD is reduced a little bit, and mean value was largely reduced to “0”, This result proves that the MAI based ionospheric phase correction method worked well in this pair.

The same approach was applied on ALOS-2 pre-seismic pair. Because ALOS-2 ScanSAR data has a huge coverage, one sub-swath was selected out to be tested in order to reduce the data volume.

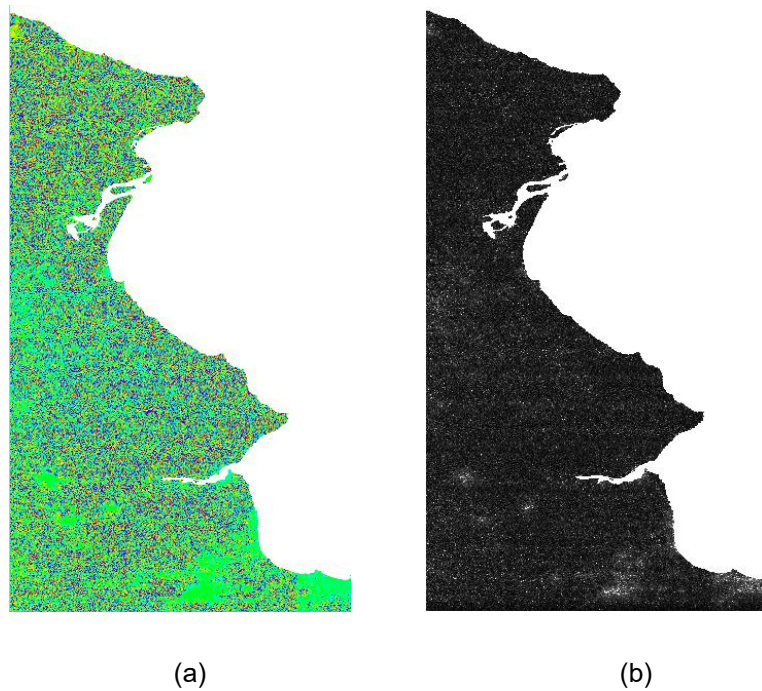


Figure 7.33: MAI results from ALOS-2 ScanSAR data from pre-seismic pair. (a) Generated MAI

phase, and (b) Coherence map of this pair, with values from 0-1 and the darker it is the more it close to 0.

Fig. 7.33 shows the result from ALOS-2 pre-seismic pair. It can be seen that the generated MAI phase from this pair is too noisy, and if we look at the coherence map, it appears to be totally decorrelated.

It seems like this approach couldn't be applied on this data. The reason of it will be discussed in the following section.

## 7.4.2 AT based Method

Like MAI based method, AT based also generates azimuth shift information of the testing pair. SARscape software(Exelis Visual Information Solutions, Boulder, Colorado) provides the AT process with generating shifts both along range and azimuth direction. in this process, the cross-correlation windows size was set to be 64×64 and only amplitude information were considered.

Like MAI phase, AT phase was also scaled by aperture length, normal squint and wavelength.

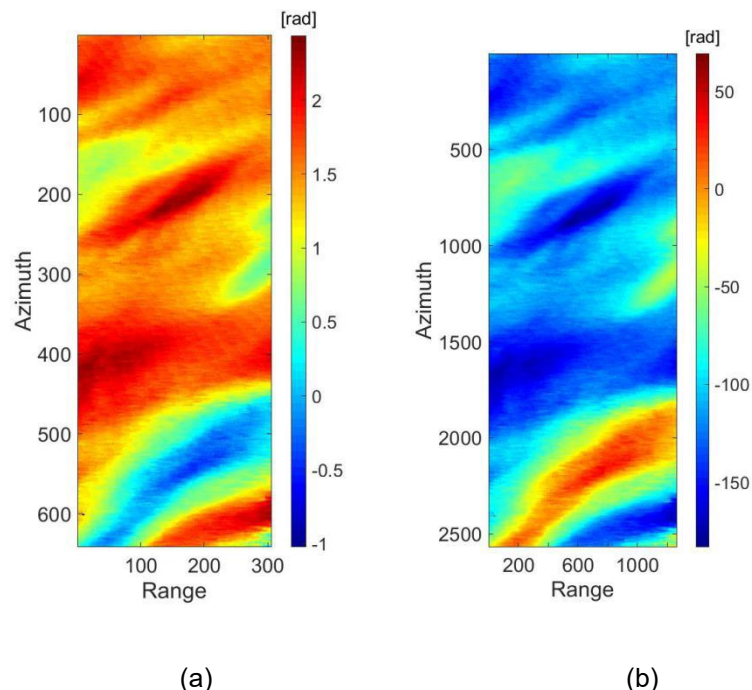




Figure 7.34: Intermediate results of AT based method on ALOS-1 PALSAR data (a) Generated AT azimuth phase from ALOS-1 pair (in radian) and (b) AT azimuth phase scaled by aperture length, normal squint and wavelength according to eq. (4.30).

The first derivative of InSAR phase with respect to azimuth direction was also generated from original InSAR phase and the linear relationship between it and scaled AT azimuth phase were estimated by poly fitting:

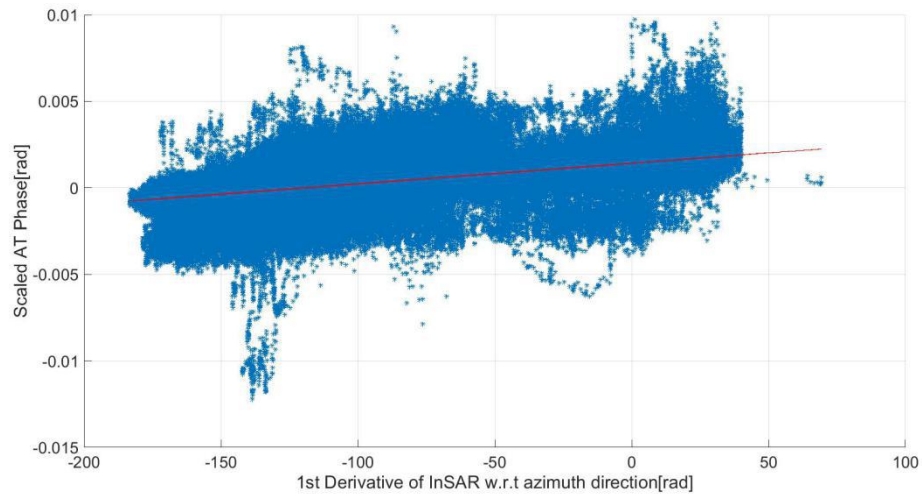


Figure 7.35: Linear relationship between scaled AT azimuth phase and the derivative of InSAR phase in azimuth direction.

Table 7.9: Estimated linear parameters (AT based method)

|          |                         |
|----------|-------------------------|
| $\alpha$ | $1.1917 \times 10^{-5}$ |
| $\beta$  | 0.0014                  |

Ionospheric phase can again be calculated by integrating scaled AT azimuth phase along azimuth direction according to eq. (4.31).



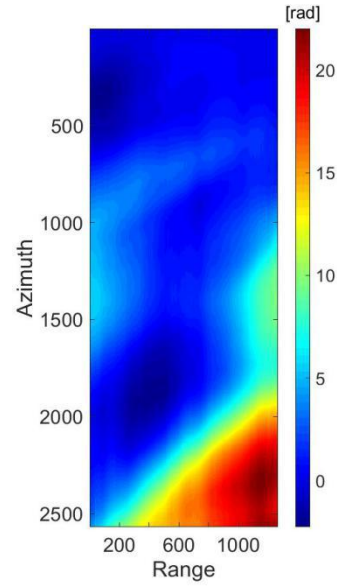


Figure 7.36: Calculated unwrapped ionospheric phase based on AT based method in radiant.

To subtract the ionospheric phase from the original InSAR phase, they were re-referenced:

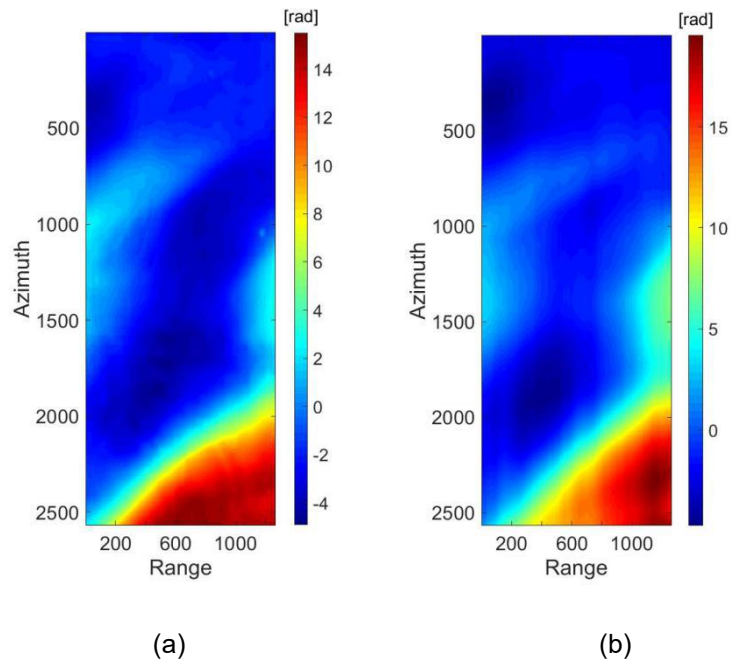


Figure 7.37: Calculated ionospheric phase using AT based method ALOS-1 data(a) re-referenced unwrapped original InSAR phase and (b) re-referenced unwrapped ionospheric phase.

By visualized comparison between InSAR phase and ionospheric phase, it is not hard to see that a similar pattern in both figures and the magnitude of the phase is almost the

same. Further, ionospheric phase was subtracted from unwrapped InSAR phase:

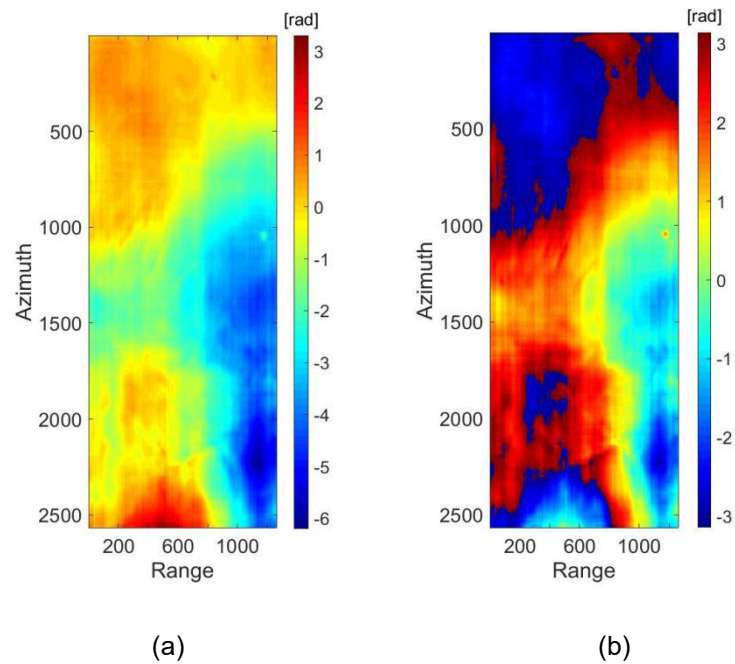


Figure 7.38: Ionospheric phase correction results based on AT based method.(a) Unwrapped corrected InSAR phase and (b) wrapped corrected InSAR phase.

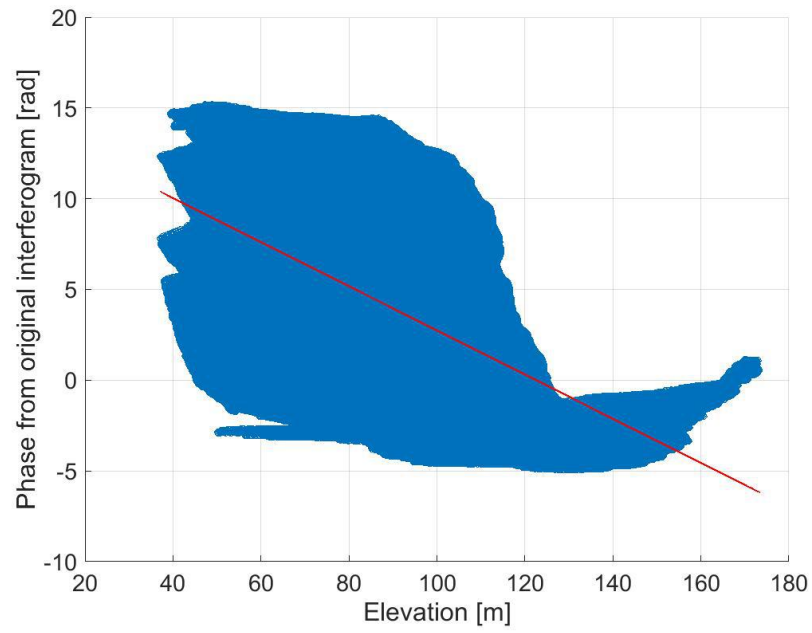
Statistical analysis was then implemented with the same selected area shown in fig. 7.31.

A comparison of the parameters before and after corrections is shown in table 7.10:

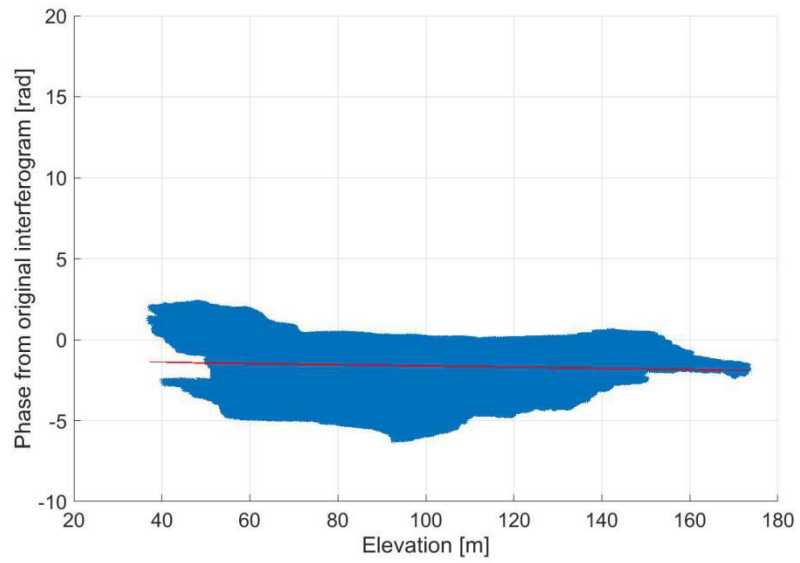
Table 7.10:STD and mean value before and after ionospheric correction (AT based method)

| Statistical value | Before correction | After correction |
|-------------------|-------------------|------------------|
| Mean [rad]        | 2.0534            | -1.6444          |
| STD [rad]         | 6.2860            | 1.7714           |

Again after ionospheric phase correction, there are some phase anomalies remained. This means some other error sources still exist in the corrected interferogram. By applying again linear regression, a linear relationship was discovered after ionospheric phase correction.



(a)



(b)

Figure 7.39: Results of linear regression, (a) original InSAR phase with respect to elevation, and (b) corrected InSAR phase with respect to elevation.

Fig. 7.39 shows that after ionospheric phase correction, there is a clear linear relationship between the phase and elevation. This proves again the ionospheric correction worked well by removing ionospheric phases but only tropospheric phases

remained. Then, after subtract this linear trend from the corrected phase, the STD and mean value of phase were estimated from the selected area:

Table 7.11:STD and mean value before and after subtracting tropospheric trend (AT based method)

| Statistical value | Before correction | After correction         |
|-------------------|-------------------|--------------------------|
| Mean [rad]        | -1.6444           | $8.3866 \times 10^{-15}$ |
| STD [rad]         | 1.7714            | 1.7677                   |

After subtracting tropospheric trend, although the STD didn't changed a lot, the mean value was largely reduced ( $\sim 1.6444$  rad) and approached to "0".

Results shows that AT based ionospheric phase correction had a good performance on our ALOS data pair.

The same process was applied on ALOS-2 ScanSAR pair. Here because the data volume is too big for processing, only a part of ScanSAR data was used for testing:

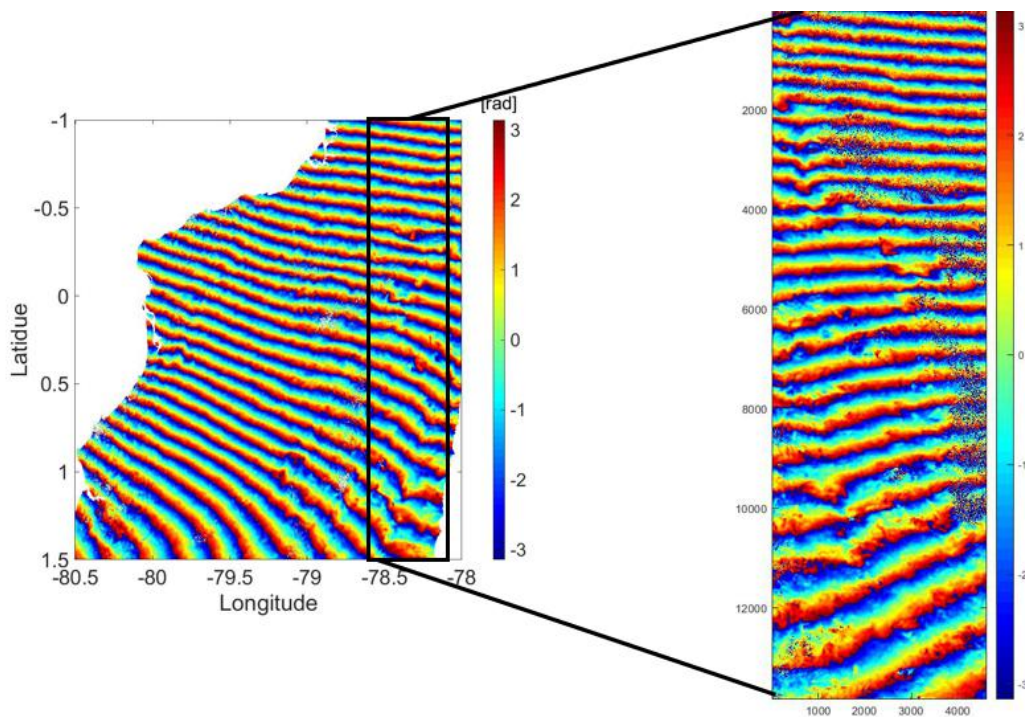


Figure 7.40: Selected area for AT based ionospheric phase correction from ALOS-2 ScanSAR pre-seismic pair.

Because only amplitude observation was used, this time the coherence was not lost like in MAI based method. In this pair, strong azimuth shift were not found, and the

corresponding azimuth derivative variance is also low:

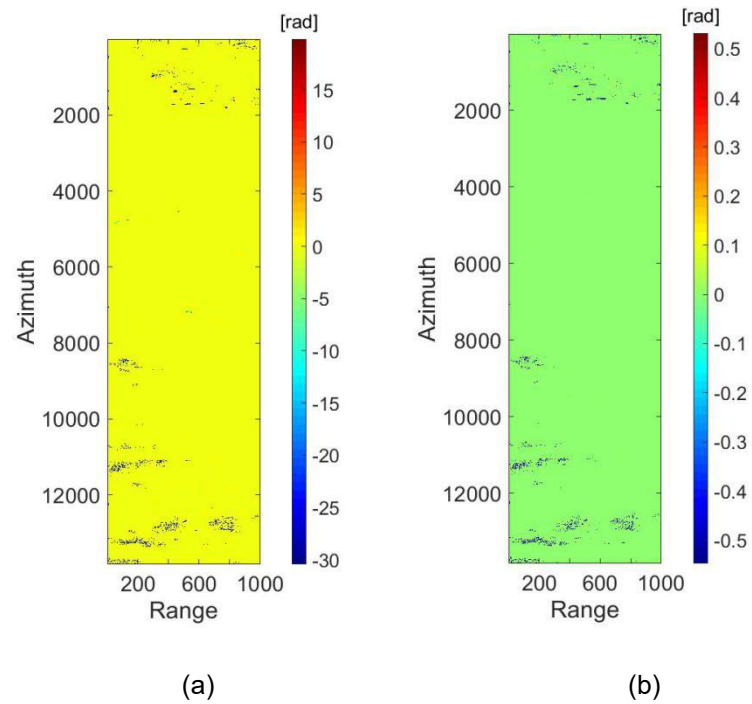
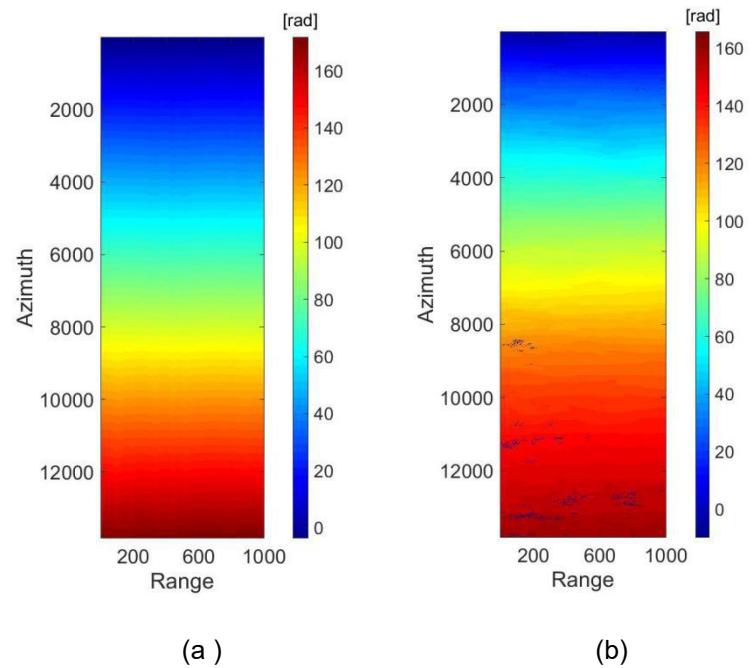


Figure 7.41: Intermediate results of AT based method on ALOS-2 data: (a) AT azimuth shift phase and (b) Azimuth derivative with respect to azimuth direction.

The ionospheric phase were then calculated and re-referenced with the original InSAR phase:



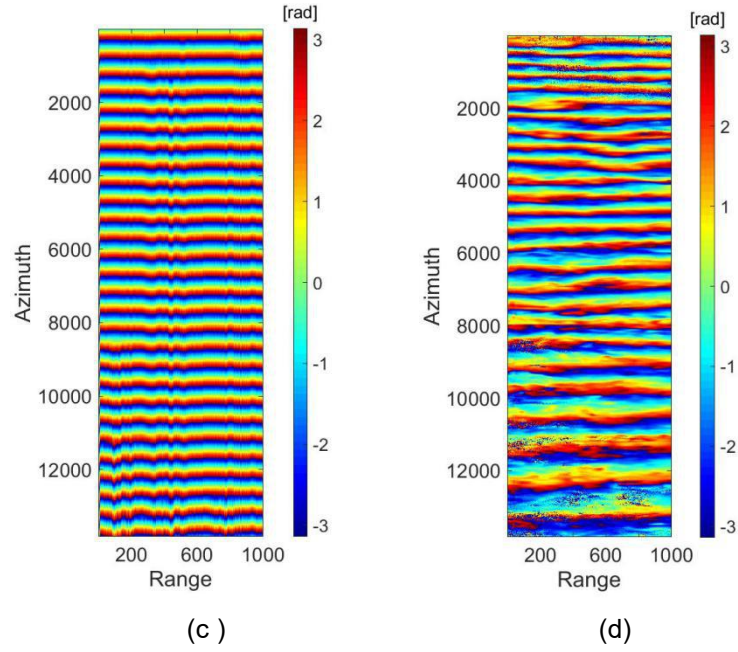


Figure 7.42: Comparison of calculated ionospheric phase and original InSAR phase. (a) Calculated ionospheric phase based on AT based method, and (b) original unwrapped InSAR phase. (c) Wrapped calculated ionospheric phase, and (d) wrapped original InSAR phase.

With no strong variance along azimuth direction, the ionospheric phase was generated with a flatted trend, and it has a shape similar to the original interferogram. It was then subtracted from the original interferogram to implement the ionospheric phase correction:

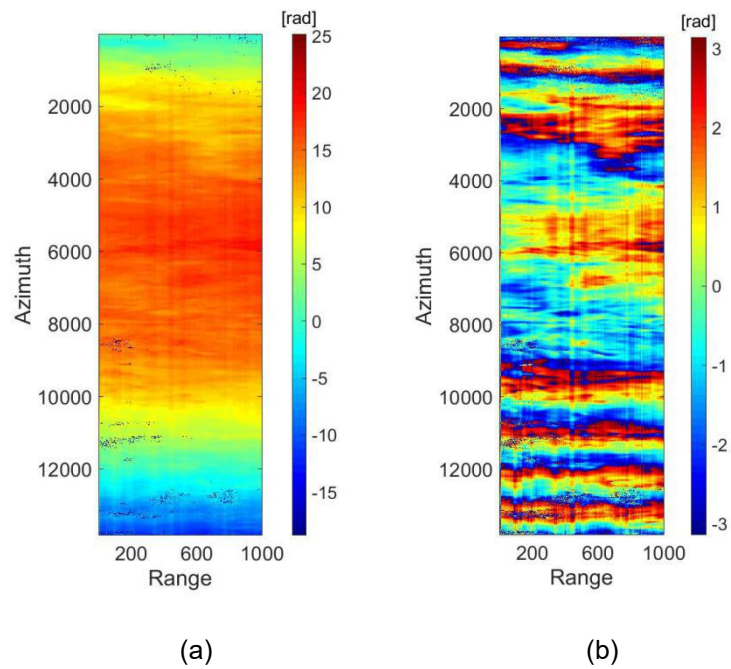


Figure 7.43: Corrected InSAR phase of ALOS-2 data, (a) unwrapped corrected InSAR phase, (b) wrapped corrected InSAR phase.



and (b) wrapped corrected InSAR phase.

Fig. 7.43 shows the corrected InSAR phase. A relative big phase anomaly can still be seen in the center of the corrected interferogram. This part can be troposphere error because as mentioned in section 7.2, this part covers a mountainous area , and also, azimuth based method didn't consider the bias of frequency from the center carrier frequency, when there is quadratic phase error existing, it can not be removed totally.

## **7.5 Discussion**

### **7.5.1 Residual Phase Removal Correction**

In the experiments part results from residual phase removal method were first introduced. The results showed a good ability of this method of removing ionospheric phase in ALOS-2 ScanSAR data. From these two pair however, the optimal degrees are not the same. For pre-seismic pair, I got a good result when I increased the polynomial degree to 7, and for co-seismic pair, the corresponding optimal degree is 3. This difference is because the shape of different ionospheric phase fringes. Like in the pre-seismic pair, due to the quadratic error from the bias of the carrier center frequency, there was a trend towards to the range direction. This kind of small detailed changes of shape of ionospheric phase increases the difficulty of modeling them using polynomial surface. Different pairs have different ionospheric phase shapes and in order to model them, different polynomial degrees should be tested separately. This is the a disadvantage of this method.

Another disadvantage of this method is, only the modeled ionospheric phase can be generated. But the true ionospheric phase as long as the true STEC values can not be generated. Further more, this method is only sufficient when the ionospheric phase shape appears like a slope shape, this usually happens in large scaled area. Too detailed and complicated ionospheric phase shape can not be modeled. For example, for the ALOS PALSAR data that were used in this thesis, the ionospheric phase patterns were difficult to be modeled.

## 7.5.2 CODE based Ionospheric Phase Correction

CODE based method appears to be not sufficient for the task. Result of ALOS-2 pair shows a poor ability of ionospheric phase correction. After every step through the process were checked, it can be assumed that this bias between CODE generated ionospheric phases and ionospheric phases we need for InSAR. This bias is because the variance of TEC existing between GPS satellites and SAR satellites.

GPS satellites flies at orbit of altitude of around 20000km, while ALOS-2 satellite flies at orbit of altitude of around 600 km. And since ionosphere exists from 60 km to 1000km, we shall expect a bias of TEC from 600 km to 1000km from GPS's observations.

Although CODE products are not sufficient to be used to apply ionospheric phase correction in InSAR application, it can still provide the information of activities of ionosphere and TEC variance, as a standard to show if the testing area suffered from ionospheric error when acquired by satellites.

## 7.5.3 Azimuth shift based Ionospheric Phase Correction

Both MAI based and Azimuth based method had a good performances on ALOS PALSAR data pair. After ionospheric correction and subtraction of tropospheric trend, the STD and mean value of them are shown in table 7.12:

Table 7.12: Statistical result of two azimuth based methods for ionospheric phase correction

| Statistical value | MAI based method         | AT based method          |
|-------------------|--------------------------|--------------------------|
| Mean [rad]        | $3.9182 \times 10^{-14}$ | $8.3866 \times 10^{-15}$ |
| STD [rad]         | 1.7395                   | 1.7677                   |

Two methods has more or less the same performances.

For the tested ALOS-2 ScanSAR data, MAI based method was not sufficient. The generated MAI phase lost coherence totally. I assume there are two reasons for this: First, when the aperture was split, the azimuth resolution is lost and signal-to-noise ratio (SNR) is decreasing at the same time. If the original pair's coherence is not high, the MAI phase



shall be even worse. Second reason can be, that ScanSAR SLC data are focused with “full-aperture” approach, and the instantaneous doppler spectrum is varying along azimuth direction, JAXA by-passes this by zero-padding the missing acquisitions. This result in again a coherence lose along azimuth direction.

As for AT based method, same ALOS-2 ScanSAR data was tested. The result was not perfect, because this method doesn’t consider the bias from the margin to the center carrier phase, which can cause quadratic ionospheric error. But still, with this method, most part of the ionospheric phase ( $\sim 160$  rad) can be removed from the original interferogram.

## 8 Conclusion and Outlook

### 8.1 Conclusion

In this thesis, 4 methods were implemented for ionospheric phase correction with different L-band SAR observations. To test the method, ALOS PALSAR data and ALOS-2 ScanSAR data were used as testing data.

Residual phased removal method were first applied for ALOS-2 ScanSAR data. A pre-seismic pair and a co-seismic pair images of an earthquake were tested using this method. Results show a good ability of eliminating ionospheric phase from this method. To implement this method, an optimal polynomial degree has to be found. This method is especially good for a slope shaped ionospheric phase.

CODE hourly based products were used to calculate ionospheric phases. In this experiment, ALOS-2 ScanSAR data were used. For ionospheric phase correction from InSAR, the right epoch of SAR data acquisition shall be used. However, results indicate that this method is not sufficient to correct ionospheric phase in the testing InSAR observation. Reason can be the bias of the altitudes of GPS satellites and SAR satellites.

Both MAI based method and AT based method worked well on ALOS PALSAR data. After ionospheric correction, phases appeared to have a linear relationship with respect to DEM, which indicated the rest phase anomalies were caused by troposphere. This two methods were also tested on ALOS-2 ScanSAR pre-seismic data. MAI based method has a bad performance on ALOS-2 ScanSAR data when the MAI phase was generated, the result lost coherence. Reason for it is because of the method itself and ScanSAR SLC data acquisition model and the further processing for Doppler spectrum. AT based method didn't have the issue of losing coherence, but the result was still not perfect due to the limitation of this method of solving quadratic ionospheric phase. Both methods can only be applied when there was no strong surface deformation.

Every method has its own advantages and disadvantages. Due to the complexity of

ionospheric phase in InSAR observations and the variety of SAR data, method should be choose according to applications and data itself.

For slope shaped ionospheric phase along a huge area, a residual phase removal strategy can be applied. For small scaled ionospheric phase that shows a relative more complicated structure, azimuth based method can be used. AT method can be choose when the coherence of image pair is low.

## 8.2 Outlook

Since residual phase removal strategy has been tested for only 2 pairs, more image pairs can be used to apply this method. After ionospheric correction, a better way to evaluate it to see if it works is to find a GPS GCP point in local site that measures the movements and compare the result of GPS and the movement results from ionospheric error free InSAR time series results.

Although CODE based method is not sufficient according to our experiments, but the products can be used as an observation of TEC concentration and can be used to evaluate whether our area is affected by TEC variance. This can be helpful for SAR data selection and judgment of the qualities of SAR observations.

For ionospheric phase correction, another method called “Split-Spectrum Method” has been developed and has a good performance on ALOS-2 ScanSAR data (Gomba, Parizzi, De Zan, Eineder, & Bamler, 2016), I can also implemented this method on our ALOS-2 ScanSAR data and compare it with the result we got from residual phase removal method.

So far, most of the methods that exists for ionospheric phase correction in InSAR observations are all focus on the first order ionospheric phase error. Studies about correction for the second order ionospheric error is still empty in this field. And now a days, not only in L-band SAR observations, ionospheric phase error were seen more often in C-band InSAR observations. Ionospheric phase correction becomes more and more important in InSAR applications.

# Bibliography

- Simons, M., Fialko, Y., & Rivera, L. (2002). Coseismic Deformation from the 1999  $M_w$  7.1 Hector Mine, California, Earthquake as Inferred from InSAR and GPS observations. *Bulletin of the Seismological Society of America*, 92(4):1390-1402.
- Ryder, I., Parsons, B., Wright, T. J., & Funning, G. J. (2007). Post-seismic motion following the 1997 Manyi (Tibet) earthquake: InSAR observations and modelling. *Geophysical Journal International*, 169(3), 1009-1027.
- Ferretti, A., Prati, C., & Rocca, F. (2001). Permanent scatterers in SAR interferometry. *IEEE Transactions on geoscience and remote sensing*, 39(1), 8-20.
- Lanari, R., Mora, O., Manunta, M., Mallorqui, J. J., Berardino, P., & Sansosti, B. (2004). A Small-Baseline Approach for Investigating Deformations on Full-Resolution Differential SAR Interferograms. *IEEE Transactions on geoscience and remote sensing*, 42(7):1377 - 1385.
- Haghshenas Haghighi, M., Motagh, M. (2016). Assessment of ground surface displacement in Taihape landslide, New Zealand, with C- and X- band SAR interferometry. *New Zealand Journal of Geology and Geophysics*, 59(1):136-146.
- Motagh, M., Shamshiri, R., Haghshenas Haghighi, M., Wetzel, H. U., Akbari, B., Hahavandchi, H., Roessner, S., & Arabi, S. (2017). Quantifying groundwater exploitation induced subsidence in Rafsanjan plain, southeastern Iran, using InSAR time-series and in situ measurements. *Engineering Geology*, 218:134-151.
- Wilson, B. D., Mannucci, A. J., & Edwards, C. D. (1995). Subdaily northern hemisphere ionospheric maps using an extensive network of GPS receivers. *Radio Science*, 30(3), 639-648.
- Gray, A. L., Mattar, K. E., & Sofko, G. (2000). Influence of ionospheric electron density fluctuations on satellite radar interferometry. *Geophysical Research Letters*, 27(10), 1451-1454.

- Mattar, K. E., & Gray, A. L. (2002). Reducing ionospheric electron density errors in satellite radar interferometry applications. *Canadian Journal of Remote Sensing*, 28(4), 593-600.
- Center for Orbit Determination in Europe (CODE)  
[http://www.aiub.unibe.ch/research/code\\_\\_\\_analysis\\_center/index\\_eng.html](http://www.aiub.unibe.ch/research/code___analysis_center/index_eng.html)
- Lanyi, G. E., & Roth, T. (1988). A comparison of mapped and measured total ionospheric electron content using global positioning system and beacon satellite observations. *Radio Science*, 23(4), 483-492.
- Mannucci, A. J., Wilson, B. D., Yuan, D. N., Ho, C. H., Lindqwister, U. J., & Runge, T. F. (1998). A global mapping technique for GPS - derived ionospheric total electron content measurements. *Radio science*, 33(3), 565-582.
- Wilson, B. D., Mannucci, A. J., & Edwards, C. D. (1995). Subdaily northern hemisphere ionospheric maps using an extensive network of GPS receivers. *Radio Science*, 30(3), 639-648.
- Dyrud L, Jovancevic A, Brown A, Wilson D, Ganguly S. Ionospheric measurement with GPS: Receiver techniques and methods. *Radio Science*. 2008 Dec;43(06):1-1.
- Jakowski, N., Hoque, M. M., & Mayer, C. (2011). A new global TEC model for estimating transionospheric radio wave propagation errors. *Journal of Geodesy*, 85(12), 965-974.
- Mateus, P., Catalão, J., & Nico, G. (2017). Sentinel-1 interferometric SAR mapping of precipitable water vapor over a country-spanning area. *IEEE Transactions on Geoscience and Remote Sensing*, 55(5), 2993-2999.
- Meyer, F. J., Bamler, R., Jakowski, N., & Fritz, T. (2006). The potential of low-frequency SAR systems for mapping ionospheric TEC distributions. *IEEE Geoscience and Remote Sensing Letters*, 3(4), 560-564.
- Meyer, F. J., & Nicoll, J. B. (2008). Prediction, detection, and correction of Faraday rotation in full-polarimetric L-band SAR data. *IEEE Transactions on Geoscience and Remote Sensing*, 46(10), 3076-3086.

- Meyer, F. J. (2011). Performance requirements for ionospheric correction of low-frequency SAR data. *IEEE transactions on geoscience and remote sensing*, 49(10), 3694-3702.
- Meyer, F. J. (2010, July). A review of ionospheric effects in low-frequency SAR—Signals, correction methods, and performance requirements. In 2010 *IEEE International Geoscience and Remote Sensing Symposium*, (pp. 29-32). IEEE
- Chen, J., & Zebker, H. A. (2012). Ionospheric artifacts in simultaneous L-band InSAR and GPS observations. *IEEE Transactions on Geoscience and Remote Sensing*, 50(4), 1227-1239.
- Wegmuller, U., Werner, C., Strozzi, T., & Wiesmann, A. (2006, July). Ionospheric electron concentration effects on SAR and INSAR. In 2006 *IEEE International Symposium on Geoscience and Remote Sensing* (pp. 3731-3734). IEEE.
- Chen, A. C., & Zebker, H. A. (2014). Reducing ionospheric effects in InSAR data using accurate coregistration. *IEEE transactions on geoscience and remote sensing*, 52(1), 60-70.
- Gomba, G., González, F. R., & De Zan, F. (2017). Ionospheric phase screen compensation for the Sentinel-1 TOPS and ALOS-2 ScanSAR modes. *IEEE Transactions on Geoscience and Remote Sensing*, 55(1), 223-235.
- Bechor, N. B., & Zebker, H. A. (2006). Measuring two - dimensional movements using a single InSAR pair. *Geophysical research letters*, 33(16).
- Jung, H. S., Won, J. S., & Kim, S. W. (2009). An improvement of the performance of multiple-aperture SAR interferometry (MAI). *IEEE Transactions on Geoscience and Remote Sensing*, 47(8), 2859-2869.
- Hu, J., Li, Z., Zhang, L., Ding, X., Zhu, J., Sun, Q., & Ding, W. (2012). Correcting ionospheric effects and monitoring two-dimensional displacement fields with

- multiple-aperture InSAR technology with application to the Yushu earthquake. *Science China Earth Sciences*, 55(12), 1961-1971.
- Hu, J., Li, Z. W., Ding, X. L., Zhu, J. J., Zhang, L., & Sun, Q. (2012). 3D coseismic displacement of 2010 Darfield, New Zealand earthquake estimated from multi-aperture InSAR and D-InSAR measurements. *Journal of Geodesy*, 86(11), 1029-1041.
- Jung, H. S., Lee, D. T., Lu, Z., & Won, J. S. (2013). Ionospheric correction of SAR interferograms by multiple-aperture interferometry. *IEEE Transactions on Geoscience and Remote Sensing*, 51(5), 3191-3199.
- Liu, Z., Jung, H. S., & Lu, Z. (2014). Joint correction of ionosphere noise and orbital error in L-band SAR interferometry of interseismic deformation in southern California. *IEEE Transactions on Geoscience and Remote Sensing*, 52(6), 3421-3427.
- Chae, S. H., Lee, W. J., Jung, H. S., & Zhang, L. (2017). Ionospheric correction of L-Band SAR offset measurements for the precise observation of glacier velocity variations on Novaya Zemlya. *IEEE Journal of Selected Topics in Applied Earth Observations and Remote Sensing*, 10(8), 3591-3603.
- Cao, N., Lee, H., Jung, H., & Yu, H. (2018). Estimation of water level changes of large-scale Amazon wetlands using ALOS2 ScanSAR differential interferometry. *Remote Sensing*, 10(6), 966.
- European Space Agency (ESA), *Geometry Glossary*. (2014). Retrieved from <https://earth.esa.int/handbooks/asar/CNTR5-5.html#eph.asar.gloss.geo:GEOMETRY>
- Sanz Subirana, J., Juan Zornoza, J. M., & Hernández-Pajares, M., (2011). Ionospheric Delay. Retrieved from [https://gssc.esa.int/navipedia/index.php/Ionospheric\\_Delay](https://gssc.esa.int/navipedia/index.php/Ionospheric_Delay)
- Hernandez - Pajares, M., Juan, J. M., Sanz, J., & Orús, R. (2007). Second - order ionospheric term in GPS: Implementation and impact on geodetic estimates. *Journal of geophysical research: solid earth*, 112(B8).

- Sanz Subirana, J., Juan Zornoza, J. M., & Hernández-Pajares, M. (2011). Ionosphere-free Combination for Dual Frequency Receivers. Retrieved from [https://gssc.esa.int/navipedia/index.php/Ionosphere-free\\_Combination\\_for\\_Dual\\_Frequency\\_Receivers](https://gssc.esa.int/navipedia/index.php/Ionosphere-free_Combination_for_Dual_Frequency_Receivers)
- Müller, J. (2016). *Spherical Harmonic Expansion of the Gravity Potential* [Class handout]. Hanover, Leibniz University Hanover.
- Heipke, C. (2016). *Central perspective and image orientation - a short review* [Class handout]. Hanover, Leibniz University Hanover.
- Motagh, M. (2017) SAR *Interferometry: Theory* [Class handout]. Hanover, Leibniz University Hannover
- MATLAB and Signal Processing Toolbox Release R2018a, The MathWorks, Inc., Natick, Massachusetts, United States. <http://www.mathworks.com/>
- Python Software Foundation, <https://www.python.org/>
- Aerospace Exploration Agency (JAXA), n.d., *About ALOS-PALSAR*. Retrieved from <https://www.eorc.jaxa.jp/ALOS/en/about/palsar.htm>
- Aerospace Exploration Agency (JAXA), n.d., *ALOS-2 Project/PALSAR-2*. Retrieved from <https://www.eorc.jaxa.jp/ALOS-2/en/about/palsar2.htm>
- Gomba, G., Parizzi, A., De Zan, F., Eineder, M., & Bamler, R. (2016). Toward operational compensation of ionospheric effects in SAR interferograms: The split-spectrum method. *IEEE Transactions on Geoscience and Remote Sensing*, 54(3), 1446-1461.
- SRTM DEM Digital Elevation Database, Consortium for Spatial Information (CGIAR-CSI), <http://srtm.csi.cgiar.org/>
- Goldstein, R. M., & Werner, C. L. (1998). Radar interferogram filtering for geophysical applications. *Geophysical research letters*, 25(21), 4035-4038.
- Costantini, M. (1998). A novel phase unwrapping method based on network programming. *IEEE Transactions on geoscience and remote sensing*, 36(3), 813-821.



Mark A. Wieczorek and Matthias Meschede (2018). SHTools — Tools for working with spherical harmonics, *Geochemistry, Geophysics, Geosystems*, 19, 2574-2592, doi:10.1029/2018GC007529.

Zebker, H. A., Rosen, P. A., & Hensley, S. (1997). Atmospheric effects in interferometric synthetic aperture radar surface deformation and topographic maps. *Journal of geophysical research: solid earth*, 102(B4), 7547-7563.

Gomba, G., Parizzi, A., De Zan, F., Eineder, M., & Bamler, R. (2016). Toward operational compensation of ionospheric effects in SAR interferograms: The split-spectrum method. *IEEE Transactions on Geoscience and Remote Sensing*, 54(3), 1446-1461.